2008

A Genetic Bayesian Approach for Texture-Aided Urban Land-Use/Land-Cover Classification

Wenxue Ju
Louisiana State University and Agricultural and Mechanical College, wju1@lsu.edu

A GENETIC BAYESIAN APPROACH FOR TEXTURE-AIDED URBAN LAND-USE/LAND-COVER CLASSIFICATION

A Dissertation

Submitted to the Graduate Faculty of the
Louisiana State University and
Agricultural and Mechanical College
in partial fulfillment of the
requirements for the degree of
Doctor of Philosophy

in

The Department of Geography and Anthropology

by
Wenxue Ju
B.S., Peking University, 2000
M.S., Peking University, 2003
December 2008

Acknowledgments

I am deeply grateful to Dr. Nina Lam, my major professor, for her advice, guidance, and support throughout my study and research. I sincerely thank Professors Michael Leitner, Robert Rohli, Jianhua Chen, and Max Conrad for their valuable comments and advice as members of my dissertation committee. I thank Dr. Barrett Kennedy, Dr. John Pine, and Mr. Farrell Jones for their support during my study. I am indebted to my fellow students at LSU for their help on my study and their friendship; I especially thank Wei Liang, Andrew Augustine, and Terrence McCloskey for their valuable comments on my dissertation.

I am very grateful to the loving members of my family. I thank my father Sixiang Ju and my mother Yunying Zang for their everlasting love and motivation. I thank my brother Wencheng Ju for his long-time encouragement. Finally, I thank my wife Honghua Wang, my daughters Jerica Jiaqi Ju and Jennifer Jiayu Ju for their understanding, support, and encouragements on my research.

This research was partially supported by the Doctoral Dissertation Research Improvement (DDRI) Grant from the National Science Foundation (BCS-0726512). IKONOS satellite imagery is courtesy of Geoeye. Aerial photographs are courtesy of the LSU GIS - Hurricane Katrina and Rita Clearinghouse Cooperative and the LSU CADGIS Research Laboratory.

Table of Contents

List of Tables

List of Figures

Abstract

Urban land-use/land-cover classification is entering a new era with the increased availability of high-resolution satellite imagery and new methods such as texture analysis and artificial intelligence classifiers. Recent research demonstrated exciting improvements of using fractal dimension, lacunarity, and Moran's *I* in classification but the integration of these spatial metrics has seldom been investigated. Also, previous research focuses more on developing new classifiers than improving the robust, simple, and fast maximum likelihood classifier. The goal of this dissertation research is to develop a new approach that utilizes a texture vector (fractal dimension, lacunarity, and Moran's *I*), combined with a new genetic Bayesian classifier, to improve urban land-use/land-cover classification accuracy. Examples of different land-use/land-covers using post-Katrina IKONOS imagery of New Orleans were demonstrated.

Because previous geometric-step and arithmetic-step implementations of the triangular prism algorithm can result in significant unutilized pixels when measuring local fractal dimension, the divisor-step method was developed and found to yield more accurate estimation. In addition, a new lacunarity estimator based on the triangular prism method and the gliding-box algorithm was developed and found better than existing gray-scale estimators for classifying land-use/land-cover from IKONOS imagery.

The accuracy of fractal dimension-aided classification was less sensitive to window size than lacunarity and Moran's *I*. In general, the optimal window size for the texture vector-aided approach is 27x27 to 37x37 pixels (i.e., 108x108 to 148x148 meters). As expected, a texture vector-aided approach yielded 2-16% better accuracy than individual textural index-aided approach. Compared to the per-pixel maximum likelihood classification, the proposed genetic Bayesian classifier yielded 12% accuracy improvement by optimizing prior probabilities with the

genetic algorithm; whereas the integrated approach with a texture vector and the genetic Bayesian classifier significantly improved classification accuracy by 17-21%. Compared to the neural network classifier and genetic algorithm-support vector machines, the genetic Bayesian classifier was slightly less accurate but more computationally efficient and required less human supervision. This research not only develops a new approach of integrating texture analysis with artificial intelligence for classification, but also reveals a promising avenue of using advanced texture analysis and classification methods to associate socioeconomic statuses with remote sensing image textures.

Chapter 1
Introduction

1.1 Urban Land-Use/Land-Cover Classification

Accurate land-use/land-cover (LULC) classification from satellite imagery is critical to many environmental applications. With the consistent operation of commercial satellites such as Landsat-5, LULC can be periodically monitored and their changes can be easily detected at low cost. Recent invention of high spatial resolution sensors such as IKONOS, QuickBird, and WorldView-1 make ground features more clearly identifiable than ever, thus promoting LULC classification to a new era. In existing literature, high-resolution imagery was used in USGS Level II classification to separate different urban lands, such as residential, commercial, and industrial (Myint et al., 2006) or even further separate high canopy covered residential neighborhoods from those with low canopy coverage (Myint and Lam, 2005a).

Traditionally, different LULC classes were classified purely based on the captured spectral information (electromagnetic reflectance) of ground features, assuming that same land cover has a similar signature statistically. In supervised classification scenarios, the original image is often classified pixel-wise by using the spectral signature of different LULC classes. This method is referred as the per-pixel method. This method has been used successfully in USGS Level I (Anderson et al. 1976) classification scenarios for a long time, using Landsat-5 TM imagery, with some accuracy problems identified in complex urban areas. It is well known that the low accuracy in urban area is caused by relatively large in-class spectral variance and between-class overlaps. The problem is even worse for high-resolution imagery such as IKONOS and QuickBird imagery. Compared to the 30-meter resolution multispectral bands and 15-meter panchromatic band of Landsat-5 TM imagery, IKONOS provides 4-meter resolution multispectral bands and 1-meter panchromatic band, while QuickBird provides 2.4-meter

resolution multispectral bands and sub-meter (0.6m) resolution for its panchromatic band. The meter-level-resolution imagery exhibits a clear view of urban area with detailed components, such as single-family houses, multi-family houses, parking lots, driveways, amenity grasses, and cars. These components exhibit sharp spectral differences but could co-exist in one land use class (residential area); the same component could exist in multiple land use categories. For example, the same construction materials could be used in residential area and commercial area.

Regarding this complex problem, two alternative solutions have been developed in previous literature (e.g. Huang et al., 2002; Myint and Lam, 2005a). First, texture analysis methods were used to provide textural information in addition to spectral information. Myint and Lam (2005a) argued that, "This spatial information needs to be extracted, in addition to its individual spectral value, to characterize the heterogeneous nature of urban features in high-resolution images". Second, alternative classifiers that utilize artificial intelligence and machine learning algorithms have been used to improve classification accuracy.

However, previous research tends to investigate the performance of individual textural index, such as fractal dimension, lacunarity, and Moran's *I* (Emerson et al., 2005; Myint and Lam, 2005a), rather than to integrate these powerful metrics together to form a texture vector to assist classification. Also, previous research focuses more on alternative classifiers (Erbek et al., 2004; Huang et al., 2002) than improving the robust, simple, and fast maximum likelihood classifier; it could be promising to improve the maximum likelihood classifier by optimizing the prior probabilities with a fast and efficient genetic algorithm and then combine with a texture vector for fast and accurate land use/cover classification.

1.2 Texture Analysis

The heterogeneous nature of urban environment caused by multiple materials and land cover integration has prompted researchers to use a texture-aided classification approach instead of pure per-pixel spectral-based image classification (Myint and Lam, 2005a). Generally there are three directions of using textural information: contextual classification, textural-layer method, and object-based approach. The neighborhood relationship is modeled in contextual classification with Markov or Gibbs random fields (Jackson and Landgrebe, 2002; Kasetkasem and Varshney, 2002; Solberg et al., 1996). In the textural-layer method, textural layers are extracted with a moving window technique (assigning local measurements to centers of moving windows) on original (Dong, 2000; Emerson et al., 2005) or transformed images (Carr and de Miranda, 1998) and then they are stacked, with or without spectral layers for classification. The object-based approach segments the images into objects based on both their spectral and textural information (Hu et al., 2005; Mitri and Gitas, 2004; Pal and Pal, 1993; Woodcock and Harward, 1992).

Unlike the per-pixel based classification which solely relies on the spectral information (visualized as color for a three bands composite), texture-aided methods utilize the neighborhood information around pixels to quantitatively interpret the image texture. Quantitative measurement of image texture is essential to various texture-aided approaches. Recent research demonstrated successful examples of using the following texture metrics in image characterization and classification: fractal dimension (Emerson et al., 1999; Lam et al., 2002; Zhao, 2001), lacunarity (Dong, 2000; Myint and Lam, 2005a), Moran's *I* spatial autocorrelation (Emerson et al., 2005), Getis statistic (Wulder and Boots, 1998), semivariogram (Carr and de Miranda, 1998; Miranda et al., 1998), co-occurrence matrix (Jobanputra and Clausi, 2006),

compactness and smoothness (Hu et al., 2005; Mitri and Gitas, 2004; Yu et al., 2006), and geostatistical metrics like entropy, variance, fragment index, and diversity (Carr and de Miranda, 1998; Li et al., 2004; Zhu and Yang, 1998). Improvements in texture-aided classification are impressive. Emerson et al. (2005) reported a 10% (67% to 77%) improvement in Landsat ETM+ imagery classification when a fractal layer was added to multispectral layers for classification. Dong and Leblon (2004) found that the lacunarity measure was useful to improve rock unit discrimination by 8%. Myint and Lam (2005a) reported that adding a spatial autocorrelation or lacunarity layer could improve land cover classification from 55% to 78% or 92%, respectively. With object-based classification using texture measures such as compactness and smoothness, Mitri and Gitas (2004) reported a high accuracy for burned area mapping with Landsat TM imagery: 94.59% user's and 97.22% producer's accuracy.

Spatial resolution plays an important role in texture analysis. Most LULC categories are more uniform in LandSat-5 TM imagery than in IKONOS imagery. Given the finer resolution of latter imagery, textural analysis is even more critical, as heterogeneous spectral information often violates the normality assumption of the maximum likelihood classifier (Myint and Lam 2005a). Textural metrics are scale dependent and their performance varies with scale and image type. For example, fractal was found to be more successful on LandSat-5 TM (Emerson et al., 2005; Lam, 2004) than IKONOS (Myint and Lam, 2005a). The need of using local window to derive neighborhood texture measurements makes the texture interpretation highly dependent on window size. Computational efficiency and classification accuracy vary across different moving window sizes that are utilized to generate textural layers (Emerson et al., 2005; Myint and Lam, 2005a). Although with some performance variation, the texture-aided approach has been reported to improve classification in many studies (Carr and de Miranda, 1998; Mitri and Gitas, 2004).

Comparisons among different metrics were made by a number of studies. Emerson et al. (2005) found fractal dimension more effective than local variance and Moran's *I* for classifying land-use/land-cover with Landsat TM imagery. Myint and Lam (2005a) reported that lacunarity was more effective than fractal dimension in classification scenarios with IKONOS imagery.

1.3 Artificial Intelligence Classifiers

A well-known problem of the maximum likelihood classifier is that its Gaussian distribution assumption of the image data is often violated in complex urban land-use/land-cover classification. Alternative classifiers have been applied to improve classification accuracies such as artificial neural networks (Bagan et al., 2005; Erbek et al., 2004; Kavzoglu and Mather, 2003; Mills et al., 2006; Verbeke et al., 2004), decision tree (Gislason et al., 2006; McIver and Friedl, 2002; Pal and Mather, 2003), and support vector machines (Foody and Marthur, 2004b; Huang et al., 2002; Pal and Mather, 2005).

While these approaches improve the classification accuracy, some bring other issues such as the training efficiency and additional requirements of user supervision. For example, the artificial neural network approach generally has a time-consuming training process. The configuration of parameters in support vector machines requires a trial-and-error approach (Huang et al., 2002). The goals of satellite image classification should include not only accuracy, but also the possibility for automation to reduce human supervision, and computational efficiency. The maximum likelihood classifier has a robust generalized mathematical formula and is easy to apply. Although it has problems, the maximum likelihood classifier is still widely used because it is the most commercially available classifier in remote sensing and photogrammetric software and is easy to apply. Huang et al. (2002) stated that, "Despite limitations due to its assumption of normal distribution of class signature, it is perhaps one of the most widely used classifiers".

1.4 Problem Statement and Research Objectives

Due to the low accuracy of applying the traditional spectral-based land use classification methods in the heterogeneous urban environment, especially when using high-resolution satellite imagery (Chen et al., 2004; Myint and Lam, 2005a), various texture indices were introduced recently to characterize the image pattern, such as fractal dimension (De Cola, 1989; Emerson et al., 1999; Lam, 2004; Lam et al., 2002; Qiu et al., 1999; Quattrochi and Goodchild, 1997; Sun et al., 2006), lacunarity (Dong, 2000; Greenhill et al., 2003; Myint et al., 2006), and spatial autocorrelation (Cliff and Ord, 1973; Emerson et al., 2005; Lam et al., 2002). Although the combination of texture and spectral information have been applied in some land-use/land-cover classification scenarios (Emerson et al., 2005; Myint and Lam, 2005a) and the performance comparison between different indices has been demonstrated in some literature (Emerson et al., 2005; Myint and Lam, 2005a), the utilization of these textural indices (fractal dimension, lacunarity, and Moran's *I*) together as a texture vector to aid texture-spectral based classification has seldom been done. It is expected that a texture vector has the capability to describe multiple aspects of the texture pattern of heterogeneous urban area, and hence better classification results can be yielded.

Fractal dimension, lacunarity, and Moran's *I* are different from many other statistical textural indices (e.g. mean and standard deviation) in that their measurements are sensitive to the spatial arrangements of pixels and they can be directly applied to the original spectral bands and to the study area as a whole or locally. When applied locally, some problems emerge. The problem of applying Moran's *I* locally has been reported by Lam et al. (2008). For fractal dimension algorithms, their local implementation could result in some pixels excluded from calculation. However, this problem has seldom been investigated. For lacunarity analysis of

remote sensing image, the performance of the existing two gray-scale estimators (Dong, 2000; Voss, 1986) has yet to be compared and tested.

Another concern when dealing with texture analysis is the size of "moving window" (Emerson et al., 2005; Lam et al., 2002), which is used to measure the local texture pattern. Different window sizes for different texture indices have been compared in some literature (Chen et al., 2004; Emerson et al., 2005; Myint and Lam, 2005a), which clearly shows the existence of an "optimal window". The term "optimal window", as used in this dissertation research, means a turning point of texture pattern and is often referred to the point of maximum complexity. In terms of texture-aided classification, the accuracy will increase to a certain level with increasing window size but will decrease thereafter. As argued in some previous studies (Chen et al., 2004; Hodgson, 1998; Zhou, 2006), the size of "optimal window" is closely associated with the landscape pattern of the image being analyzed (Chen et al., 2004). Thus, there is a need to study the quantitative relationships between optimal window, texture measures, and LULC objects.

Instead of improving the widely-used maximum likelihood classifier, different classifiers have been developed for land cover classification, such as artificial neural networks (Bagan et al., 2005; Erbek et al., 2004; Kavzoglu and Mather, 2003; Mills et al., 2006; Verbeke et al., 2004), decision tree methods (DeFries et al., 1998; Galante, 1996; Gislason et al., 2006; McIver and Friedl, 2002; Pal and Mather, 2003), support vector machines (Foody and Mathur, 2004a; Pal, 2006), and discriminant analysis (Myint et al., 2004). One important part of using maximum likelihood classifier is the prior probability, which is often assumed to be the same for all classes or assigned using the proportion of training samples in each class. The prior probabilities are rarely optimized with other methods, except in some contextual classification using Markov/Gibbs random field (Jackson and Landgrebe, 2002; Kasetkasem and Varshney, 2002;

Solberg et al., 1996). Since they are between 0 and 1, some search methods could be applied to find the optimal solution to achieve higher classification accuracy. Because genetic algorithms are quite efficient and fast in optimizing weights (Galante, 1996; Huang et al., 2004; Maniezzo, 1994) or location search (Li and Yeh, 2005), it is promising to use genetic algorithms to optimize the prior parameter in maximum likelihood classification to boost its performance.

The goal of this dissertation research is to develop more efficient and accurate methods for classifying urban LULC from high-resolution imagery. The ultimate goal is to reduce human supervision and enable automation for a variety of environmental applications. The overriding hypothesis for this dissertation is: integrating the texture vector-aided approach with artificial intelligence classifiers can improve urban LULC classification accuracy. The research will investigate the performance of utilizing a texture vector (fractal dimension, lacunarity, and Moran's *I*), combined with an innovative genetic Bayesian classifier, to improve the urban land-use/land-cover classification accuracy using high-resolution IKONOS imagery post-Katrina in New Orleans, Louisiana. Specifically, the objectives are:

(1) To develop more efficient algorithms of calculating local fractal dimension;

(2) To evaluate and determinate the best lacunarity estimators;

(3) To determine the effects of windows size and the optimal window size for deriving local neighborhood textural measurements with fractal dimension, lacunarity, and Moran's *I*, using the IKONOS imagery;

(4) To develop a genetic Bayesian classifier to boost the classification performance of the traditional maximum likelihood method by optimizing the prior probabilities, and to test the robustness and computational efficiency of the classifier;

(5) To determine whether combining a texture vector-aided approach (fractal dimension,

lacunarity, and Moran's *I*) and the proposed genetic Bayesian classifier is efficient in classifying heterogeneous urban area and identifying different residential neighborhoods with different social-economic statuses.

1.5 Expected Significance of the Research

For the intellectual merits, this dissertation research will contribute to four aspects. First, more efficient algorithms will be developed for calculating local fractal dimension and lacunarity. The research results will provide better options for application scenarios in geographic information science and benefit future improvements to the estimation of fractal dimension and lacunarity. Second, by using a genetic algorithm, the proposed genetic Bayesian classifier will optimize the prior probability parameter of the maximum likelihood classifier to boost its performance without losing the computational efficiency or adding substantial human supervision. Third, this study is among the few to bring the most recent successful texture indices like fractal dimension, lacunarity, and Moran's *I* together to build a texture vector to assist urban LULC classification. Although many approaches with these indices have been experimented, very few studies bring them together to demonstrate different aspects of the texture pattern of the remotely sensed image, which could lead to accurate classification. The use of the combined genetic Bayesian classifier and texture vector-aided approach could make automation and generalization to other study areas easier. Fourth, previous research about texture analysis with different window sizes implies the existence of the "optimal window". The proposed study will identify the quantitative relationships between the effects of window size on fractal dimension, lacunarity, and Moran's *I* when using IKONOS imagery, and discuss the relationship between the size of "optimal window" and the land use objects. The findings will increase our understanding of the nature of the moving window technique and serves as guidance

for the selection of appropriate window size when performing texture analysis with high-resolution imagery.

This dissertation research will have four broad impacts. First, the improved algorithms of fractal dimension and lacunarity can be applied to many other applications that use these indices. Second, although the proposed genetic Bayesian classifier is primarily used for one urban LULC classification scenario, the methodology can be applied to other classification scenarios in other scientific disciplines. The MATLAB modules developed in this research can be widely distributed (through http://www.lsu.edu/rsgis) to benefit other research. Third, the proposed integration of multiple texture indices may be further applied to some other classification methods, such as the rapidly-growing object-based classification that emphasizes the use of texture. Fourth, the improved classification of New Orleans will be helpful to urban structure analysis. The results will also be useful to government agencies for urban planning, environmental assessment, disaster or special event monitoring such as hurricane, earthquake, and vegetation health, as well as guiding the recovery.

1.6 Chapter Organization

The entire dissertation is organized into six journal-style chapters. Each chapter can be treated as a separate paper but are linked together under the central topic of the dissertation. The second, third, and fourth chapters focus on basic problems of textural approach, and the fifth and sixth chapters focus on the genetic Bayesian classifier, its integration with textural approach and comparison with other classification methods.

First, based on the literature review, research problems are defined in this introduction chapter. A new method of calculating fractal dimension is presented in the second chapter, followed by a chapter discussing a new lacunarity estimator and the inconsistency problem

among different gray-scale lacunarity algorithms. The fourth chapter investigates the optimal window size issue of the three spatial-based textural indices: fractal dimension, lacunarity, and Moran's *I*, when applied to urban LULC classification scenarios with an IKONOS image. In the fifth chapter, a new classifier, genetic Bayesian classifier, is presented. Fractal dimension is used along with lacunarity and Moran's *I* for texture vector extraction. They are then combined with the GBC method for land-use/land-cover classification. In the sixth chapter, integration of texture analysis with artificial intelligence classifiers is further investigated and compared with other classifiers including the maximum likelihood classifier, genetic Bayesian classifier, multi-layer perceptron neural network classifier, and genetic algorithm – support vector machines. A special scenario of discriminating four residential neighborhoods with different economic statuses and impacts by Hurricane Katrina is discussed. The seventh chapter summarizes the findings and significance of this dissertation research.

Chapter 2
An Improved Algorithm for Computing Local Fractal Dimension Using the Triangular Prism Method

2.1 Introduction

As a promising spatial metric, the fractal dimension (Mandelbrot, 1983) has been frequently applied in many geoscience applications, including remote sensing image complexity characterization (De Cola, 1989; Lam, 2004; Liu and Cameron, 2001; Qiu et al., 1999; Quattrochi et al., 2001; Turner and Ruscher, 1988), land-use/land-cover classification, and change detection (Chust et al., 2004; Emerson et al., 2005; Myint and Lam, 2005a; Myint et al., 2004; Read and Lam, 2002). Despite the many applications, the problem of inconsistent results derived from different fractal calculation algorithms remains. Algorithms such as the isarithm, variogram, probability, box-counting and triangular prism methods have been proposed and tested (Goodchild, 1980; Jaggi et al., 1993; Lam and De Cola, 1993; Sun et al., 2006; Tate, 1998; Voss, 1988). For complex surfaces such as remote sensing images, it was found that the modified triangular prism method was the most reliable estimator when compared with the isarithm and variogram methods (Lam et al., 2002; Zhou and Lam, 2005). This paper focuses on improving the triangular prism method, especially on extending its applications for local measurements.

Originally proposed by Clarke (1986), the triangular prism method utilizes imaginary three-dimensional prisms constructed from the image, and then compares the total prism surface area with the step size used to derive the prisms in a double-logarithmic regression. The slope of the regression is then used to estimate the fractal dimension. Specifically, a triangular prism is constructed by connecting four adjacent pixels and its center (Figure 2.1a). The height of each corner pixel is the pixel intensity value and the height of the center takes the average of the four corner pixels. The step size is the number of pixels on a side. Given a step size, triangular prisms

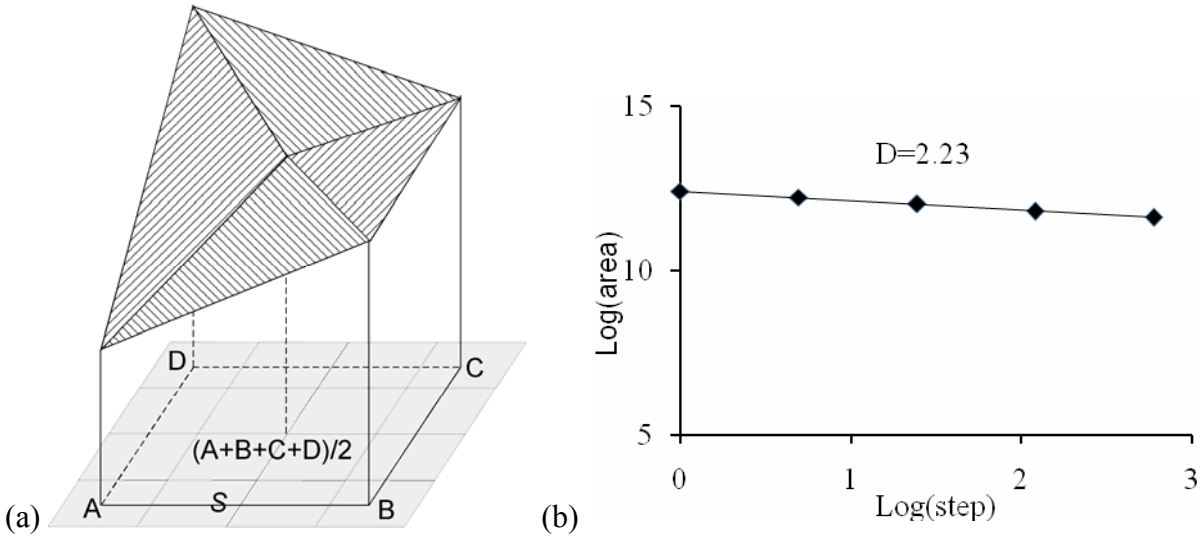

Figure 2.1 A triangular prism (a) and a regression plot (b).

are constructed across the image and the total surface area of all triangular prisms calculated. The procedure is repeated for each step size. A double-log regression (Figure 2.1b) between the total prism surface area (A) and the area of step size (S^2) is estimated to derive the slope B, where fractal dimension D=2-B. Clarke's original algorithm was later modified so that the length of step size, not step size squared, is used in the regression, because the use of step size squared led to underestimation of the fractal dimension (Jaggi et al., 1993). The modified triangular prism method was subsequently proven to be mathematically correct, as well as experimentally reliable (Lam et al., 2002; Zhao, 2001). It was then suggested that the modified triangular prism method should be used. Hence,

$$Log\ A = a + (2\text{-}D)\ Log\ S \qquad (1)$$

where A is the total surface area of the prism "facets", S is the step size, a is the intercept, and D is the fractal dimension. In the remainder of the paper, whenever the term "triangular prism method" is used, it implies the modified version. It is noted that some other variants were also developed by using alternative pixels other than corner pixels of the square (Sun, 2006).

In general, the triangular prism method is very robust in its estimation of the fractal dimension. The only source of estimation variation is the choice of the number of steps and the corresponding step sizes. How to determine these two related parameters so that the results are reliable is the focus of this study. In essence, this is an issue of sampling strategy, which is common to many fractal estimation algorithms and will affect the estimation accuracy. This paper introduces a new sampling strategy, called the divisor-step method, which is designed to overcome the weakness of the geometric-step method that has been commonly employed in the triangular prism method.

2.2 Sampling Issues

The original algorithm by Clarke (1986) uses a series of geometric steps with an increase in power of two until it reaches the maximum limit imposed by the algorithm. For example, for a 33x33 image, steps 1, 2, 4, 8, and 16 can be used. The maximum step size is usually bounded by a value equivalent to the image size minus one and divided by half ((W-1)/2), which is 16 in this case. Otherwise, it will result in only one triangular prism for the largest step (S=32 for the example), which could lead to unstable log-log area-step regression. The use of geometric steps is to ensure that points are distributed uniformly on the log-log regression curve so that an unbiased regression can be obtained. However, if the size of an image (or local window within an image) is not of 2^n+1 pixels (for convenience, it is called "geometric-square" image thereafter), a portion of the image will not be included in the calculation. This is considered undesirable from a theoretical point of view, as variation in some parts of the image is not measured. When apply the algorithm locally to a small non-geometric-square local window, the omitted portion could be significantly large that could lead to unreliable estimation of local fractal dimension. For example, if the local window size is 29x29, using geometric steps of 1, 2,

4, and 8, only 17x17 (i.e., 2^n+1) pixels will be used, whereas the remaining 2/3 pixels within the window will not be included in the estimation.

Another sampling method is to employ arithmetic steps, such as 1, 2, 3, 4, and so on. The arithmetic-step method has an advantage that it can yield sufficient number of area-step points for the log-log regression even for a very small study area. However, since it is not a geometric progression, a counter argument for this method is that these arithmetic points might bias the log-log regression estimate as a result of including more samples at the lower end of the regression. The proposed divisor-step method is designed such that full coverage of the sampling area is ensured at each step.

2.3 Comparison Using Effective Coverage Ratio

2.3.1 The Geometric-Step Method (Fixed Coverage)

The geometric-step method, as originally presented by Clarke (1986), requires the calculation to be based on a geometric-square subset of the study area. It has a fixed coverage for all the geometric steps. Figure 2.2a shows the geometric steps of 1, 2, and 4 for an 11 x 11 local window. For ease of visual comparison with other methods, the upper-left subset is used instead of center cut. It is apparent from Figure 2.2a that some pixels are “wasted” and will not be included in the calculation. As already mentioned above, this will cause two problems. First, the calculated fractal dimension is not a true measurement of the entire window, and second, local windows with different sizes may have the same measurements as they may be confined by the same sampling sizes for calculation.

2.3.2 The Geometric-Step Method (Varying Coverage)

To extend the ability of using geometric steps in the calculation of non-geometric-square windows, some algorithms will let the triangular prisms grow within the study area and cover as

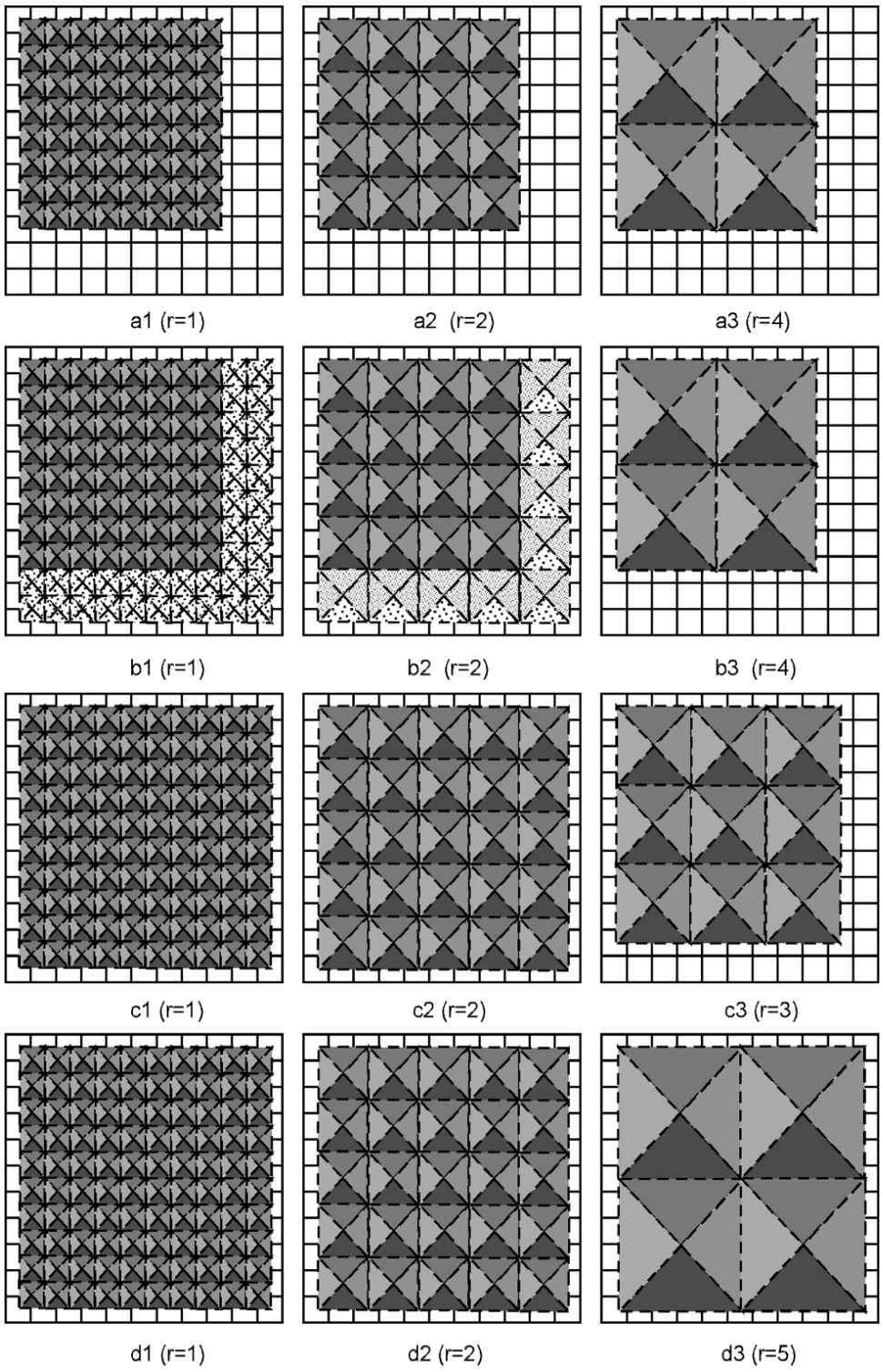

Figure 2.2 A top-view demonstration of the coverage (shaded prisms) by different sampling methods with an 11x11 window. a1-a3: the geometric-step method (fixed coverage); b1-b3: the geometric-step method (varying coverage); c1-c3: the arithmetic-step method; d1-d3: the divisor-step method.

many pixels as possible. The coverage of triangular prisms at each step may vary, as illustrated in Figure 2.2b. This method was implemented in the Image Characterization And Measurement System (ICAMS) software (Lam et al., 1998; Quattrochi et al., 1997). Although the coverage in this method is larger than that of the original algorithm, it is clear that complete coverage of the entire study area at all steps is not guaranteed.

2.3.3 The Arithmetic-Step Method

The arithmetic-step method has been used in previous research to obtain sufficient number of regression points when using a small window (e.g. Emerson et al., 2005). The number of pixels utilized in the arithmetic-step method is generally more than that of the geometric-step methods. Figure 2.2c presents the first three steps (1, 2, and 3) using the arithmetic-step method for the same 11x11 window. Similar to the geometric-step methods, however, 100% coverage of the entire window at all steps is not guaranteed.

2.3.4 The Proposed Divisor-Step Method

This new sampling method is developed in this research. To cover the entire W x W window (W is an odd number) by triangular prisms at any given step, the step size should be a divisor of (W-1). Using a set of divisor steps of (W-1) will guarantee 100% coverage of the entire window at all steps. For this example, the three divisible steps are 1, 2, and 5 (Figure 2.2d). By taking advantage of the 100% window coverage at all steps, the derived fractal dimension value is expected to measure more accurately the surface variation within the study area. This is especially critical to local fractal estimation, as excluding some pixels for calculation in a small window area is more likely to lead to unreliable results.

2.3.5 Effective Coverage Ratio and Coverage Fluctuation

To quantify the effects of different algorithms on pixel utilization, the ratio between the average number of utilized pixels at each step and the total number of pixels contained in the local window can be used. In this study, we define this ratio as effective coverage ratio (ECR):

$$ECR = \{\sum_{i\in\{s\}} \{floor[(W-1)/i]*i+1\}^2 / n\} / \{W \times W\} \quad (2)$$

where *{s}* is the collection of step length, W is the size of the local window, $\{floor[(W-1)/i]*i+1\}^2$ is the coverage (in pixels) at a given step i, n is the size of the collection *{s}*. The higher the ECR, the fewer the wasted pixels will be. For the geometric (fixed coverage) method, as the calculation is based on a square subset, the ECR is calculated as the following:

$$ECR = \{[floor(\log_2 W)+1]/W\}^2 \quad (3)$$

Along with ECR, the standard deviation of coverage (SDC) for all steps for each method can be calculated. Table 2.1 lists the ECR and SDC of different methods at different window sizes. The divisor-step method has 100% coverage, whereas the geometric-step method (fixed coverage) has the largest waste of pixels (i.e., lowest ECR), hence is not considered desirable and will not be tested further with simulated surfaces. The arithmetic-step method and the geometric-step (varying coverage) generally have larger ECRs than the geometric-step method (fixed coverage). Neither geometric-step (varying coverage) nor arithmetic-step method can guarantee a full coverage for all steps. The ECR and coverage fluctuation (SDC) are expected to affect the accuracy and robustness of subsequent fractal surface dimension estimation.

Table 2.1 Effective Coverage Ratios (ECR) and standard deviation of coverage (SDC) of different sampling methods (%)

Window	Geometric (fixed)		Geometric (varying)		Arithmetic		Divisor	
	ECR	SDC	ECR	SDC	ECR	SDC	ECR	SDC
9x9	100	0.00	100	0.00	90.12	1.23	100	0.00
13x13	47.93	0.00	100	0.00	95.27	0.48	100	0.00
17x17	100	0.00	100	0.00	89.19	0.49	100	0.00
21x21	65.53	0.00	91.38	0.17	86.21	0.47	100	0.00
25x25	46.24	0.00	100	0.00	88.41	0.34	100	0.00
29x29	34.36	0.00	93.58	0.13	85.13	0.30	100	0.00
33x33	100	0.00	100	0.00	83.79	0.28	100	0.00
37x37	79.55	0.00	91.82	0.11	87.63	0.23	100	0.00
41x41	64.78	0.00	92.96	0.16	84.87	0.22	100	0.00
45x45	53.78	0.00	87.36	0.20	82.15	0.20	100	0.00
49x49	45.36	0.00	100	0.00	84.76	0.18	100	0.00
53x53	38.77	0.00	94.19	0.08	82.87	0.16	100	0.00
57x57	33.52	0.00	94.78	0.12	83.84	0.16	100	0.00
61x61	29.27	0.00	90.37	0.15	84.92	0.14	100	0.00
65x65	100	0.00	100	0.00	82.72	0.14	100	0.00
69x69	88.74	0.00	94.37	0.06	81.49	0.13	100	0.00

2.4 Comparison Using Simulated Images

2.4.1 Shear Displacement Simulation

Because simulated self-similar fractal surfaces have frequently been used for benchmark testing, we will also utilize these simulated surfaces to test the performance of the different sampling methods (Lam et al., 2002; Zhou and Lam, 2005). The shear displacement method is one of the popular algorithms used to generate fractional Brownian motion (fBm) surfaces (Goodchild, 1980; Lam and De Cola, 1993; Mandelbrot, 1975; Mandelbrot, 1983). The algorithm works as follows: An image is initialized with zero values everywhere. The image is then randomly cut into halves and each part is randomly shifted vertically. This shear-and-displacement process is repeated for a number of times until there are several cliffs between adjacent pixels. A Poisson process controls the intersection points of the break lines while the angles of intersections are uniformly distributed. A persistence factor H controls the magnitude of vertical shift and H satisfies:

$$E(Z_i - Z_{i+d})^2 = |d|^{2H} \quad (4)$$

where Z_i is the pixel value and d is the pixel distance. The expected variance between two pixels is a function of their distance powered by $2H$. Fractal dimension is $3-H$.

The shear displacement algorithm has been implemented in ICAMS (Lam et al., 1998; Quattrochi et al., 1997) with a batch mode available. Figure 2.3 shows a set of 45x45 fractal surfaces with varying levels of complexity generated using ICAMS.

2.4.2 Comparison among Different Sampling Methods

To compare the accuracy and robustness of different sampling methods, a set of small simulated surfaces with 16 sizes ranging from 9x9 to 69x69 were generated. These window sizes were selected because this series covers most windows used in previous image classification or

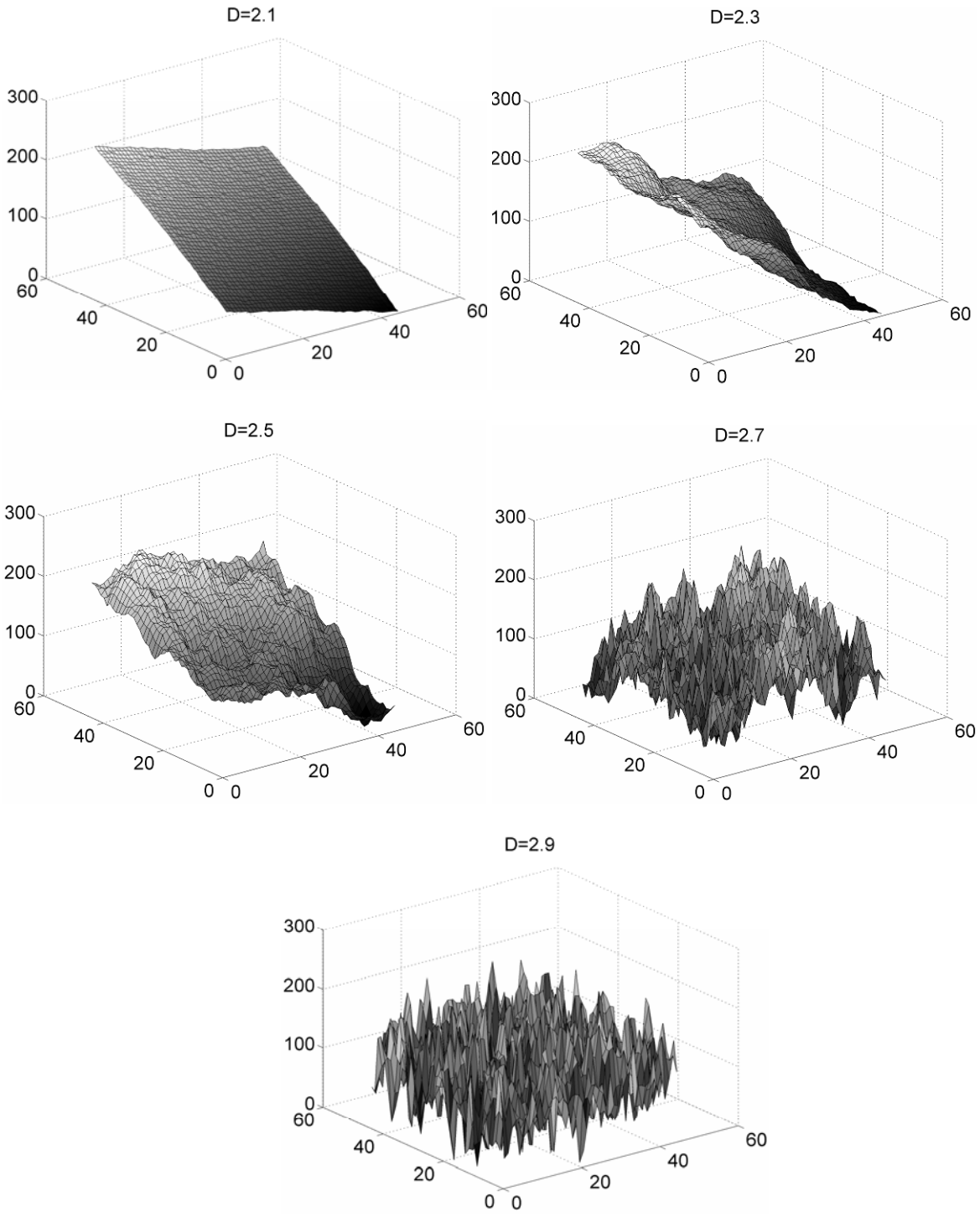

Figure 2.3 Fractional Brownian surfaces (45x45) generated using the shear displacement algorithm (3000 cuts).

segmentation research that uses local fractal measurements (Dejong and Burrough, 1995; Emerson et al., 2005; Myint and Lam, 2005a). For each window size, 50 surfaces were generated for each of the five theoretical dimensions (2.1, 2.3, 2.5, 2.7, and 2.9) using the same number of cuts (3000). The 50 surfaces were generated with the same control parameters (theoretical dimension, image size, number of cuts), but each time a different sequence of random numbers was used, hence the surfaces are different. The surfaces were generated by ICAMS based on the algorithm described in Lam and De Cola (1993). This resulted in a total of 4,000 surfaces used for this experiment. All simulated surfaces were stretched to 0-255 to provide the same basis for comparison. For the geometric-step (varying coverage) method, the maximum number of steps and step sizes were calculated according to *(W-1)/2*, and in this experiment, the number of steps ranged from 4 to 6 (except when W=9), depending on the window size. For the arithmetic-step method, the number of steps was *(W-1)/2*. The number of steps of the divisor-step method depended on the available divisors of *(W-1)*, and it ranged from 4-11 (except when W=9) in this experiment. ICAMS was used to generate the simulated surfaces. ICAMS already has two built-in modules for the geometric-step (varying coverage) and arithmetic-step methods. The divisor-step method was programmed in MATLAB and was not yet available in ICAMS.

For each window size, the average estimated fractal dimension (D) was calculated and the root mean square errors between the estimated and the theoretical D were computed. The grand average values by fractal dimension for all window sizes are presented in Table 2.2.

Based on the average estimated D measure, the arithmetic-step method yielded an estimated fractal dimension much closer to the theoretical D for surfaces with low complexity (when $D<$ 2.5), whereas the divisor-step method yielded more accurate estimates for surfaces with high complexity (when $D>2.5$). This pattern can also be reflected by the average RMSE measure,

Table 2.2 Estimated fractal dimension and RMSE averaged for all 16 window sizes (from 17x17 to 69x69)

D	Geometric (varying)		Arithmetic		Divisor	
	Avg. D	Avg. RMSE	Avg. D	Avg. RMSE	Avg. D	Avg. RMSE
2.1	2.12	0.109	2.15	0.101	2.04	0.095
2.3	2.18	0.153	2.24	0.109	2.11	0.201
2.5	2.45	0.129	2.53	0.111	2.39	0.141
2.7	2.79	0.143	2.87	0.195	2.74	0.101
2.9	2.97	0.127	3.06	0.166	2.91	0.077
Grand Avg.		0.132		0.136		0.123

where the divisor method resulted in lower RMSE for surfaces with high complexity, and the arithmetic-step method yielded lower RMSE for surfaces with low complexity. The geometric-step method (varying coverage) ranks in the middle, with a grand average RMSE equals to 0.132, compared with 0.123 and 0.136 of the divisor-step and arithmetic-step methods, respectively.

A closer look of the results across window sizes provides further insights. Figure 2.4 plots the mean estimated fractal dimension from different algorithms at different windows.

From Figure 2.4, it can be observed that the geometric-step method (varying coverage) had the most unstable estimation across different window sizes and yielded the largest deviations from the theoretical values at most window sizes. The three peak points of the geometric-step method (varying coverage) corresponded to the three worst ECR and SDC in Table 2.1 (at windows 21x21, 45x45, and 61x61). This implies that the geometric-step (varying coverage) method tends to overestimate the fractal surface dimension (D=2.7, 2.9) when there is uneven or partial coverage among the steps. When the coverage is about the same as in the arithmetic-step

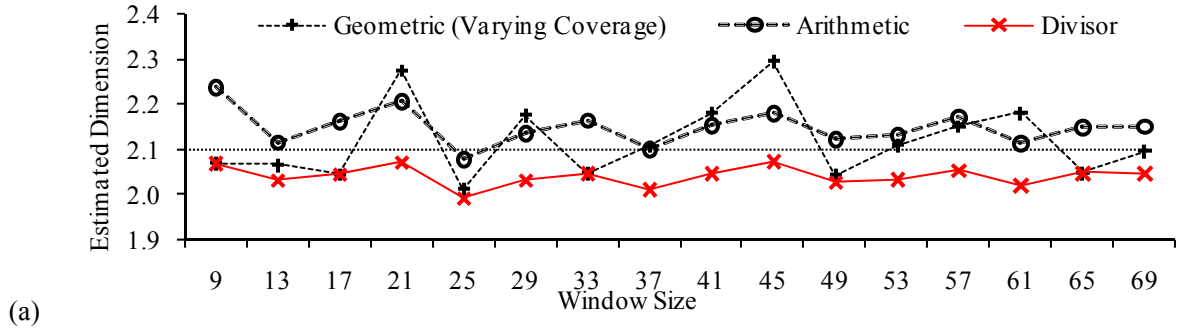

(a)

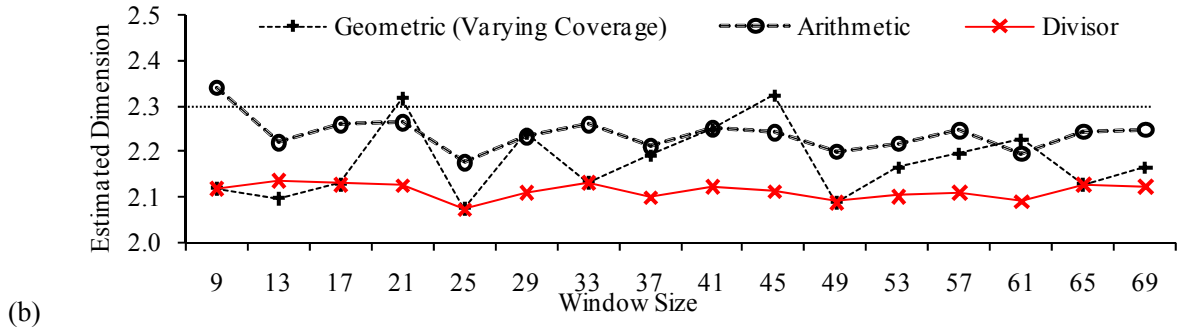

(b)

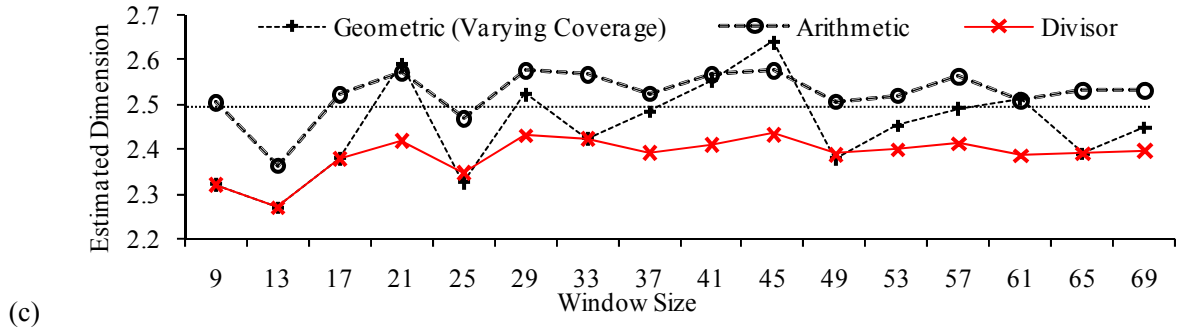

(c)

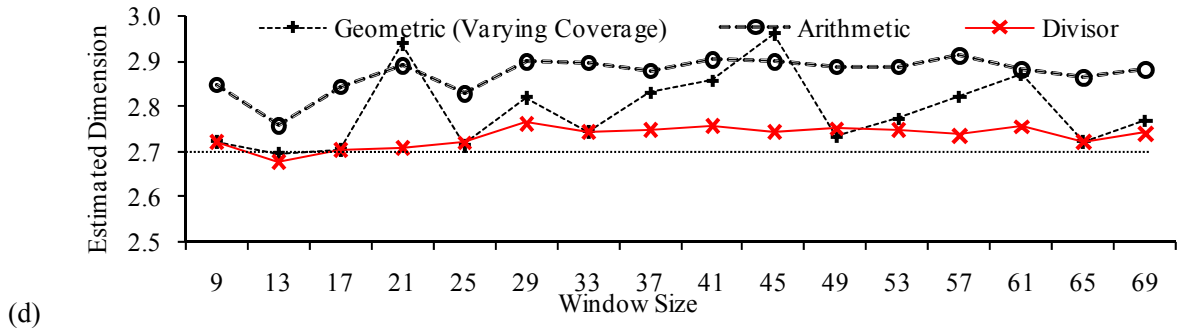

(d)

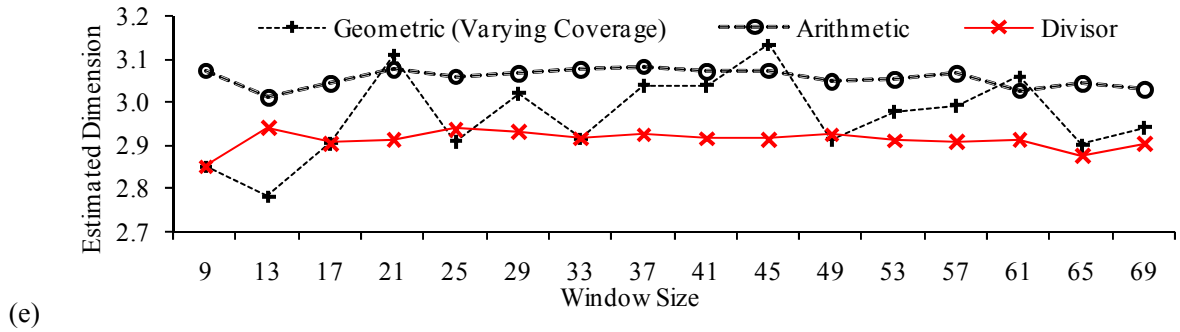

(e)

Figure 2.4 The mean estimated fractal dimensions derived from different methods, theoretical dimension shown in dashed straight line. (a) D=2.1; (b) D=2.3; (c) D=2.5; (d) D=2.7; (e) D=2.9.

divisor-step methods, the geometric-step (varying coverage) method yields similar fractal dimension values, as expected.

The arithmetic-step method consistently yielded higher estimated fractal dimension than the divisor-step method across all window sizes. The plot (Figure 2.4) further confirms that the arithmetic-step method is a more accurate estimator for low-complexity surfaces across all window sizes, whereas the divisor-method is more accurate for high-complexity surfaces. The estimates from the geometric-step (varying coverage) method fluctuate substantially across the windows, making this method far less desirable for fractal surface estimation.

The RMSE plots across windows (Figure 2.5) also show similar patterns. For surfaces with high-complexity (D=2.7, 2.9), the arithmetic-step method is clearly the worst due to high RMSEs and overestimation. The geometric-step (varying coverage) method also yielded high RMSEs, especially for windows with low ECRs and high SDCs (e.g., at 21, 45, and 61). The divisor-step method is generally the best for most windows. For surfaces with medium-low complexity (D=2.3, 2.5), the arithmetic-step method generally achieves the best RMSE for most windows. For surfaces with D=2.1, the arithmetic-step method is close to the divisor-step method.

Based on this experiment, we can conclude that the geometric-step method (varying coverage) is most unstable across different local windows and is less accurate than the others for most theoretical dimensions. Thus the method should be avoided in the future. The arithmetic-step method consistently yields a higher estimate than the other methods and is generally a better estimator for surfaces with medium-low complexity (D=2.3, 2.5), but it seriously overestimates the fractal dimension of surfaces with high complexity (D=2.7, 2.9). For D=2.9, the estimation consistently exceeds the theoretical maximum of 3.0. The divisor-step method is generally the best for surfaces with high complexity (D=2.7, 2.9) and very low complexity (D=2.1), but it

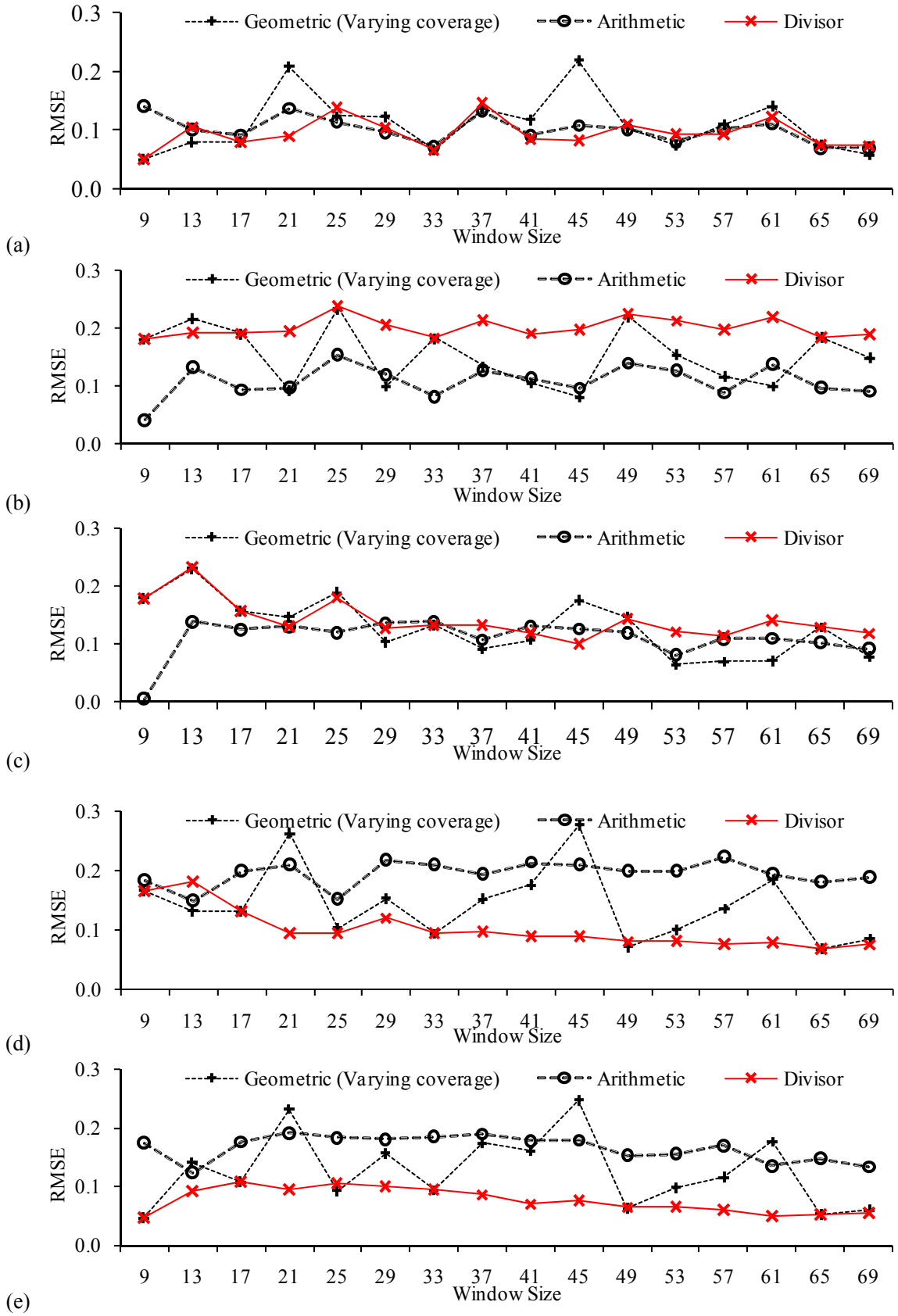

Figure 2.5 RMSE of different methods. (a) D=2.1; (b) D=2.3; (c) D=2.5; (d) D=2.7; (e) D=2.9.

underestimates for surfaces of medium and low complexity (for D=2.3 and D=2.5 with few exceptions).

2.5 Comparison with Real-World Data

To illustrate the effects of different algorithms in the real-world situation, a test was made using an IKONOS image (Figure 2.6a). The subset (252 x 252 pixels) is the near-infrared band of a typical urban residential neighborhood extracted from an IKONOS image of New Orleans, Louisiana. The image was taken in 2005. The bit depth is 11-bit, and the spatial resolution of the near-infrared band is 4 meters. The residential neighborhood exhibits a fractal appearance.

To visualize the difference among different sampling methods in generating fractal layers, a 21x21 pixel moving-window was applied to the subset to compute local fractal dimensions using different sampling methods. The 21x21 window size was picked because it was one of the three peak points at which the performance of the geometric-step method (varying coverage) was the worst (Figure 2.4). The use of this window size is expected to better illustrate the problem of the geometric-step method (varying coverage) visually.

The results were scaled to 0-255 for display (Figure 2.6). The overwhelming brighter appearance of the geometric-step (varying coverage) and arithmetic-step methods over the divisor-step method indicate higher estimated values, a finding similar to that of the simulated surface experiment. The standard deviations of the estimated local fractal dimensions were computed. For stretched images (Figure 2.6), the geometric-step method had the highest value (9.03), compared with 8.34 and 8.71 for the arithmetic-step and the divisor-step methods. Since the original image is quite self-similar (Figure 2.6a), it is expected local textures as reflected from the local fractal dimensions should be similar or stable across the image, hence the

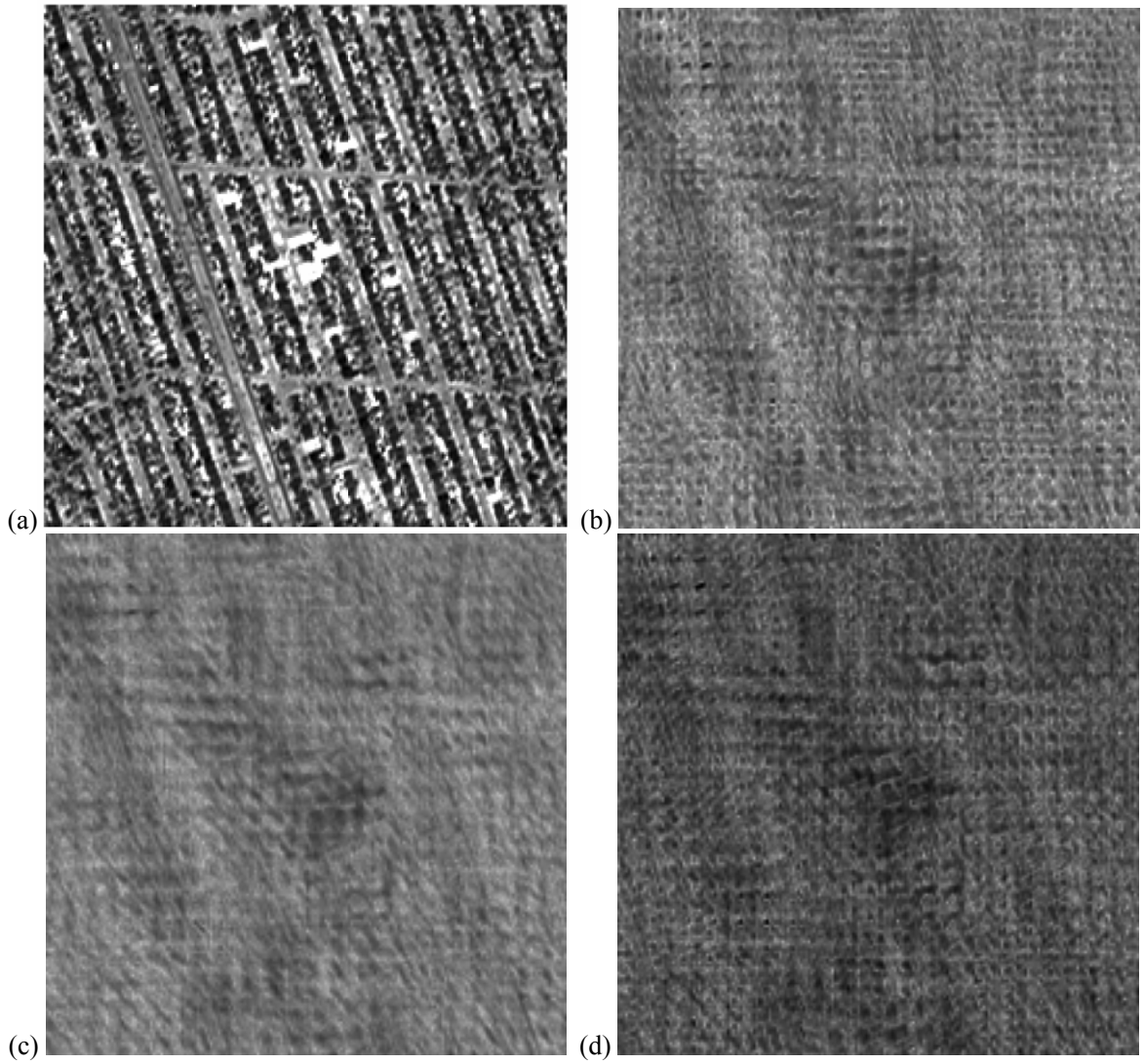

Figure 2.6 (a) An urban residential neighborhood (252x252 pixels) displayed using the near-infrared band of an IKONOS image from New Orleans, Louisiana, and fractal layers derived from using 21x21 moving-windows with different sampling methods; (b) geometric-step (varying coverage); (c) arithmetic-step; and (d) divisor-step. For (b)-(c), brighter pixels denote higher local fractal dimensions.

geometric-step method (varying coverage) can be interpreted as less reliable at this window size. It is noted that other factors such as variation of land cover, in addition to window size, may also contribute to higher standard deviation.

To further compare the estimated local fractal dimensions, 16 local windows ranging from 9x9 to 69x69 (in pixels) were used to derive fractal layers from the residential subset. As

different windows leave different edge portions uncalculated, the central 150 x 150 pixels were extracted from the resultant layers to provide the same basis for comparison. The average local fractal dimensions of each window size are listed in Table 2.3 and plotted in Figure 2.7.

Table 2.3 Average local fractal dimension of a residential neighborhood in New Orleans, LA

Window	Geometric (varying coverage)	Arithmetic	Divisor
9x9	2.52	2.67	2.52
13x13	2.51	2.68	2.59
17x17	2.65	2.79	2.65
21x21	2.84	2.85	2.68
25x25	2.64	2.87	2.72
29x29	2.77	2.90	2.72
33x33	2.74	2.93	2.74
37x37	2.84	2.93	2.77
41x41	2.87	2.95	2.76
45x45	2.95	2.96	2.78
49x49	2.73	2.97	2.80
53x53	2.80	2.98	2.80
57x57	2.82	3.00	2.79
61x61	2.88	3.00	2.83
65x65	2.81	3.00	2.81
69x69	2.85	3.01	2.82

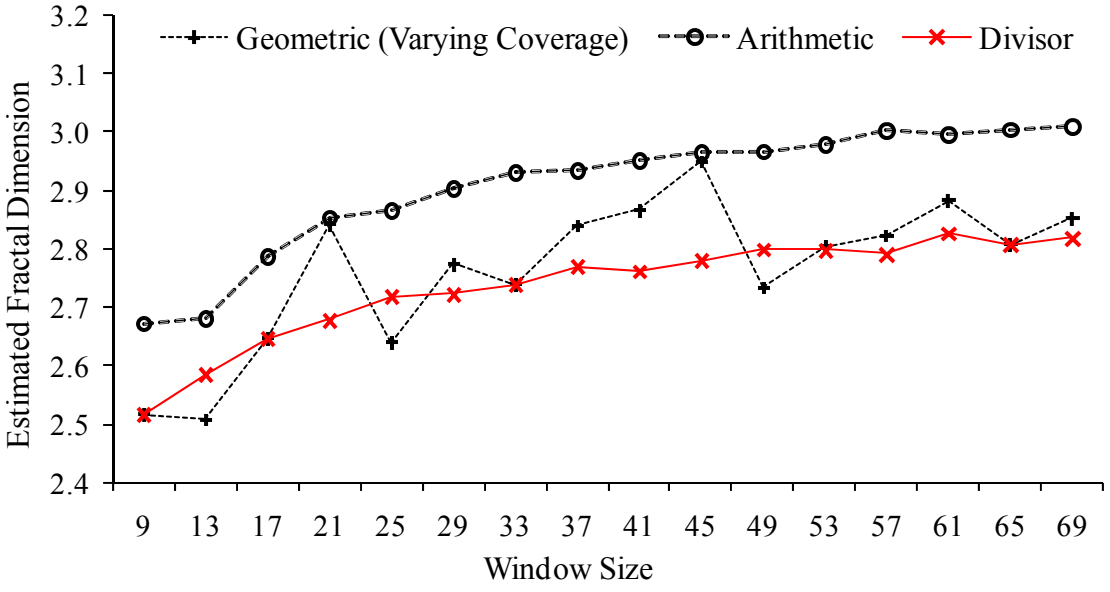

Figure 2.7 Average fractal dimension of an urban residential neighborhood measured from the near-infrared band of an IKONOS image in New Orleans, Louisiana.

Since this is a real-world dataset that does not have a known *D* value to serve as a benchmark, comparison of different methods cannot be based on the accuracy of estimated fractal dimensions. However, Table 2.3 and Figure 2.7 clearly show that the geometric-step (varying coverage) method resulted in higher fluctuations in the average local fractal dimensions across windows. This result is similar to the results found in the simulated surface experiment and can be attributed to the problem of different coverage sizes at different sampling steps. The fluctuation across windows, which may be attributed largely to the sampling method, complicates the interpretation of window size effects. It added an algorithm effect in addition to the window size effect (Sun et al. 2006). Both the arithmetic-step and divisor-step methods yielded fractal dimension estimates that increased gradually with increasing window size while approaching a stable stage at larger windows. Similar to the simulated surface experiment, the arithmetic-step method seems to overestimate the fractal dimension for larger windows, with values exceeding 3.0 when window size is 57x57 and greater. Hence, from this comparison, it

can be suggested that the divisor method is more preferable for real-world urban remote sensing application.

The above discussion has been focused on square images. In many geoscience applications, rectangular images are often used instead. Some other fractal dimension estimators can compute fractal dimensions of rectangular images easily, such as the isarithm and variogram estimators (Goodchild, 1980; Jaggi et al., 1993; Lam and De Cola, 1993). For the triangular prism method, the effects of sampling strategy on the resultant fractal estimates are expected to be greater for a rectangular image than for a square image. Equation 2 can also be applied to evaluate the effective coverage ratio of rectangular image. Consider a 151x201 image, by applying equation 2, the ECRs for different methods can be computed as: 54.8% for the geometric-step method (fixed coverage), 82.0% for the geometric-step method (varying coverage), 93.0% for the arithmetic-step method, and 100% for the divisor-step method (using common divisors of both sides). For irregular shapes, the triangular prism method would not be an effective method for computing the fractal dimension. Alternative methods such as the isarithm method should be considered.

2.6 Conclusions

Fractal dimension as an index has been widely used in geosciences, even though inconsistent results from different fractal estimators remain. Such inconsistencies could be a result of different sampling strategies applied to a fractal estimator. For local measurements where small windows are used, the impacts of different sampling strategies on the resultant fractal dimensions could be high. This paper introduces a new sampling strategy, called the divisor-step method, which can be applied to the triangular prism method to compute the fractal dimension. The divisor-step method is designed to fully utilize the entire study area (window) for all steps for calculation, so that part of the study area will not be wasted in the calculation.

Using 4,000 simulated surfaces and an IKONOS subset, the divisor-step method was compared with the two conventional approaches: the arithmetic-step and the geometric-step (varying coverage) methods. It was found that the geometric-step method (varying coverage) was less stable and less accurate than the other two methods for most theoretical dimensions and windows; hence it is not recommended for use by the triangular prism method. The arithmetic-step method consistently yielded a higher dimension than the other two methods. It performed better when the surfaces were of lower complexity, but for surfaces of high complexity (D=2.7, 2.9), the arithmetic-step method overestimated the fractal dimensions and sometimes yielded a value exceeding 3.0. On the other hand, the divisor-step method underestimated the fractal dimension values for surfaces of low complexity, but performed very well for surfaces of high complexity such as satellite images. The overall RMSE for the divisor-step method was also the lowest. Based on these results, it is recommended that the divisor-step method should be employed in fractal surface calculation algorithms especially for complex urban remote sensing image characterization. The divisor-step method can be easily programmed and implemented in any fractal estimation algorithms.

Chapter 3
Test of a New Lacunarity Estimator for Land Use Texture Analysis with IKONOS Imagery

3.1 Introduction

Because fractal dimension can measure the roughness of shape and objects, it has been widely used in image texture analysis (Emerson et al., 2005; Lam and De Cola, 1993; Liu and Cameron, 2001; Qiu et al., 1999; Turner and Ruscher, 1988). However, images that have the same fractal dimension may look very different. Lacunarity, a counterpart of fractal dimension, was proposed by Mandelbrot (1983) to describe this characteristic. Lacunarity is defined as the degree that a fractal deviates from transitional invariance (Gefen et al., 1984; Mandelbrot, 1983), and is an index of porosity. An image with higher lacunarity is more porous than an image with lower lacunarity (Figure 3.1). As the interpretation of transitional variance is relative to scale, lacunarity is a scale-dependent measurement and permits the analysis of scale effects. Recent applications of lacunarity in geographical and environmental studies have shown that lacunarity can be a promising geospatial analytic tool (Dale, 2000; Greenhill et al., 2003; Henebry and Kux, 1995). In image classification, lacunarity was found to outperform fractal dimension (Dong, 2000; Myint and Lam, 2005a).

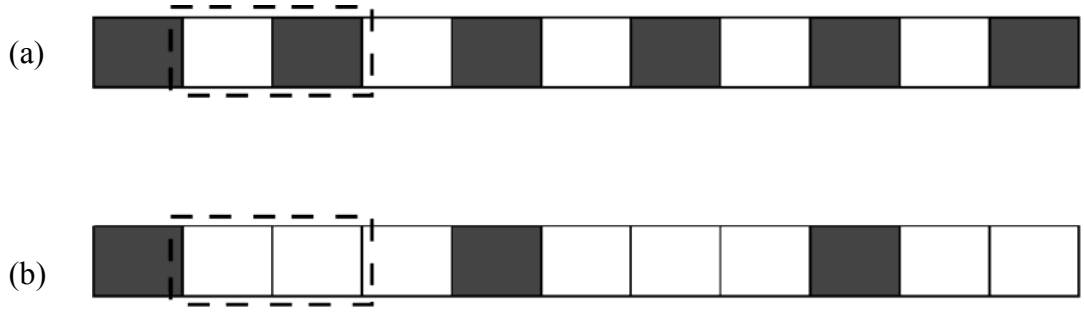

Figure 3.1 Demonstration of lacunarity, using the gliding-box algorithm. (b) is more porous (i.e. higher lacunarity) than (a) with a 1 x 2 gliding-box.

Several mathematical definitions and algorithms for calculating lacunarity have been suggested in the early literature (Gefen et al., 1984; Lin and Yang, 1986; Mandelbrot, 1983). Over time, more practical and efficient methods have been proposed. Voss (1986) devised a probabilistic modification to the box counting method (PBC) for calculating lacunarity by interpreting the mass as the number of points in the *three*-dimensional box which is positioned in the image intensity space. Allain and Cloitre (1991) presented a gliding-box algorithm to calculate lacunarity. Plotnick et al. (1996) extended the use of lacunarity to non-fractal real datasets with the gliding-box algorithm. Dong (2000) proposed a differential box counting (DBC) that uses the gliding-box algorithm, and the DBC method was found to perform better than the PBC method in separating selected Brodatz textures (1966). The method was later modified to reduce the intensity sensitivity of lacunarity measurement by Du and Yeo (2002) and used for SAR image segmentation. Myint et al. (2006) compared the original gliding-box approach (overlapping boxes) with an alternative implementation (skipping boxes) and found the overlapping-box approach to be more effective than the skipping-box approach for the DBC method in urban mapping with IKONOS imagery.

Gray-scale lacunarity algorithms are closely related to and derived from fractal algorithms. Both PBC and DBC methods are based on different versions of box counting methods. As Lam et al. (2002) found that the triangular prism method was the best to estimate fractal dimensions; it is possible to derive a good lacunarity estimator based on it. In this paper, using a gliding-box algorithm, a new lacunarity estimation method based on the triangular prism (TP) method is proposed. The new method is compared to two widely-used gray-scale lacunarity estimators, PBC and DBC, utilizing several land-use/land-cover (LULC) textures extracted from an IKONOS image of New Orleans, Louisiana. The image was taken in 2005.

3.2 Gray-Scale Lacunarity Estimators

3.2.1 Voss's Probabilistic Box Counting (PBC) Method

Voss (1986) proposed an approach that uses empirically-derived probabilistic mass distribution to estimate both fractal dimension and lacunarity. In his method, an image is treated as a set of point arrays at position *(x, y)* with the number of points over each pixel being the z-value of the pixel (Figure 3.2). All points have the same probability to be the center of an *r* x *r* x *r* cube (or a sphere with radii = *r*) inside of the image intensity space. The mass of a cube is measured by the number of points included. If we let the probability of a cubic having mass *m* be *Q(m,r),*

$$\sum_{m=1}^{n} Q(m,r) = 1 \tag{1}$$

where *n* is the maximum mass of a cube given *r*.

Lacunarity ($\Lambda(r)$) is usually defined as the following:

$$\Lambda(r) = \frac{\sum_{m=1}^{n} m^2 Q(m,r)}{(\sum_{m=1}^{n} mQ(m,r))^2} - 1 \tag{2}$$

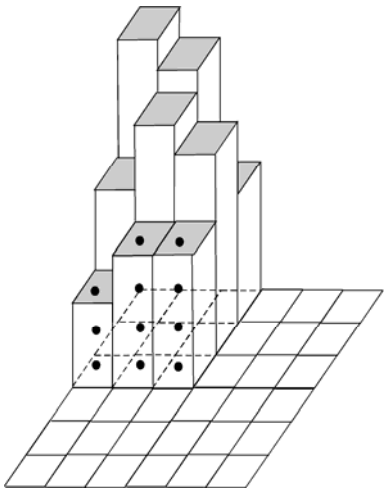

Figure 3.2 Demonstration of the extruded image space, number of points equal to the z value.

3.2.2 Dong's Differential Box Counting (DBC) Method

This algorithm is based on the gliding-box algorithm (Allain and Cloitre, 1991), which is widely used to analyze binary images. Consider a square box of radius *r* which glides on a lattice; its center is placed over all possible points with the coverage of the box bounded by the *(x,y)* extent of the underlying lattice (Figure 3.3). Let *n(m,r)* denote the number of gliding-boxes with radius *r* and mass *m* and let *N* denote the total number of gliding-box. Then *Q(m,r)* is the probability of a box having a mass *m*, or

$$Q(m,r) = n(m,r) / N \tag{3}$$

The lacunarity at a given scale *r* can be defined as the mean-square deviation of the fluctuations of mass distribution probability *Q(m,r)* divided by its square mean (Allain and Cloitre, 1991):

$$\Lambda(r) = \frac{\sum_{m=1}^{n} m^2 Q(m,r)}{(\sum_{m=1}^{n} mQ(m,r))^2} \tag{4}$$

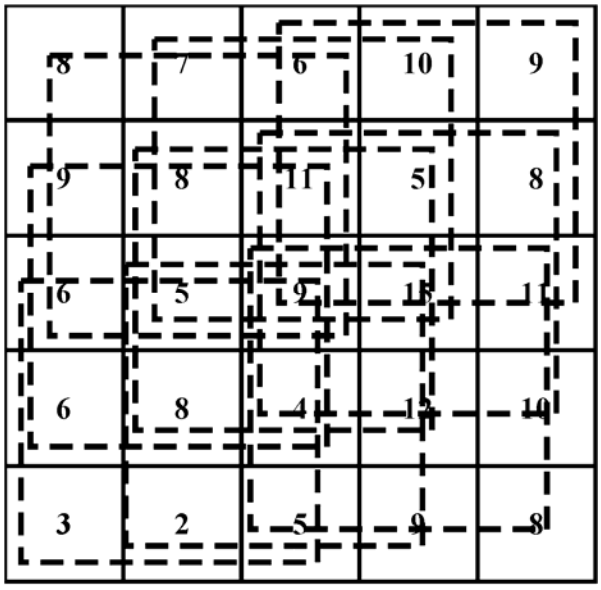

Figure 3.3 Demonstration of the gliding-box algorithm.

Although equation (3) is slightly different from equation (2), because the difference is a constant -1, it does not affect the interpretation of the value. Equation (2) is used as the only mathematical definition for all calculations in this paper. The minimum lacunarity value is 0 when the image exhibits an even mass distribution (uniform surface).

Based on the gliding-box algorithm and the DBC method (Sarkar and Chaudhuri, 1992), Dong (2000) proposed a new interpretation of box mass. Let a gliding-box r x r glide over the image, and each gliding-box corresponds to a part of the image intensity space. Stack the cube r x r x r to fill the corresponding image intensity space. Assign numbers 1, 2, 3 … to the boxes from the bottom level to the top level. Let u and v represent the top box levels of the maximum gray scale pixel and the minimum gray scale pixel respectively. The relative height of the column is:

$$h(i, j) = u - v - 1 \tag{5}$$

$h(i, j)$ is assigned to the corresponding gliding-box *(i,j)* and is treated as its mass in equation (2). As the equation (5) may cause negative height values, Myint *et al.* (2006) changed it to:

$$h(i, j) = u - v + 1 \tag{6}$$

3.3 The New Method

3.3.1 Triangular Prism (TP) Method

The triangular prism method was proposed by Clarke (1986) as a means to calculate fractal dimension. As documented in some benchmark tests (Lam et al., 2002; Zhou and Lam, 2005), a slightly modified version of the TP method was found to be more effective than the box counting method, Fourier spectrum, variogram method, and probabilistic method in characterizing fractal dimension. In the TP method, image pixels are treated as a set of elevated points floating over the image *(x,y)* plane. Starting from the upper-left corner of an image, given a step size r, a triangular

prism can be constructed by connecting four corner points with the center point which carries the average *z* value of the corner points (Figure 3.4a). Similarly, other prisms can be constructed all over the image without overlapping among the prisms (Figure 3.4b). Fractal dimension can be estimated from the double-log regression between the total triangular prism surface area and the step size (Lam et al., 2002; Zhao, 2001).

$$LogA=a+bLogS \tag{7}$$

Where A is the total area of the top surfaces of triangular prisms, S is the step size, a is the intercept, b is the regression slope. Fractal dimension is 2-b.

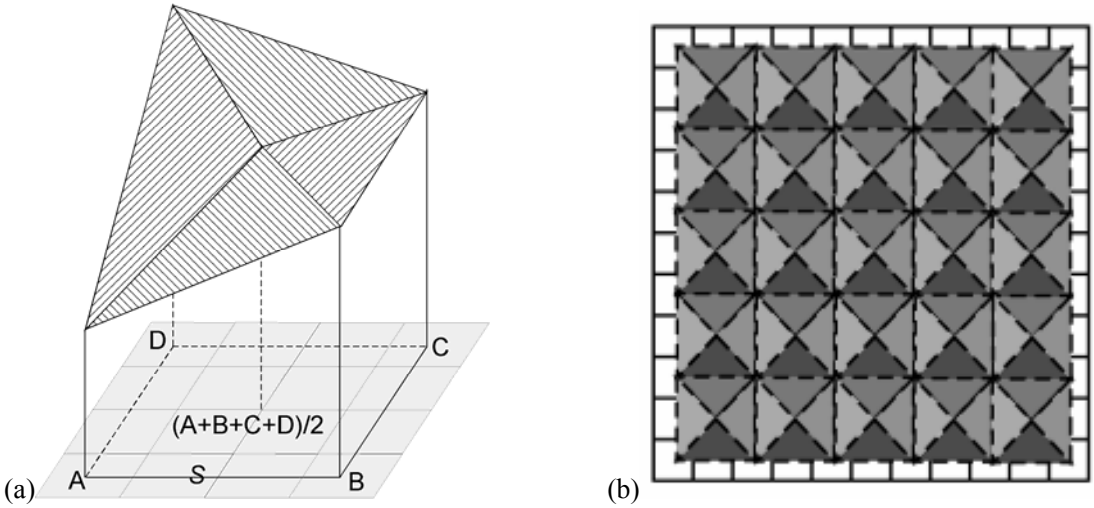

Figure 3.4 (a) A triangular prism; (b) Triangular prisms over the image.

In the following implementation for lacunarity estimation, triangular prisms are placed one column or row next to each other such that each triangular prism corresponds to a gliding-box (Figure 3.3) on the image. The image roughness inside of a gliding-box can be quantified by the ratio of the surface area of the triangular prism to its projected area on the image *(x,y)* plane. This is in analog to the DBC method, where relative height is standardized by the edge length of the gliding-box. In TP method, the TP surface area is standardized by the area of the gliding-box. The following equation applies:

$$m(i,j) = ceil(A(i,j)/(r \times r)) \quad (8)$$

This measurement can be interpreted as the number of patches (area: r x r) required to cover a triangular prism surface. This number of patches *m(i,j)* fluctuates across the image and can be used as a substitute to box mass in equation (2).

3.3.2 A Worked Example

The calculation process is illustrated in a worked example for a 5x5 4-bit image (Figure 3.5a) with r=3.

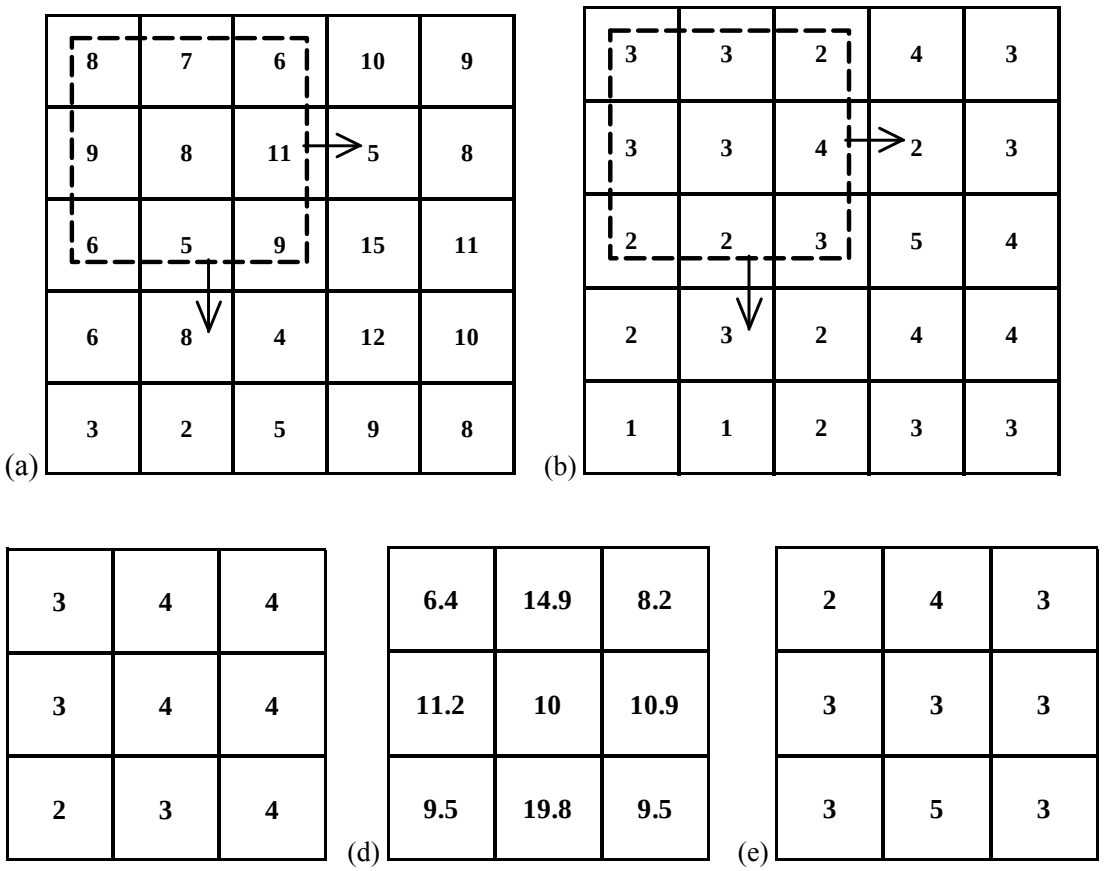

Figure 3.5 A worked example of the new lacunarity estimator. (a) original 5x5 4-bit image; (b) box levels needed for each pixel using the DBC method; (c) box mass distribution matrix using the DBC method; (d) TP surface area of each gliding-box using the TP method; (e) box mass distribution matrix using the TP method.

For the DBC method, the first step is to stack 3x3x3 cubic, equivalent to scaling the image by 1/3 (Figure 3.5b). Starting from the upper-left corner, a 3x3 box glides through the image by moving a row or a column next to the current location. In each gliding box, the differential box level is calculated (Figure 3.5c). *Q(m,r)* is 1/9, 3/9, and 5/9 for *m*=2, 3, and 4 respectively, and 0 for other *m* values. The lacunarity for DBC method is:

$(2x2x1/9 + 3x3x3/9 + 4x4x5/9) / (2x1/9 + 3x3/9 + 4x5/9)^2 - 1 = 0.0395.$

For the calculation of the above example with TP method, the first step is to construct triangular prisms. Starting from the upper-left corner, a triangular prism is constructed from the four corner pixels of the gliding-box. With the box gliding on the image, overlapping triangular prisms will be constructed, consisting of four triangular facets for each triangular prism. The area of a triangular facet can be derived using the Heron's formula:

$$A = \sqrt{s(s-a)(s-b)(s-c)}, \quad s=(a+b+c)/2 \qquad (9)$$

The triangular prism surface area of each gliding-box is calculated accordingly (Figure 3.5d). The area is then scaled by the square of the triangular step *(r-1)* and the box mass distribution is derived (Figure 3.5e). *Q(m,r)* is 1/9, 6/9, 1/9, and 1/9 for *m*=2, 3, 4, and 5 respectively, and 0 for other *m* values. The lacunarity is:

$(2x2x1/9 + 3x3x6/9 + 4x4x1/9 + 5x5x1/9) / (2x1/9 + 3x6/9 + 4x1/9 + 5x1/9)^2 - 1 = 0.0595.$

Detailed calculation examples of Voss's method can be found in recent literature (Myint and Lam, 2005b).

3.4 Experiments with an IKONOS Image

To test the suitability of different lacunarity estimators in LULC research, four 252x252 pixels land use patches extracted from the green, red, and near-infrared multispectral bands of an IKONOS image (taken in 2005) in New Orleans were used here. These subsets are shown in

Figure 3.6. IKONOS images have an 11-bit radiometric resolution and 4-meter spatial resolution on the multispectral bands.

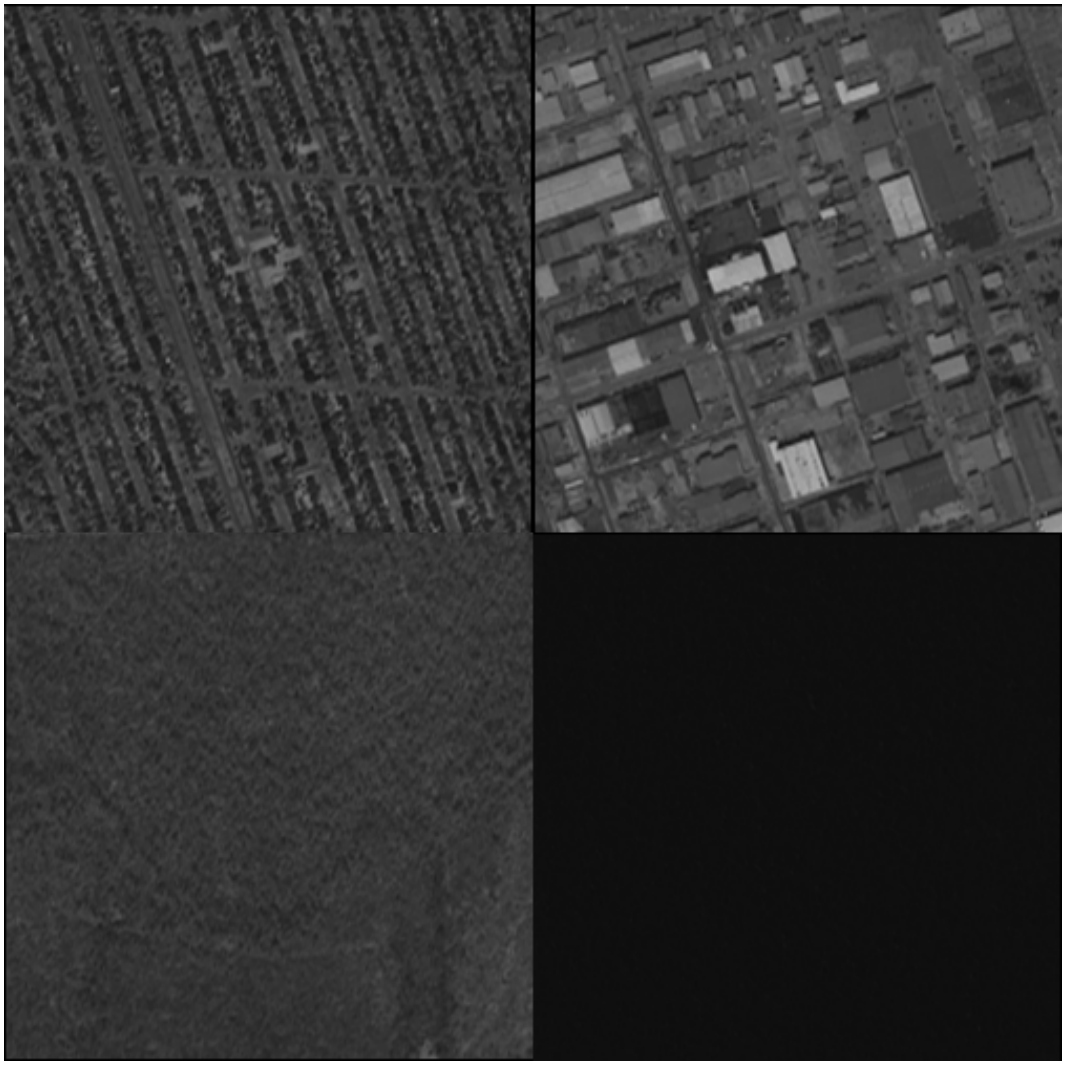

Figure 3.6 Land-use/land-cover extracted from an IKONOS image in New Orleans, LA. Clockwisely from upper left are, residential, industrial/commercial complex, water, and forest. Shown in the near-infrared band. Image taken on Sep. 2, 2005.

The new method using triangular prism surface patch counting was compared to PBC (Voss, 1986) and DBC (Dong, 2000) methods. The original gliding-box implementation (overlapping boxes) was used in this research as it is superior to the skipping approach (Myint et al., 2006). In the experiment, 3000 pattern samples (each sample is a w x w window of the land use subset) were randomly selected from each land cover (residential, industrial/commercial, water, or forest)

and lacunarity values from the three multispectral bands were calculated. A random subset containing 2000 samples were used to train the maximum likelihood classifier and the remaining 1000 samples were used as test data. The three lacunarity layers computed from each of the three spectral bands were stacked together in each classification test. Following Myint et al. (2006), three window sizes were selected to extract texture samples: w=15, 19, and 23 pixels, equivalent to 60x60, 76x76, and 92x92 meters. As box edge length *r* plays an important role in measuring the gappiness of mass distribution, three different *r*, 3, 5, and 7 pixels were used. The sampling-test process was repeated 50 times to derive mean accuracies. In addition to classification, the lacunarity values of different LULC categories from different algorithms were also compared.

3.4.1 Accuracy and Robustness

The mean overall classification accuracies are listed in Table 3.1-3.3. In most cases, the accuracies from PBC and DBC decreased when increasing *r*, and the best accuracies were achieved using a small *r* (*r*=3), which agreed with previous findings (Myint and Lam, 2005a). The new method was slightly better than DBC when *r* = 3. For bigger *r* (5 or 7), the new method outperformed both PBC and DBC in terms of separating different land use textures. When performing classification based on the composite lacunarity feature set (*r*=3,5,7 from three different bands), the relative rank according to accuracy is: TP>DBC>PBC. Kappa statistics results are shown in Table 3.4. It can be found that the improvement from the PBC or DBC method to the TP method is significant at 0.05 significance level (z=1.96), with very few exceptions when *r*=3. Accuracy generally increased along with sample window size (except PBC), due to better characterization of distinctive texture with a larger sample window. It should be noticed that the edge effects due to multi- class coverage by a window was largely eliminated in this research by using texture mosaics.

Table 3.1 Overall classification accuracies: industrial/commercial complex, urban residential, water, and forest. Window=15x15 pixels

r	PBC	DBC	TP
3	58.5	60.3	61.7
5	53.6	46.5	57.2
7	51.4	39.8	60.7
Composite	57.8	61.4	63.0

Table 3.2 Overall classification accuracies: industrial/commercial complex, urban residential, water, and forest. Window=19x19 pixels

r	PBC	DBC	TP
3	57.9	64.7	67.0
5	54.5	49.3	60.8
7	51.1	43.2	66.5
Composite	55.4	62.0	65.5

Table 3.3 Overall classification accuracies: industrial/commercial complex, urban residential, water, and forest. Window=23x23 pixels

r	PBC	DBC	TP
3	56.3	70.0	70.9
5	54.0	52.9	64.7
7	52.9	46.2	71.8
Composite	54.4	63.5	66.2

Table 3.4 Kappa Z statistics of the TP method over the PBC and DBC methods.

r	TP VS PBC			TP VS DBC		
	w=15	*w*=19	*w*=23	*w*=15	*w*=19	*w*=23
3	6.25*	10.69*	1.37	1.76	15.36*	0.73
5	4.20*	6.75*	9.43*	8.82*	12.35*	12.71*
7	10.62*	15.94*	20.79*	22.59*	17.47*	23.63*
Composite	6.42*	10.19*	2.01*	4.19*	11.81*	2.77*

*: significant at 0.05 level (Z>1.96)

The 252x252 forest subset was used to compare the computational cost of different algorithms. The computational environment was a Sun Microsystems workstation equipped with Dual-Core AMD Opteron 280 processor (2.41GHz) and 4GB RAM. For each algorithm, the derivation of local lacunarity using *w*=15 and *r*=3 was run 50 times in order to achieve an average estimation. The average cost was 3.3 seconds for DBC, 6.0 seconds for TP, and 282 seconds for PBC. Thus the new method, although less cost efficient than DBC, is computationally much more efficient than PBC.

3.4.2 Inconsistent Lacunarity Interpretations among Different Methods

Three box plots (Figure 3.7) demonstrate the distributions of lacunarity of different LULC types, when calculated by the three different methods. For each LULC category, lacunarity values were derived from the near-infrared band using a 15x15 pixels window and *r* =3. By observation, the three methods agreed on the tighter distributions of residential, forest, and water than industrial/commercial complex, but the distribution of residential land calculated by both the TP and DBC methods were even tighter than the one from the PBC method. The TP method

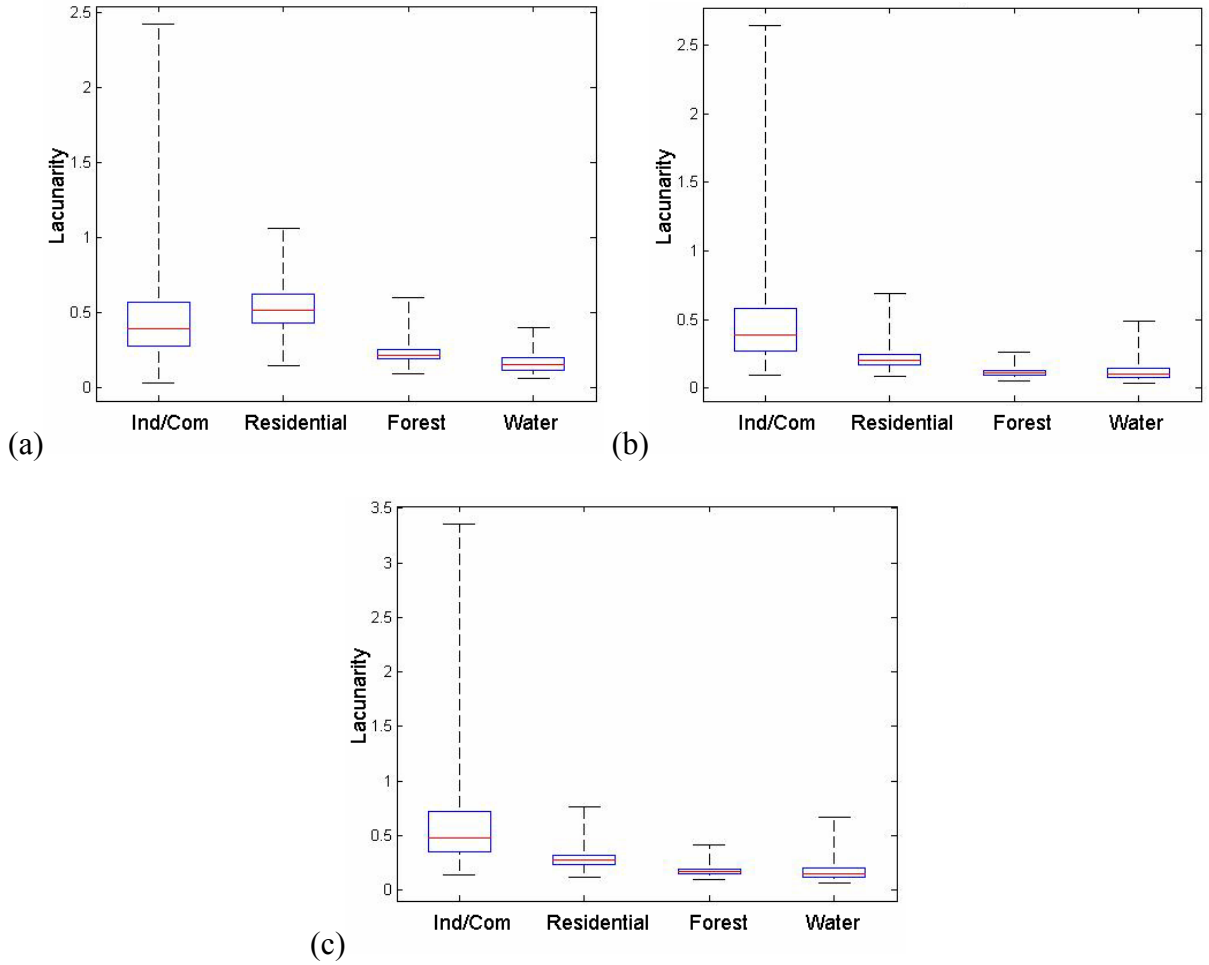

Figure 3.7 Box plots of the distribution of lacunarity. (a) PBC; (b) DBC; (c) TP. Minimum and maximum values are shown in bars connected by dashed lines. Center half (2nd and 3rd quarters) are bounded by boxes. Median values are shown in the line inside of the boxes.

derived a bigger maximum value for industrial/commercial land than the DBC and PBC methods. The biggest difference among different methods is probably the ranking of these LULC categories per their median values. This difference is crucial for lacunarity estimation as it affects the interpretation of lacunarity of different images. This disagreement among different methods will be addressed further in the following paragraph using mean values from different bands.

As lacunarity measures porosity, the question arises as to which LULC is more lacunar? To illustrate this question, the mean measurement of industrial/commercial, residential, water, and forest using r=3 and w=15 is demonstrated in Figure 3.8.

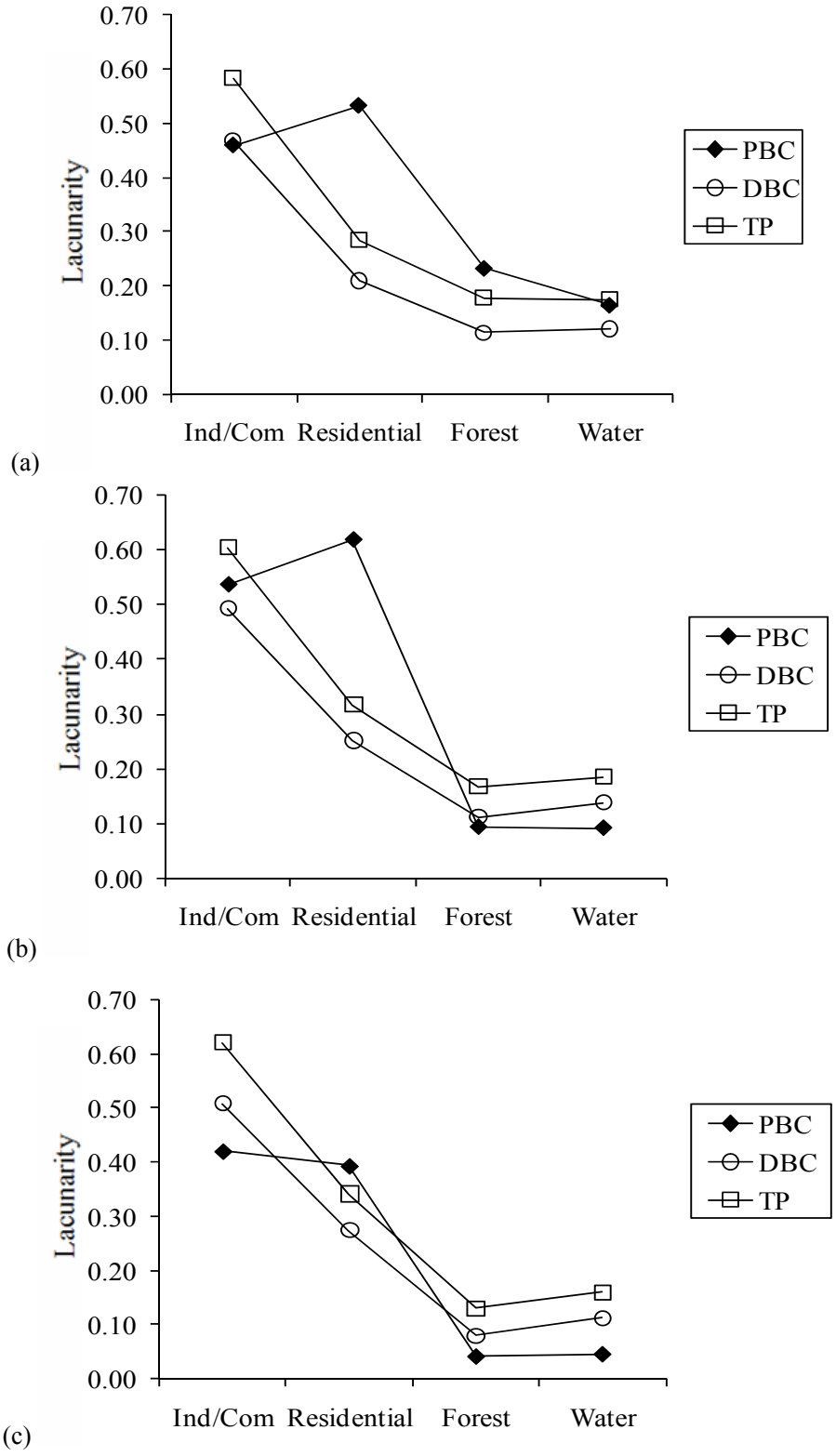

Figure 3.8 Mean lacunarity measurements of selected USGS Level I&II land-use/land-cover textures from the near-infrared band of an IKONOS image, w=15, r=3. (a) band4; (b) band3; (c) band2.

Both TP and DBC methods agreed on the lacunarity ranking of all land use categories, but the PBC method ranked them differently. For the red band and near-infrared band, while the industrial/commercial complex was found less lacunar than residential land based on the PBC method, it was more porous based on the DBC and TP methods. Similar trends can be observed for forest and water. The dichotic ranking is possibly due to the different utilization of pixel intensity. In the PBC method, boxes fill the entire image intensity space and hence the absolute intensity information is used. DBC is based on the relative height of boxes; TP is based on the top surface of triangular prisms; hence both DBC and TP utilize the relative intensity information. Some geographical data (interval but not ratio type) such as DEM only have relative height information available, thus only TP and DBC are theoretically more applicable to measure topographical lacunarity than PBC.

3.5 Experiments with Computer Simulated Fractals

As revealed by the first experiment, the lacunarity ranking of different LULC categories varied by measuring algorithm. To further address this inconsistency, a set of computer simulated fractals were tested in this experiment.

3.5.1 Shear Displacement Algorithm

One commonly used computer algorithm to generate the fractional Brownian motion (fBm) surface is the shear displacement method (Goodchild, 1980; Mandelbrot, 1975). The algorithm starts with a flat surface and randomly cuts and shifts the surface with the position of cut controlled by a random process and the magnitude of shift controlled statistically by a persistence factor related to fractal dimension (Zhou and Lam, 2005). The process repeats until a number of cuts are satisfied. Graphic interface of this algorithm is provided in Image Characterization And Modeling System (ICAMS, Lam et al., 1998; Quattrochi et al., 1997).

For this test, four 257x257 images were generated with 300, 600, 900, and 1200 cuts respectively, at the same theoretical fractal dimension (2.5). ICAMS automatically stretched these images to 0-255. As the numbers of cuts were different, they exhibited a different appearance (Figure 3.9) with different mass distributions. Lacunarity could quantify their difference. All three gray-scale lacunarity estimators were applied to the four images globally using r=3 and the lacunarity of each image was ranked.

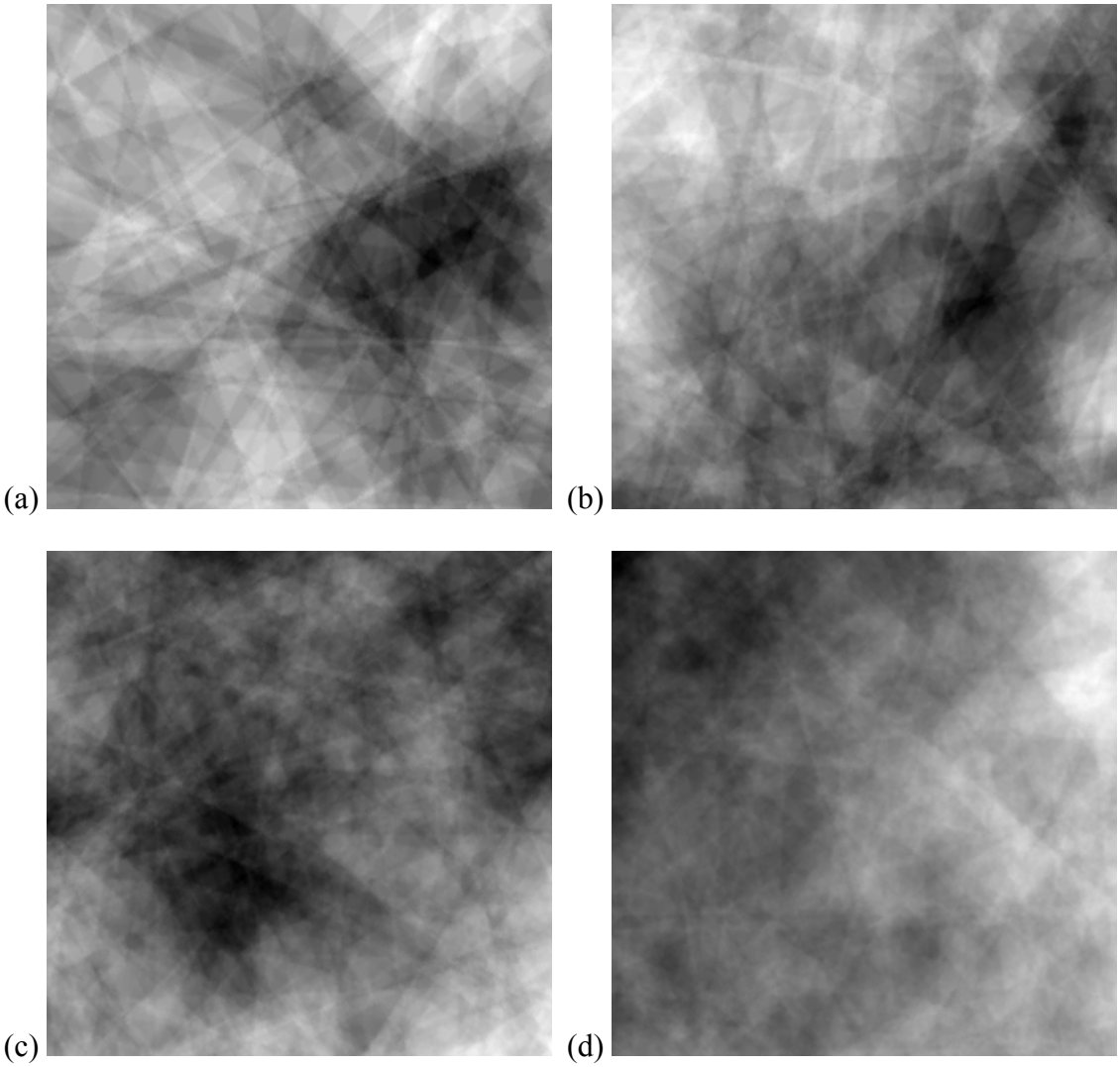

Figure 3.9 Computer simulated fractals with shear displacement algorithm. Theoretical fractal dimension is 2.5 for all images. (a) 300 cuts; (b) 600 cuts; (c) 900 cuts; (d) 1200 cuts.

3.5.2 Lacunarity Ranking of Fractal Set

The average lacunarity are plotted in Figure 3.10. As different algorithms use different mass interpretation, the absolute lacunarity values are not comparable and focus is given to the relative ranking. The ranking of three different fractals were the same for TP and DBC, but different for PBC. Thus, the inconsistency of lacunarity interpretation among different algorithms in real-world IKONOS remote sensing data was reproduced with computer simulated fractals. In a random survey of 5 people, 4 of them conceived that Figure 3.9a was more heterogeneous than Figure 3.9b. This is probably because more cuts could make the visual appearance transition across the simulated surface smoother, thus both TP and DBC methods seem to better describe the "gappiness" decreasing trend from less cuts to more cuts.

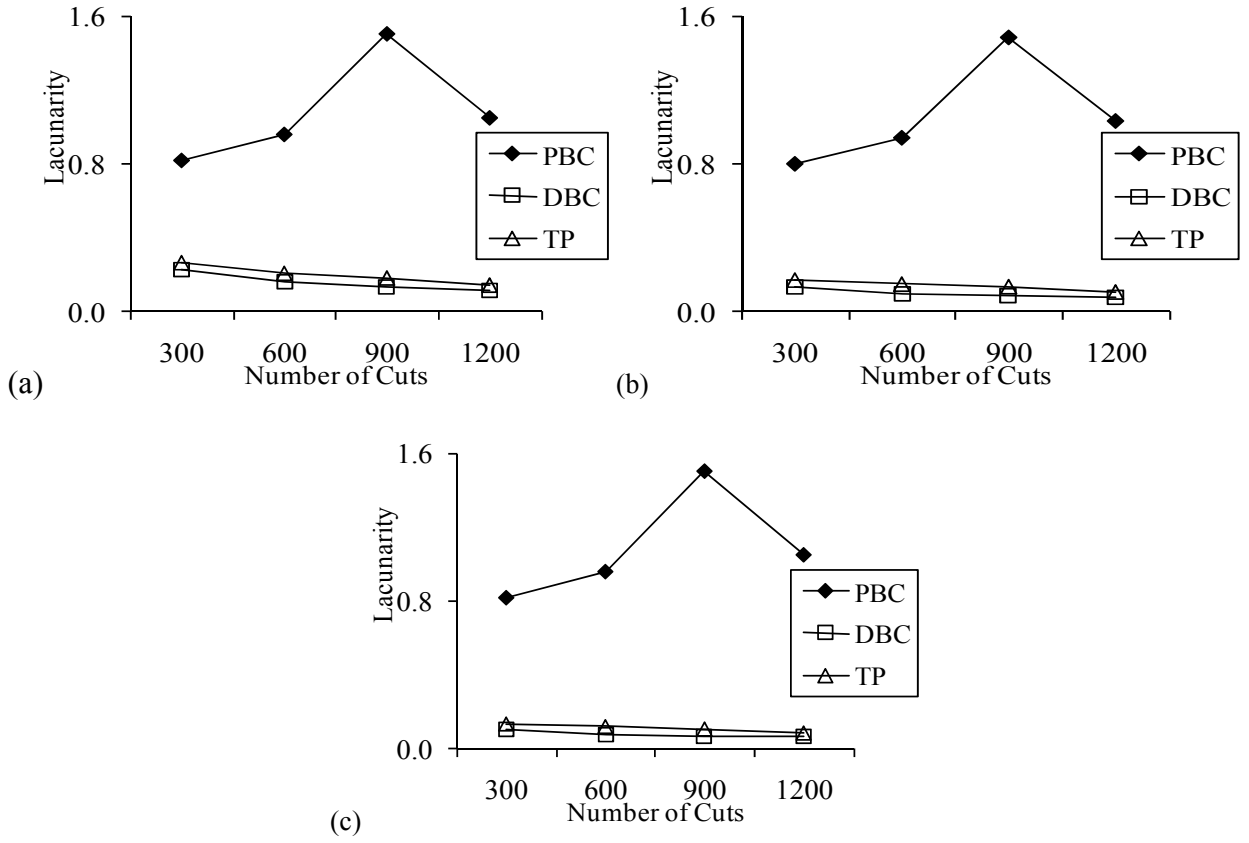

Figure 3.10 Lacunarity measurements of three different fractals with different number of cuts. Theoretical fractal dimension is 2.5 for all images. (a) r=3 (b) r=5 (c) r=7.

3.6 Conclusions

Lacunarity reflects the degree of heterogeneity and has the capability of discriminating image textures. This research provides a new lacunarity estimator based on the gliding-box algorithm (Allain and Cloitre, 1991) and the fractal TP method (Clarke, 1986). Experiments with four industrial/commercial, residential, water, and forest land covers extracted from high-resolution IKONOS imagery found that lacunarity features derived with the new method led to better classification accuracy than the PBC (Voss, 1986) and DBC (Dong, 2000) methods, partially due to the better accuracy of the TP method over other methods (Lam et al., 2002; Zhou and Lam, 2005). Both TP and DBC are more computationally efficient than PBC. Based on the advantage of accuracy and computational efficiency, the new method is more suitable to differentiating different LULC categories with high-resolution IKONOS imagery.

A very intriguing problem is discovered by analyzing the lacunarity values of different LULC categories with different methods. While TP and DBC agree on the ranking of lacunarity of the four LULC categories, the PBC method provides a different result. Experiments found that industrial/commercial texture could be more or less heterogeneous than residential land texture, depending on the estimator. Similar trends can be found for forest and water. The ranking difference coincides with the dichotic utilization of pixel intensity information: relative or absolute. As it was recently found that the similar problem exists in binary lacunarity estimators (Pendleton et al., 2005), this work reveals the unpleasant problem in gray-scale lacunarity estimators: the inconsistent interpretation of “gappiness”. A further investigation with computer generated fractals also found the same inconsistency among different estimators. For computer simulated fractals, both TP and PBC methods are more likely to fit the transition trends for fractals with less cuts to those with more cuts. Further benchmark tests with theoretical gray-

scale fractals with known gap distribution are needed to address the relative goodness of different methods and effects of spatial resolution, radiometric resolution, data type (interval versus ratio), as well as deriving a robust and accurate estimator.

Chapter 4
Effects of Window Size on Texture-Aided Land-Use/Land-Cover Classification

4.1 Introduction

Land-use/land-cover (LULC) classification is facing great challenges with recent advances in high-resolution satellite sensors such as IKONOS, QuickBird, and WorldView-1. The new meter or sub-meter level spatial resolution provides great ability of identifying ground features but also complicates LULC classification by aggregating physical components with varying spectral responses in a single LULC category. With higher potential resolution, on one hand USGS level II or III classifications (Anderson et al. 1976) are made possible, on the other hand LULC categories now have more in-class heterogeneity and more between-class overlap. The traditional per-pixel maximum likelihood method has been shown to be insufficient to cope with this problem (Huang et al., 2002; Myint and Lam, 2005a). The problem of classifying high-resolution imagery has been dealt extensively with using neighborhood spatial/textural analysis.

For the texture approach, the rationale is that different land use categories can have distinctive textural appearance even though they may have the same per-pixel spectral responses. By taking this important neighborhood information into account, various textural indices can be applied to improve classification, such as simple statistical variance (Chen et al., 2004), fractal dimension (Chust et al., 2004; Emerson et al., 2005; Myint and Lam, 2005a; Qiu et al., 1999; Read and Lam, 2002), lacunarity (Dale, 2000; Dong and Leblon, 2004; Greenhill et al., 2003; Henebry and Kux, 1995; Myint et al., 2006), semivariogram (Carr and de Miranda, 1998; Miranda et al., 1998), spatial autocorrelation Moran's *I* (Emerson et al., 2005), and compactness and smoothess in object-based approach (Hu et al., 2005; Mitri and Gitas, 2004; Yu et al., 2006). A number of statistical attributes were not only used in original bands, but also applied to

transformed images after texture analysis such as gray-level co-occurrence matrix (Carr and de Miranda, 1998; Jobanputra and Clausi, 2006) and wavelet transform (Myint et al., 2004; Zhu and Yang, 1998).

For texture-aided classification, a commonly-used technique to extract texture information from images is to use a square moving window. The measurement inside of a local moving window is then assigned to its central pixel as additional feature to describe neighborhood environments. These extracted neighborhood measurements are stacked with spectral features to improve classification accuracies. The size of moving window plays a key role in this technique as it affects the stability of measurement and causes blurring effects and boundary effects. A number of previous studies have examined this problem by using different indices, different images, different study areas and different classification schemes. In a case study with Digital Orthophoto Quarter Quadrangle (DOQQ) images, Chen et al. (2004) tested simple variance with windows ranging from 3x3 to 11x11 for a series of images at different resolutions (4-24m), and found that 5x5 (20x20 meters) window was the best for the 4m- resolution image while 3x3 (24x24 meters) window was the best for the 8m-resolution image. In a study using Landsat Enhanced Thematic Mapper plus (ETM+) panchromatic band, Emerson et al. (2005) demonstrated that a 21x21 (315x315 meters) window was most suitable for fractal dimension, while a 7x7 (105x105 meters) window was good for local variance. In studies with IKONOS imagery, Myint and Lam (2005b) found that a 29x29 (116x116 meters) moving window was better than 13x13 and 21x21 for lacunarity (method due to Voss, 1986) but suggested further investigation, while Myint et al. (2006) suggested that very minor difference existed in window 15x15, 21x21, and 27x27 for lacunarity (method due to Dong, 2000). It can be inferred from these studies that an optimal window or a range could exist for a certain index and sensor. Such

an optimal window means a turning point of texture-aided classification, where classification accuracy reaches the highest level.

Compared to simple statistical textural indices that do not reflect inside spatial distribution of different pixel values such as variance, standard deviation, and entropy, another category of textural indices including fractal dimension, lacunarity, and spatial autocorrelation indices are truly spatial-based textural indices. There is an increasing interest in these spatial-based textural indices in recent literature (Dong, 2000; Myint et al., 2006). In this paper, effects of window sizes on classification accuracies were tested for three spatial-based textural indices: fractal dimension, lacunarity, and Moran's *I*. The optimal windows for different indices with different spectral-textural configurations were compared. The maximum likelihood classifiers was used to perform classification as it is one of the most commonly used and robust classifier and it is commonly used in previous window size effect studies (Chen et al., 2004; Myint and Lam, 2005a). In addition to classification accuracy, the association between window size and detailed level LULC object size (i.e. single houses etc.) will be also analyzed to generate rules of thumb for selecting proper windows.

4.2 Textural Indices

4.2.1 Fractal Dimension

Various methods exist for calculating the fractal dimension of a surface. As documented in recent benchmark tests (Lam et al., 2002; Zhou and Lam, 2005), a slightly modified version of the triangular prism (TP) method (Clarke, 1986; Zhao, 2001) was found to be effective than the box counting, Fourier spectrum, variogram, and probabilistic methods. In this method, TPs (Figure 4.1) are constructed by connecting the four corner pixels with the center pixel, with the z-position of the center point averaged from the corner pixel values. The edge length (in pixel) is

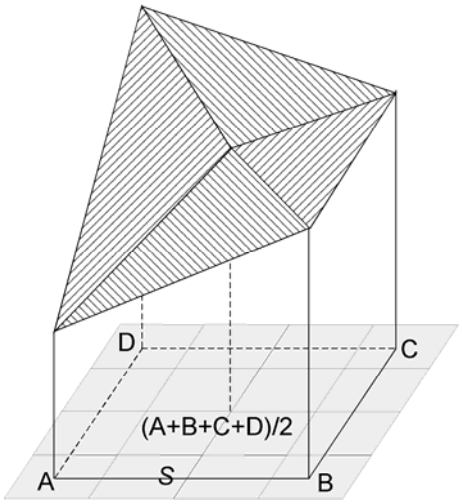

Figure 4.1 A triangular prism.

the step size *S*. By taking a number of measurements with a series of steps, a log-log regression between surface area and area of step size can be derived. The slope of the regression line is used to derive the fractal dimension using equation (1) (Clarke, 1986). However, it was found that the use of square step size in log-log regression underestimated the result and thus a modified log-log regression (equation 2) was provided (Lam et al., 2002; Zhao, 2001).

$$LogA=a+(2-D)LogS^2 \quad (1)$$

$$LogA=a+(2-D)LogS \quad (2)$$

where A is the total surface area of the TP surfaces, S is the step size, a is the intercept, D is fractal dimension.

When using the TP method to calculate the fractal dimension of a small neighborhood, especially when using the moving window technique to extract fractal feature of an image, proper selection of step size is important such that the constructed TPs take full coverage of the local window and truly reflect local characteristics. As the traditional geometric steps or arithmetic steps cannot guarantee a full coverage, divisors of window size (divisor steps) were used to construct series of steps in this research (See Chapter 3).

4.2.2 Lacunarity

Lacunarity, a counterpart of fractal dimension, was proposed to describe the different appearance of fractals with the same dimension. Lacunarity is defined as the degree that a fractal deviates from transitional invariance (Gefen et al., 1984; Mandelbrot, 1983). It describes the gap distribution inside a fractal. Hence, it is a quantitative measurement of heterogeneity. A fractal with higher lacunarity is more porous than those of lower lacunarity measurements. As heterogeneity is a scale-dependent phenomenon, the scale used has important effects on lacunarity measurements. Plotnick et al. (1996) extended the use of lacunarity on non-fractal real datasets. Lacunarity has been applied to a number of geospatial and environmental research problems (Greenhill et al., 2003; Henebry and Kux, 1995; Myint and Lam, 2005a).

Like fractal dimension, the algorithm of calculating lacunarity is not unique. There are several different estimators or definitions in the early literature (Gefen et al., 1984; Lin and Yang, 1986; Mandelbrot, 1983; Voss, 1986). Voss (1986) presented a probabilistic approach to estimate lacunarity of gray-scale images. Dong (2000) developed an approach based on the gliding-box algorithm (Allain and Cloitre, 1991) and the differential box counting method (Sarkar and Chaudhuri, 1992). Du and Yeo (2002) provided a novel modification to Dong's method by introducing the relative differential box counting method (Jin and Ong, 1995). In this window size effect study, we used a new estimator based on the gliding-box algorithm and the fractal triangular method (Clarke, 1986).

The gliding-box algorithm was proposed by Allain and Cloitre (1991). The algorithm was initially defined for binary data. Consider a one- or two-dimensional lattice containing a number of points; place a r (or r x r) box on the top left corner of the image and count the covered points as the box mass. The box then glides on the lattice by moving one unit right or down. Let $n(m,r)$

denote the number of gliding-boxes having a mass of *m*; *N* denotes the total number of gliding-boxes; let *Q(m,r)* to be the probability of a box with a mass m. Then

$$Q(m,r) = n(m,r) / N \tag{3}$$

The lacunarity at a given scale *r* can be defined (Voss, 1986):

$$\Lambda(r) = \frac{\sum_{m=1}^{n} m^2 Q(m,r)}{(\sum_{m=1}^{n} mQ(m,r))^2} - 1 \tag{4}$$

This is the mean-square deviation of the fluctuations of mass distribution probability divided by its square mean.

To estimate lacunarity, we constructed TPs similar to the original TP method. TPs are placed one column or row next to each other such that each TP corresponds to a gliding-box on the image surface. The image roughness inside of a gliding-box can be quantified by the ratio of the surface area of the TP to the area of basement gliding-box.

$$m(i,j) = ceil(A(i,j)/(r \times r)) \tag{5}$$

This measurement can be used as an alternative interpretation of box mass *m* in equation (4) for the calculation of lacunarity.

4.2.3 Moran's *I*

Spatial autocorrelation (Cliff and Ord, 1973; Goodchild, 1986) refers to the similarity or dissimilarity of values between neighboring pixels. Moran's *I*, a robust measure of spatial autocorrelation, has also been applied locally to generate additional textural layer to help classification (Emerson et al., 2005). These previous research demonstrates the potential of Moran's *I* as an aid in image classification. The formula of Moran's *I* is:

$$I(d) = (n\sum_{i}^{n}\sum_{j}^{n} w_{ij} z_i z_j) / (W\sum_{j}^{n} z_i^2) \quad (6)$$

where w_{ij} is the weight at distance d, w_{ij}=1 if point j is within a certain distance d of point i, otherwise w_{ij}=0; W is the summation of all weights for any $i \neq j$; z is the deviation from its mean value. I >0 indicates a positive autocorrelation, and I < 0 indicates a negative autocorrelation. When there is a random pattern, I will approach 0.

4.3 Study Area

An IKONOS image of Metairie, Louisiana, taken on September 2, 2005 after Hurricane Katrina, was used in this study (Figure 4.2). The study area covers around 4.8 x 3.6 square kilometers and is a highly populated area. Based on the USGS LULC classification scheme (Anderson et al., 1976) and previous research about the need for further detailed classification of residential area (Lo et al., 1997; Myint and Lam, 2005b), a classification scheme with commercial, residential I (single family), residential II (multiple family, usually with less than 50% vegetation coverage), and grassland was used in this research (Figure 4.3, Table 4.1).

The training area was selected carefully based on field survey and half-foot aerial photograph. These areas were distributed across the image to ensure representation. Descriptive statistics are listed in Table 4.2. The minimum and maximum values of different land-use/land-cover categories indicate the between-class overlap. The in-class heterogeneity is indicated by the coefficient of variation (CV), as both residential lands and commercial lands express a more than 10% relative standard deviation, a conventional cut-off line of using the traditional pixel-based maximum likelihood classifier (Myint et al., 2006).

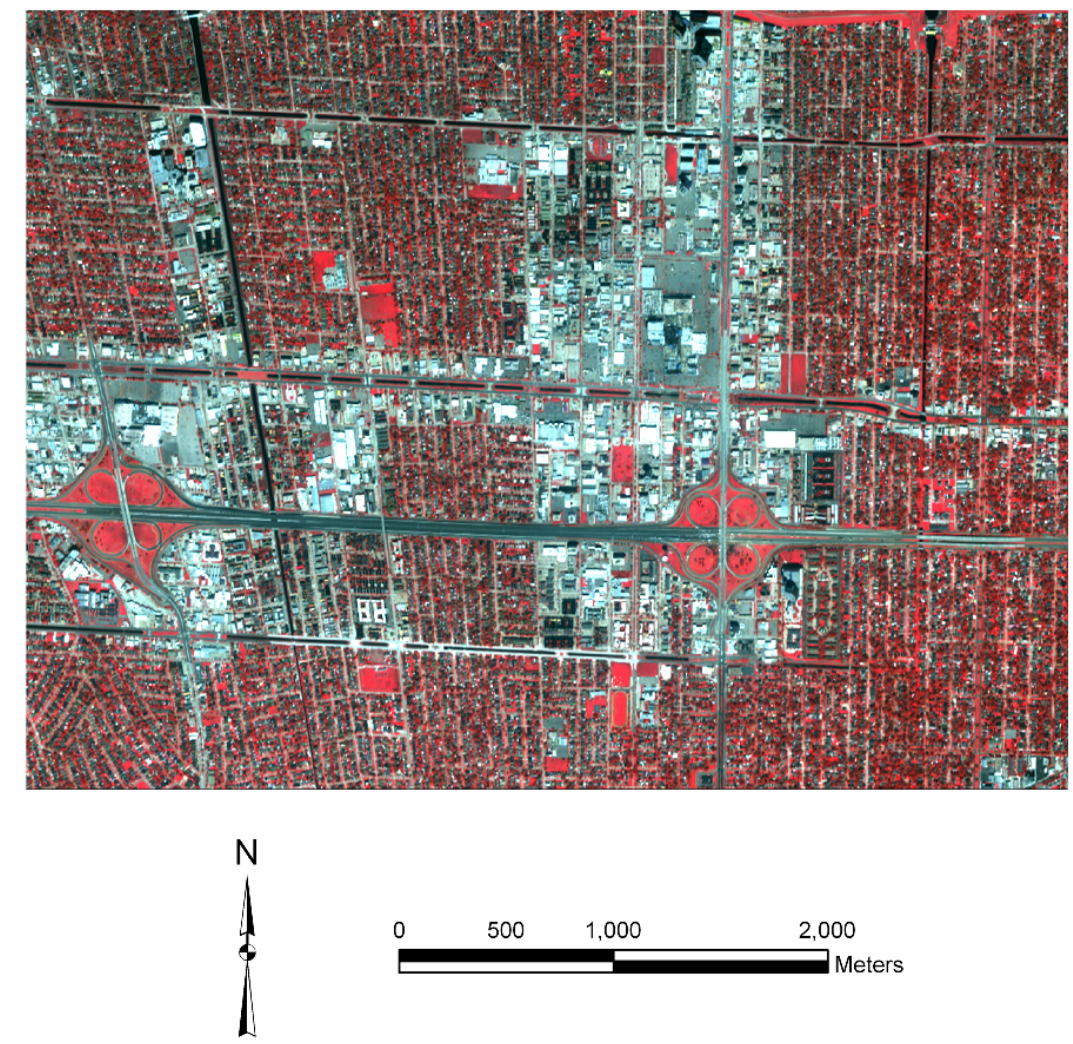

Figure 4.2 The study area: Metairie, Louisiana. The IKONOS image was taken on September 2, 2005. Shown in band 4, 3, 2 composition.

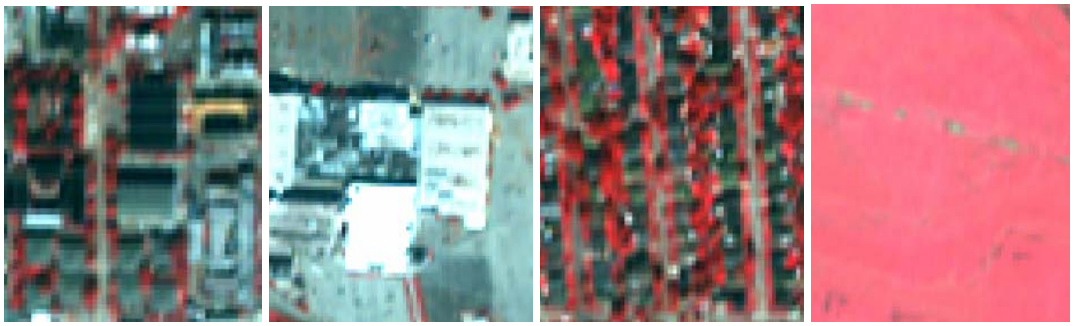

(a) (b) (c) (d)

Figure 4.3 A visual illustration of different land use categories. (a) residential 2; (b) commercial; (c) residential 1; (d) grassland.

Table 4.1 Land-use/land-cover classification scheme description

Category	Description
Commercial	Areas used predominantly for the sale of products and services, including shopping centers, office buildings, warehouses, driveways, parking lots etc.
Residential I	Areas used primarily for residential purposes, occupied by single-family houses where vegetation coverage is above 50%
Residential II	Areas used primarily for residential purposes, occupied by multi-family apartments/townhouses, or overcrowded residential area where vegetation coverage is above 50%
Grassland	Areas dominated by grasses like parks or big playgrounds, excluding those located inside of residential or commercial lots.

Table 4.2 Descriptive statistics of different bands

Band	Land Use	Min	Max	Mean	St. Dev.	CV
Green	Res1	334	1222	440.44	57.75	0.13
	Res2	347	1166	479.71	86.00	0.18
	Commercial	330	1639	596.46	150.50	0.25
	Grassland	394	554	440.59	14.11	0.03
Red	Res1	189	1168	317.82	71.33	0.22
	Res2	202	1064	364.44	105.57	0.29
	Commercial	181	1603	494.17	169.06	0.34
	Grassland	245	465	290.75	22.67	0.08
NIR	Res1	165	1151	450.61	117.08	0.26
	Res2	133	1136	395.70	118.64	0.30
	Commercial	123	1468	474.92	161.37	0.34
	Grassland	360	965	665.67	88.17	0.13

Figure 4.4 plots the average lacunarity values and fractal dimensions for each LULC category using the training samples. The measurement window is 33x33 pixels. Grassland has the lowest fractal dimension and the least complexity. The relative order of fractal dimension from high to low is residential type 1, residential type 2, commercial, and grassland. The relative order holds for all bands, including the first principal component. One may also observe that for the same land use type, the measured fractal dimension varies a bit when a different band is used, with the near-infrared band the highest followed by the red band and the green band. For lacunarity, the relative ranking order from low to high is also residential type 1, residential type 2,

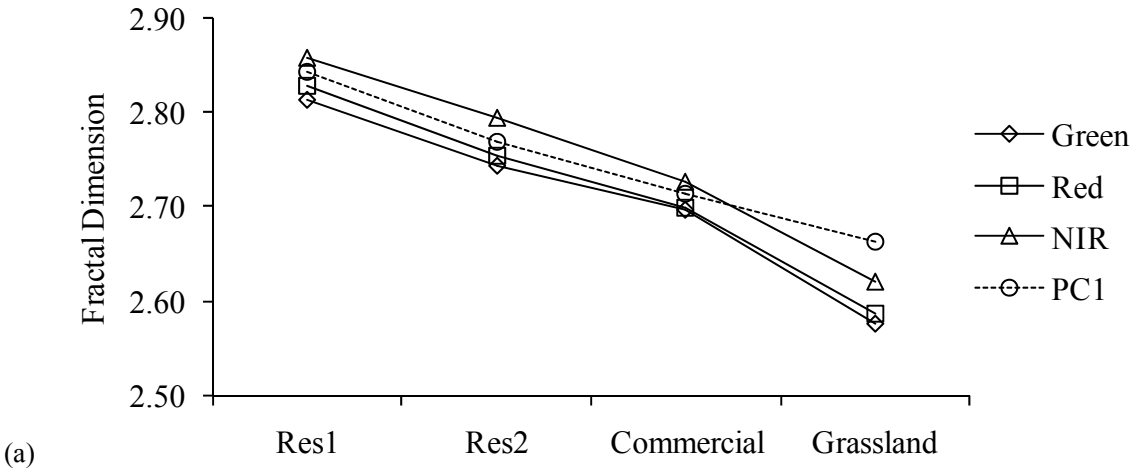

(a)

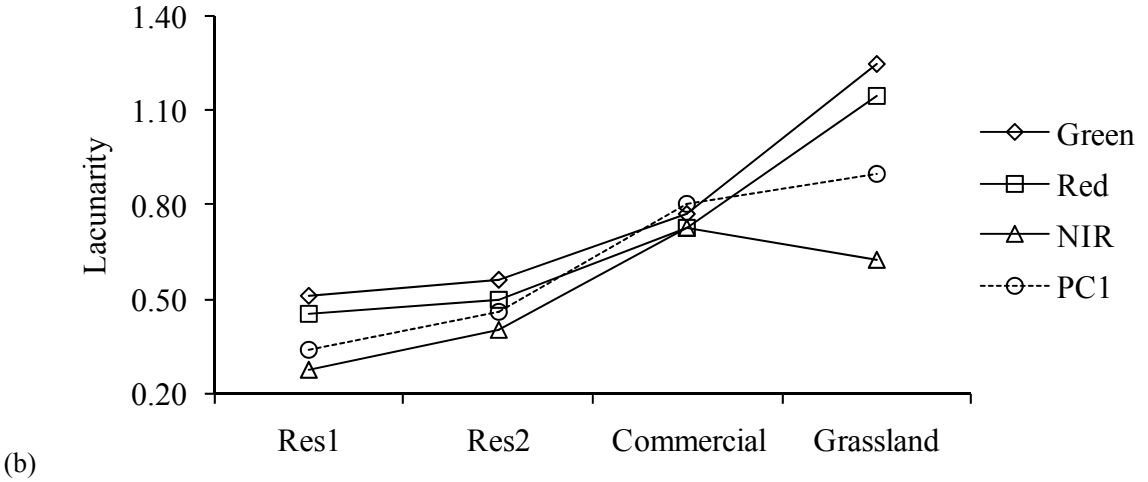

(b)

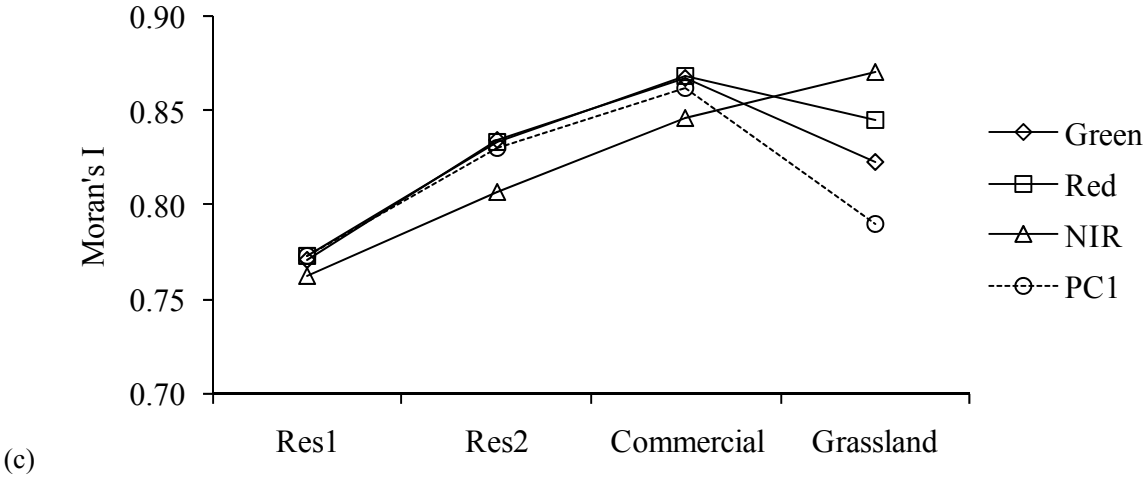

(c)

Figure 4.4 Average fractal dimension (a), lacunarity (b), and Moran's *I* (c) measurements of the four different land-use/land-cover categories from the green, red, near-infrared, and the principal component band of the training samples.

commercial, and grassland, with the exception of grassland measurement from the near-infrared band. With the exception of grassland, the lowest lacunarity value occurred in the near-infrared band, while the green band is higher than the red band. Thus fractal dimension and lacunarity exhibit a reverse ranking relationship among different land use categories and bands. For spatial autocorrelation measurement (with Moran's *I*), considering only direct neighborhoods with shared edges for the weighting scheme and using the 33x33 window on average, all land use categories exhibit positive autocorrelation, with a high-low order of commercial, residential type 2 and residential type 1. This trend implies that commercial land is the least varying; followed by residential type 2 and residential type 1, which can be supported by the sub-content size (building size, parking lot size, amenity grass size, etc.). Grassland, however, varies across bands. Although grassland has the least standard deviation (Table 4.2), it does not always have the smallest Moran's *I* (Figure 4.4). Standard deviation does not correlate to Moran's *I* measurement.

4.4 Classification Results and Analysis

Classifications were performed with different spectral-textural band configurations. The purpose is to test how additional textural information can help improve classification accuracy, and how window size affects the performance of textural indices. Previous research used multiple textural bands from corresponding multispectral bands (Emerson et al., 2005; Myint et al., 2006), or single textural band in addition to multiple spectral bands (Myint et al., 2006), or only textural bands (Myint and Lam 2005b). In addition to these different spectral-textural band configurations, the composite texture vector containing different textural indices (fractal dimension, lacunarity, Moran's *I*) was also explored in this research (Table 4.3).

Table 4.3. Description of designed experiments

Band configurations	Experiments
Three spectral bands (green, red, NIR) and their corresponding textural bands	Exp1. 3 spectral + 3 Fractal bands Exp2. 3 spectral + 3 Lacunarity bands Exp3. 3 spectral + 3 Moran's *I* bands Exp4. 3 spectral + 3 Texture vector
Three spectral bands (green, red, NIR) and additional textural band(s) extracted from the first principal component band	Exp5. 3 spectral + 1 Fractal band Exp6. 3 spectral + 1 Lacunarity band Exp7. 3 spectral + 1 Moran's *I* band Exp8. 3 spectral + 1 Texture vector
Textural bands extracted from the three spectral bands (green, red, NIR). Spectral bands not included.	Exp9. 3 Fractal bands Exp10. 3 Lacunarity bands Exp11. 3 Moran's *I* bands Exp12. 3 Texture vector

* Each texture vector consists of three textural bands (fractal, lacunarity, and Moran's *I*), corresponding to the same spectral layer.

In addition, per-pixel classification with only three spectral bands was performed as a baseline for comparison. The difference among these experiments is the different emphasis of the textural and spectral information.

To examine the effects of moving window size on classification accuracy, a series of moving windows 9x9, 13x13, 17x17, 21x21, 25x25, 29x29, 33x33, 37x37, and 41x41, were used to extract fractal dimension, lacunarity, and spatial autocorrelation (Moran's *I*) feature layers.

Training sites were carefully selected by referencing aerial photographs and field survey. As two neighboring moving windows share a high-percentage of common pixels, neighboring local textural measurements correlate with each other. A random sampling process was implemented on the training sites to reduce this biased correlation among adjacent windows, so the final training set will be more representative. The final training set includes 6400 samples. The accuracy assessment procedure involves an on-screen check with the aid of half-foot resolution aerial photograph and field survey. As the area is quite big and heterogeneous, a stratified random sample based on land use categories was used. The test set contains 5370 points. To obtain a stable measurement, the classification process was repeated three times using three different training sets for each experiment. The mean measurement is used for the following accuracy comparison to address window size effects. Overall results are shown in Table 4.4.

4.4.1 Three Spectral Bands (Green, Red, NIR) and Their Corresponding Textural Bands

In experiment 1-4, each original spectral band was augmented equally with their textural bands. For the first three experiments (Exp1-3) with individual textural index, classifications were based on six spectral-textural bands. For the fourth experiment (Exp4) with texture vector, classifications were based on 12 spectral-textural layers. Results are shown in Figure 4.5. Compared to the baseline overall accuracy of traditional spectral-based classification (52.8%), supplying fractal dimension, lacunarity, or spatial autocorrelation (Moran's *I*) definitely benefitted the classification, as shown in Figure 4.5. As expected, highest accuracy was yielded using a texture vector. The improvement using a texture vector is significant at the 0.05 significance level (Z=1.96), reflected by Kappa statistics (Table 4.5). For single textural measure, lacunarity was the most accurate, followed by Moran's *I* and fractal.

Table 4.4 Average overall accuracy of different experiments at different windows

Window	Exp1	Exp2	Exp3	Exp4	Exp5	Exp6	Exp7	Exp8	Exp9	Exp10	Exp11	Exp12
7	58.5	61.0	57.5	64.9	55.5	59.1	54.1	60.0	44.4	53.8	39.9	56.2
9	58.4	61.4	58.5	65.7	55.5	59.1	55.2	60.0	47.4	56.2	39.3	58.3
11	58.4	62.8	59.2	65.7	55.7	59.5	55.7	60.2	46.7	57.7	42.6	58.8
13	59.1	64.4	59.6	67.1	55.9	59.8	56.0	60.8	48.4	59.2	45.1	60.9
15	59.2	64.8	60.0	68.5	56.5	60.1	56.4	61.6	50.9	60.0	47.1	62.9
17	59.7	65.9	60.8	69.5	56.3	60.4	56.9	62.4	50.4	61.3	47.9	64.1
19	59.8	66.7	61.6	70.2	56.9	60.9	57.9	63.3	49.8	62.1	50.2	64.8
21	60.4	67.3	63.0	70.7	56.5	61.7	58.7	64.1	51.2	63.1	52.4	66.3
23	59.9	68.0	63.0	71.7	56.4	62.9	59.1	65.4	51.1	63.6	55.6	67.5
25	60.3	69.1	63.2	71.6	57.4	63.5	59.8	65.7	51.0	64.3	56.7	67.4
27	60.4	69.3	64.2	71.5	56.7	64.0	60.0	65.8	49.3	64.5	57.8	67.4
29	60.7	69.8	64.7	71.4	56.2	64.3	59.9	65.8	49.3	65.5	58.7	67.9
31	60.7	69.7	65.7	71.5	56.1	64.8	60.2	66.1	50.8	66.1	59.3	68.2
33	60.2	69.5	65.9	70.9	55.9	64.8	60.8	66.1	49.1	66.1	59.7	68.0
35	59.9	69.8	66.1	70.9	56.0	65.2	61.3	66.6	49.8	66.7	59.5	67.4
37	60.1	69.5	66.1	70.7	56.7	65.3	61.5	66.7	50.5	66.6	58.9	68.1
39	59.5	69.3	66.2	70.3	55.8	65.2	61.7	66.9	47.9	66.2	59.3	67.5
41	59.3	69.0	66.1	70.2	55.5	65.0	61.5	66.4	49.0	65.7	59.3	67.1

* The overall accuracy of spectral-based classification is 52.8%.

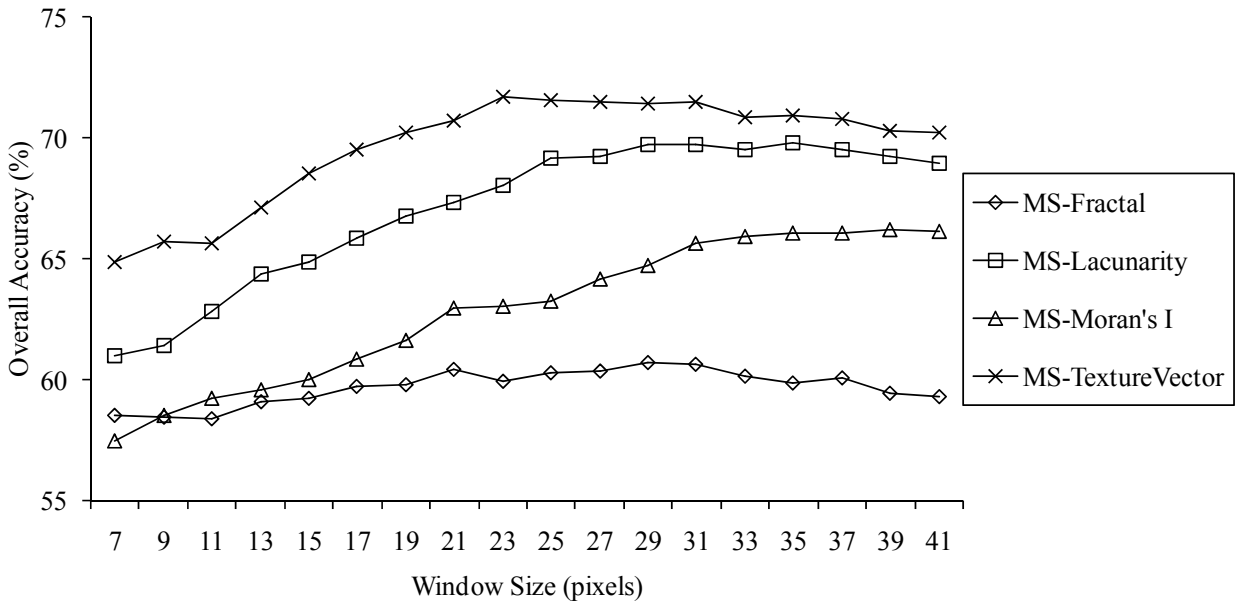

Figure 4.5 Overall accuracies across different windows for different experiments with integrated spectral-textural bands. Textural bands were derived from the green, red, and near-infrared multi-spectral IKONOS bands.

Table 4.5 Kappa Z statistics of texture vector-aided approach over individual textural index-aided approach (exp 4 versus exp 1-3)

W	TV* VS Fractal	TV VS Moran's *I*	TV VS Lacunarity	TV VS Spectral
7	4.77	6.30	4.09	8.98
9	5.70	6.02	4.50	9.74
11	6.22	5.86	3.20	10.16
13	6.43	6.32	2.87	11.29
15	8.12	8.29	4.03	13.00
17	9.02	8.20	4.65	14.41
19	10.38	8.29	4.86	15.60
21	10.71	7.61	4.75	16.38
23	12.04	8.67	4.75	17.37
25	12.25	8.44	3.54	17.52
27	11.60	7.71	3.56	17.50
29	11.56	7.24	2.70	17.60
31	12.24	6.26	3.08	17.75
33	12.37	5.42	2.57	17.39
35	12.21	5.09	2.13	17.31
37	11.92	5.05	1.88	17.16
39	11.84	4.67	1.75	16.65
41	12.17	4.13	1.66	16.46

*TV: texture vector.

For the experiment of fractal dimension (three spectral bands and their corresponding fractal layers), the accuracy curve is quite stable with minor fluctuations among window size. The highest accuracy (60.7%) was yielded at window 29x29 (pixels) and accuracies were quite stable from window 17x17 to 37x37 with less than 1% down from the peak point. For all tested windows, the biggest difference was only 2.3%, implying that fractal dimension was less sensitive to window size. In contrast, both lacunarity and Moran's *I* were more sensitive to window size, with 8.8% max-min difference for lacunarity and 8.7% max-min difference for Moran' *I*. For lacunarity-aided classification, the overall accuracy started from a low point at the smallest window 7x7 and gradually increased to a stable level. The highest accuracy (69.8%) was yielded at window 29x29 and 35x35, followed by a slight downward curve. For Moran's *I* spatial autocorrelation index, the overall accuracy started from a low point at window 7x7 and gradually increased to a stable level. The highest accuracy (66.2%) was achieved at window 39x39. Furthermore, stable stages existed for both lacunarity and Moran's *I*, from window 25x25 to 41x41 for lacunarity and from window 31x31 to 41x41 for Moran's *I*. Within the window span of the stable stage, the accuracy variation is within 1% of the peak point. For the texture vector-aided approach with overwhelming textural information, a clear increasing-plateau-decreasing trend was observed. From the lowest point at window 7x7, the overall accuracy gradually increased to the peak point (71.7%) at window 23x23, followed by a slight decreasing trend. The stable stage spanned from window 21x21 to 37x37, where overall accuracies were within 1% difference threshold from the peak point at window 23x23.

4.4.2 Three Spectral Bands (Green, Red, NIR) and Additional Textural Band(s) Extracted from the First Principal Component Band

In experiment 5-8, the original three spectral bands were first subjected to principal component analysis. The first principal component accounted for 77.7% of total information and

was used to extract textural layers. For the first three experiments (Exp5-7) with individual textural index, classifications were based on four spectral-textural bands. For the fourth experiment (Exp8) with texture vector, classifications were based on six spectral-textural layers. Results were shown in Figure 4.6. Improvements over the baseline overall accuracy of traditional spectral-based classification (52.8%) can be observed. Comparing to experiment 1-4, each experiment here was based on the same spectral bands but with fewer textural bands. Thus, for each corresponding experiment with the same textural index(es), the overall accuracy was slightly lower, at roughly 3-7%. Texture vector-aided approach provided significant improvement to individual textural index-aided approach at the 0.05 significant level (Z=1.96), as reflected by the Kappa Z statistics (Table 4.6).

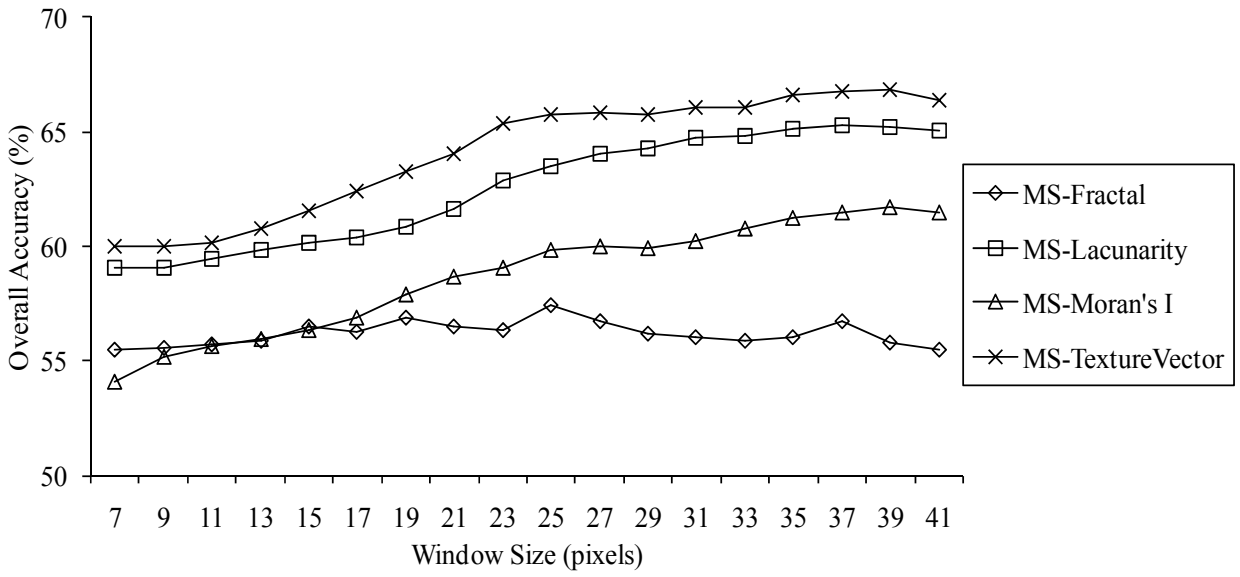

Figure 4.6 Overall accuracies across different windows for different experiments with integrated spectral-textural bands. Textural layers were derived from the principal component of multi-spectral IKONOS bands.

Table 4.6 Kappa Z statistics of texture vector-aided approach over individual textural index-aided approach (exp 8 versus exp 5-7)

W	TV* VS Fractal	TV VS Moran's *I*	TV VS Lacunarity	TV VS Spectral
7	2.64	3.75	0.82	4.40
9	3.12	3.25	1.39	4.82
11	2.85	3.04	0.70	4.87
13	3.37	3.67	1.06	5.52
15	3.41	3.86	1.38	6.22
17	4.64	4.34	1.92	7.10
19	4.92	3.48	2.19	7.65
21	6.25	3.89	2.70	8.74
23	7.83	5.15	3.13	10.27
25	8.00	5.03	3.35	10.93
27	8.56	4.91	2.80	11.17
29	9.17	5.15	2.16	10.95
31	9.98	5.45	2.32	11.55
33	10.00	4.75	2.28	11.62
35	10.67	4.72	2.58	12.35
37	10.41	5.05	2.57	12.52
39	11.38	4.89	2.84	12.81
41	11.48	4.42	2.44	12.33

*TV: texture vector.

For these experiments with texture information derived from the principal component band, window size effects on classification accuracy were slightly different, but the entire trend remained. Fractal dimension was also insensitive to window size compared to the other two indices but carried frequent fluctuations across windows. The maximum-minimum difference for fractal dimension was 2.0%, with the peak point occurring at window 25x25 (57.4%). The stable stage was spanned from window 15x15 to window 27x27, with an additional window 37x37. Both lacunarity and spatial autocorrelation aided approaches exhibited similar window effects as previous experiments (1-4) using textural layers derived from the original multispectral bands, with a clear gradual increasing trend from a low point at window 7x7 to a stable stage, but the subsequent decreasing trend was not obvious. The peak point for lacunarity (65.3%) was at window 37x37 and the stable stage spanned from 29x29 to 41x41. Both the peak point and the range of stable stage were postponed compared to previous experiments (1-4) using textural layers derived from the original multispectral bands. The peak point for Moran's *I* (61.7%) was at window 39x39 and the stable stage spanned from 33x33 to 41x41. The stable stage was also delayed to a larger window (33x33) compared to the 29x29 of experiments that use textural layers from the original multispectral bands. A texture vector-aided approach combined these effects and resulted in a delayed peak point and stable stage. The peak point (66.9) was at window 39x39 and the stable stage extended from 29x29 to 41x41.

4.4.3 Textural Bands Extracted from the Three Spectral Bands (Green, Red, NIR). Spectral Bands not Included

In experiment 9-12, each original three spectral bands were used to extract textural layers. Only textural layers were used for classification. For the first three experiments (Exp9-11) with individual textural index, classifications were based on three textural layers. For the fourth experiment (Exp12) with texture vector, classifications were based on nine textural bands.

Results are shown in Figure 4.7. Compared to experiment 1-4, for each corresponding experiment with the same textural index(es), the overall accuracy was lower, with roughly 2-10%. However, pure texture-based classification did not always outperform spectral-based classification (52.8%), except lacunarity and the texture vector methods, as revealed in Figure 4.7. In some cases (w=7, 9, 11), pure textural-based approach was significantly less accurate or no significant difference than spectral approach at the 0.05 significance level (Table 4.7). However, texture vector-based approach still significantly outperformed individual textural index-based approach at the 0.05 significance level (Z=1.96), reflected by Kappa Z statistics (Table 4.7). This further shows the need to integrate spectral and textural information. This series of experiments (9-12) also serve as a pure window-effect study purpose since only textural information was used.

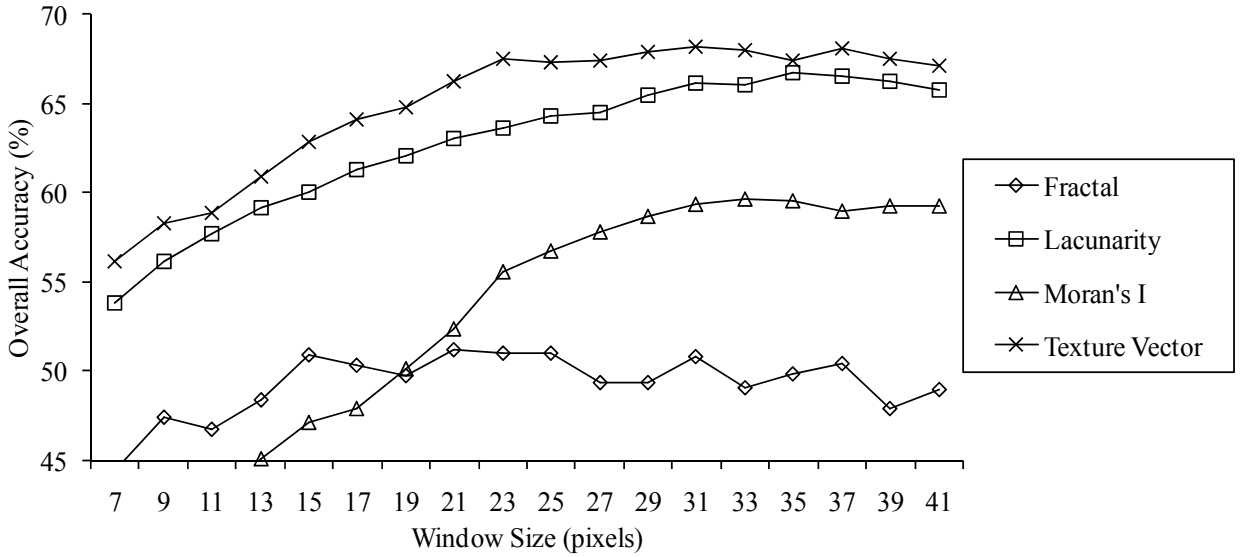

Figure 4.7 Overall accuracies across different windows for different experiments with only textural bands. Textural bands were derived from the green, red, and near-infrared multi-spectral IKONOS bands.

Table 4.7 Kappa Z statistics of texture vector-aided approach over individual textural index-based approach (exp 12 versus exp 9-11)

W	TV* VS Fractal	TV VS Moran's *I*	TV VS Lacunarity	TV VS Spectral
7	9.90	11.77	11.82	-2.81
9	10.13	14.11	11.66	-0.48
11	11.62	14.30	7.97	0.82
13	13.93	15.02	7.00	3.07
15	14.03	15.65	7.43	5.92
17	16.11	16.41	6.49	7.62
19	18.62	15.36	6.37	8.91
21	18.52	14.95	6.53	10.86
23	20.32	13.44	6.91	12.38
25	20.69	12.10	5.60	12.15
27	21.86	11.06	5.71	12.57
29	21.46	10.52	4.72	13.27
31	23.04	10.55	4.60	14.19
33	25.23	10.09	4.34	14.18
35	22.80	9.51	2.70	13.43
37	23.40	10.78	3.21	14.24
39	24.17	9.90	2.94	13.69
41	22.84	9.19	2.90	13.27

*TV: texture vector.

This group of experiments with pure textural information exhibited a similar trend as previous experiments (1-8). Classification accuracy using fractal dimension layers did not show an increasing-decreasing trend similar to that of lacunarity and Moran's *I*, with a maximum-minimum difference of 6.8%, but bigger fluctuations across windows. The peak point was at window 21x21 and a stable stage was a short range from 21x21 to 25x25, while three additional windows (15x15, 31x31, 37x37) also yielded accuracies within 1% of the peak point. Both lacunarity and Moran's I exhibited an increasing trend to a stable stage, followed by a slight downward curve. The peak point occurred at window 35x35 for lacunarity (66.7%) with the stable stage ranging from 31x31 to 39x39. For spatial autocorrelation, the highest accuracy (59.7%) was achieved at window 33x33 with a stable stage spanning from 29x29 to 41x41. A clear upward-downward stage was observed for the texture vector approach, with a peak point (68.2%) at window 31x31 and the stable stage from 23x23 to 39x39.

4.5 Discussion: An Object-Based Analysis of Window Size Effects

The above experiments demonstrated clear window size effects on the texture-aided classification approach. Since window size is closely associated with the underlying contents covered by the window, a further analysis of the underlying contents, i.e., objects such as houses, amenity grasses, parking lots, and community roads, may provide valuable information to explain window size effects and suggest some guidelines.

4.5.1 Object-Based Classification

The object-based approach draws increasing interest in the remote sensing community with a wide range of applications. Different from the texture-aided classification, the object-based approach takes a two-stage approach. The first stage is to segment the image into distinct objects according to a set of criteria such as color, shape, texture, etc. General segmentation techniques

include region-based and boundary-based approaches (Cufi et al., 2002; Haralick and Shapiro, 1985; Pal and Pal, 1993). Each object was considered to be homogeneous according to a preset threshold value. It could involve top-down image segmentation or bottom-up pixel aggregation, or both processes. A hierarchical series of objects that consist of parent-children object relationship can also be constructed given a series of homogeneous criteria. The second stage is to use some standard classifiers to classify these objects, instead of pixels, into different categories. Parameters, or features, that associated with the objects, such as mean value, standard deviation, entropy, etc., are used. Supervised class signature training is often involved in the second stage.

The object-based approach has been studied for quite some time (e.g. Ketting and Landgrebe, 1976). However, it is just recently getting popular in image processing community because of increased computing power and availability of well-developed commercial software, such as Definiens (formerly known as eCognition) and Feature Analyst (extensions for ArcGIS, Imagine, and Geomedia). In this research, Definiens was used because of its great flexibility of user control and independence of third party software.

Definiens (2008) implements an excellent multiresolution segmentation algorithm, allowing user to control the weight of two complementary homogeneity criteria: color and shape. The color criterion controls the standard deviations of pixel values within an object. The shape criterion is comprised of two sub-criteria: a smoothness criterion that controls the smoothness of image borders, and a compactness criterion that controls the deviation from the ideal compact form. The threshold homogeneity is controlled by the user through a scale parameter. The scale parameter, as used by Definiens (2008), is an abstract term that controls the maximum allowed heterogeneity; it has no units. When a larger scale is used, larger segmented objects will result

from the same study area. By changing this scale parameter, a series of objects with hierarchical structure can be defined, forming multi-resolution objects segmentation. The appropriate scale parameter depends on the satisfied segmentation level, and is often decided through a trial-and-error approach (Chubey et al., 2006).

In Definiens (2008), a set of indices are measured for the objects, such as statistical indices (maximum, minimum, mean, standard deviation, etc.), shape indices (area, main direction, length/width, compactness, rectangular fit, roundness, density, etc.), and textural indices (e.g. mean, standard deviation, entropy from the Gray Level Co-occurrence Matrix (Haralick et al., 1973). Neighborhood relationships to topological neighbors and parent-children parameters are also included and can be customized. By examining these indices and parameters, users can simply collect training samples and define signatures used for classification, and then apply the nearest neighborhood classifier to classify objects. One can also further define rule set and membership functions to use the fuzzy classifiers. If a hierarchical object structure is used, hierarchical classification results can also be yielded. A number of successful applications using Definiens have been made in recent literature (Chubey et al., 2006; Mitri and Gitas, 2004; Yu et al., 2006).

To address the window size effects on LULC classification, Definiens was used to segment the study area into underlying objects of these categories. The segmentation scheme is set for single-family houses, amenity grasses (yards), amenity trees, community roads, multi-family houses, commercial buildings, parking lots, and grasslands (parks). The panchromatic band is combined with the green, red, and near-infrared band of the IKONOS image into segmentation, as the panchromatic band improved segmentation in some previous experiments (Chubey et al., 2006). Due to its higher spatial resolution, the panchromatic band was set with a weight of 3.0,

which equaled to the summation of three same-weighted 4-m multispectral bands. Multi-family houses and commercial buildings are generally larger than single-family houses, so two scales were used after a trial-and-error process. The first scale was set to 35 for single-family houses, amenity grasses (yards), amenity trees, and community roads. The second scale was set to 80 for multi-family houses, commercial buildings, parking lots, and grasslands (parks). A segmentation comparison at two scales is provided in Figure 4.8.

A trial-and-error approach was also used to select appropriate weight of the color criterion, compactness criterion, and smoothness criterion. Color criterion was set to 0.7 and shape criterion was therefore 0.3. The smoothness and compactness criteria were set equal to each other. A nearest neighbor classification was applied to selected training objects. With visual accuracy check, a trial-and-error approach was used to select the following criteria for classification: mean spectral values (four bands), standard deviations (four bands), compactness, and GLCM (Gray Level Co-occurrence Matrix) entropy. Obvious classification errors were further recoded. With 1240 random points from stratified sampling, the overall accuracy is 84.7%.

4.5.2 Comparative Study of Window Size Effects and Land Use Categories

The window size used to derive neighborhood texture measurements affects classification accuracies, as demonstrated previously. The effects generally include three aspects: stability of measurements, generalization effects, and edge effects. The stability of measurement is tied to the algorithm requirement of a textural index, while the generalization and edge effects could be associated with the individual image.

(a)

(b)

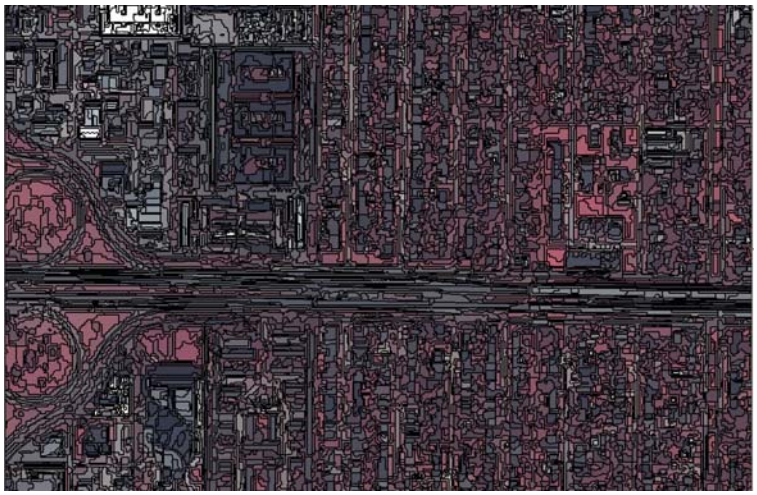

(c)

Figure 4.8 Segmentation results at different scales. (a) Original IKONOS image, shown in band 432 false color composite; (b) Segmented objects at scale 35; (c) Segmented objects at scale 80.

(1) Stability of measurements

Measurements such as fractal dimension require a window large enough to have sufficient measurements for a stable regression curve. Thus, small windows such as 3x3, 5x5, 7x7 are not likely to be good, as they affect the stability of measurements. Also due to the coverage problem or sampling methods in estimation algorithm, fractal dimension measurements could fluctuate around the theoretical curve given different windows. This fluctuation is larger at small windows like 7x7 and 9x9. Lacunarity relies on the statistics of gliding boxes, and a larger window help to retrieve sufficient samples for a reliable measurement. Spatial autocorrelation measurements would also benefit from larger windows. The problem of using small windows (7x7 and 9x9) was reflected in Figure 4.5-4.7.

(2) Generalization effects

Considering a uni-class area (such as residential area, or commercial area), bigger windows have bigger generalization power to reflect the unique texture of this class, while smaller windows could eventually derive some textures that are similar to another class. Considering generalization, a window should be large enough to cover distinct underlying objects (houses, parking lots), as well as different objects.

(3) Edge effects

On the edge of multi-class overlapped area, a texture measurement from a window is not tied to any class. With bigger windows, more boundary pixels will be involved in local neighborhood measurements. Although the proportion of the second class could be smaller, more windows will include two classes and there is greater potential for a window to cover more than two classes. This will blur the class boundaries and reduce classification accuracy at the boundaries.

Based on the object-based image segmentation, sizes of different buildings in the study area are listed in Table 4.8. Common sense of choosing window size is that it should cover these key objects as well as some adjacent elements (grasses, roads, parking lots, etc.). It is clear that the desired windows with stable accuracies (minimum 15x15 pixels, equivalent of 3600 square meters) are well beyond the area range of the three key building objects.

Table 4.8 Size of different buildings in the study area (square meters)

Objects	Scale	Min	Max	Mean	Median
Single-family houses	35	64	741	279	254
Commercial buildings	80	384	2736	1247	1152
Multi-family houses	80	162	2869	890	694

However, an important question regarding the generalization effect arises: which size would be sufficient to generalize the texture? To address this question, local statistics with moving window was applied to classified objects at each tested window in previous classification experiments. Five single-family residential neighborhoods and three commercial neighborhoods were selected in this study. Buildings dominated both residential area and commercial area with 25% and 56% respectively. However, the percentage of different objects varied from window to window, as plotted in Figure 4.9.

For residential neighborhoods, for the percentage of any object (houses, roads, trees, grass), the variation across different local windows will decrease as the window size increase. The standard deviation was used as a measurement to reflect the variation of objects composition among different windows. It is expected that with a smaller standard deviation, the objects composition are similar among different windows of the same land use category, hence textural

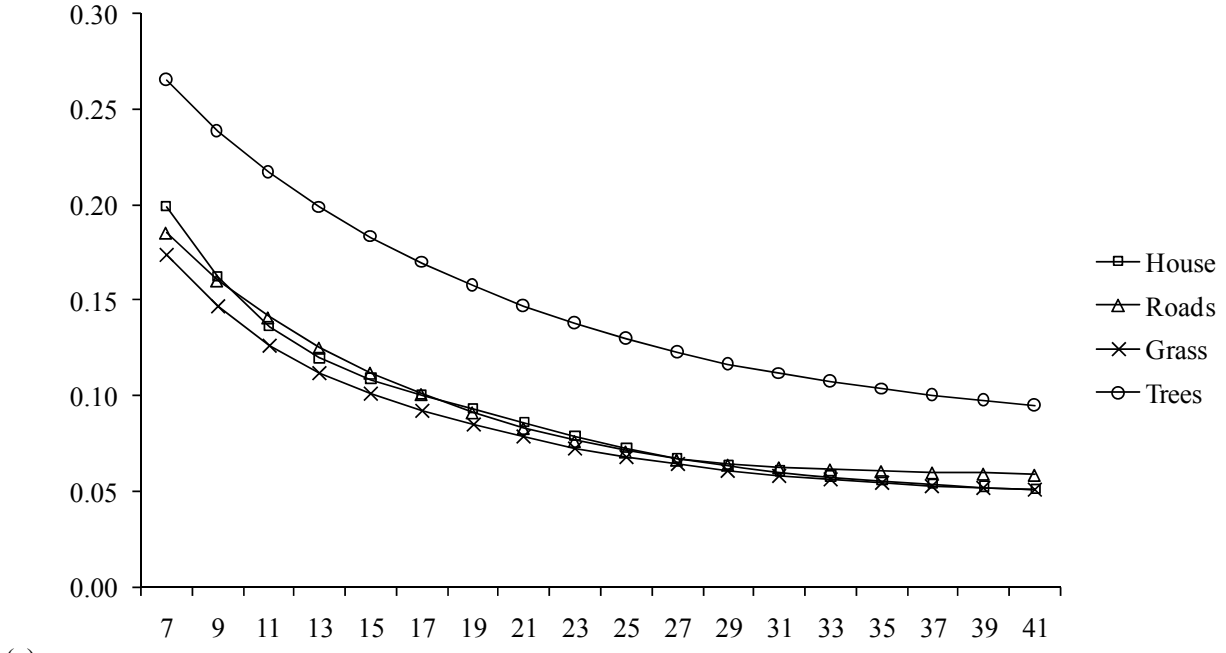

(a)

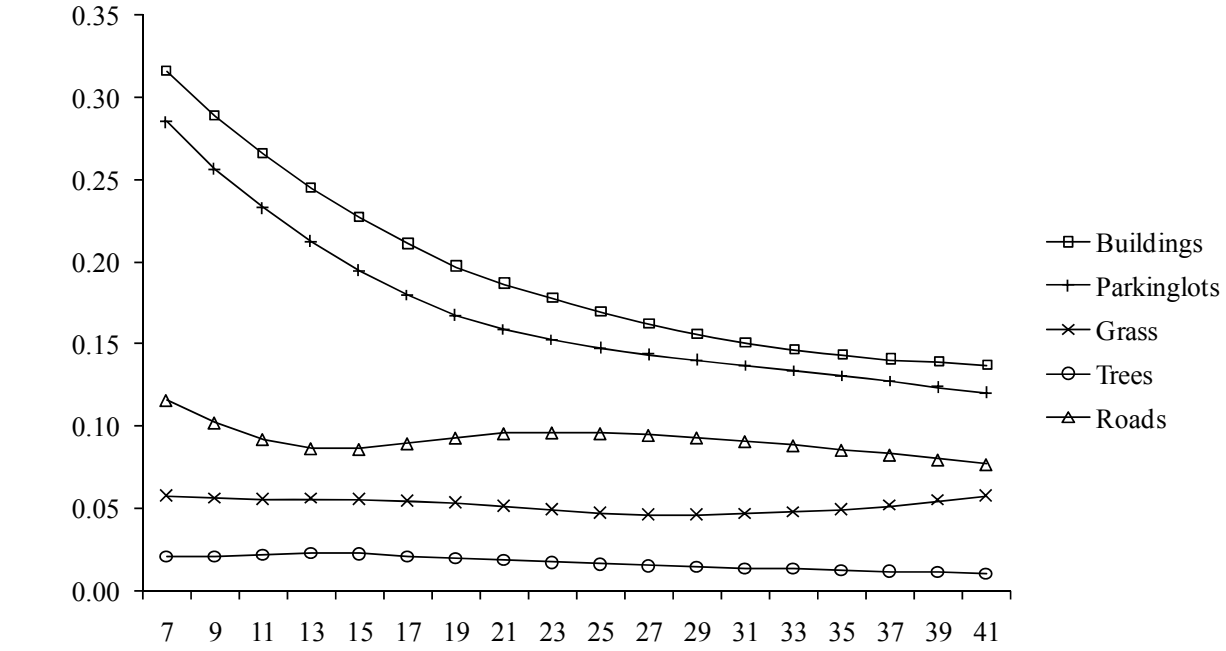

(b)

Figure 4.9 Standard deviation of the percentage of image object classes at different windows. (a) residential neighborhood; (b) commercial neighborhood.

measures based on this window size will be more stable. The gradient is in a descending trend. For houses, roads, grass and trees, the standard deviation decreased by half at window 17x17, 19x19, 19x19 and 23x23, compared to the initial stage at window 7x7. The difference of standard deviations between these windows and the biggest window 41x41 was just 0.05.

Similar trends can be found for two dominating elements of commercial area: buildings and parking lots, with standard deviations decreasing from the highest point (window 7x7) by half at window 27x27. The difference of standard deviations between window 27x27 and window 41x41 was just 0.03. For the 0.05 standard deviation threshold, window size can be further traced back to 21x21 for buildings and 19x19 for parking lots. Closely associated to these stable stages of generalization effects are the stable plateau of overall classification accuracies. At these windows, stable measurements were satisfied from both the algorithm perspective and generalization effects, and the measurements more accurately reflect local texture as the member of certain classes. Similar classes will be better characterized. However, although the generalization (small standard deviation) still increases after entering this stable stage, the increased edge effects will increasingly cut off the accuracies along the edges and even affect training samples that are near the class boundaries. The result is a trade-off between these two reverse effects, resulting in the classification curve as a stable stage and preceded by a steadily increasing trend and followed by a slight decreasing trend.

Based on this comparative study, optimal windows should be: (1) large enough to satisfy algorithm requirements for accurate and robust measurement; (2) large enough to cover underlying objects; (3) large enough to have good generalization such that variation of percentage of objects in each moving window is relatively small; (4) small enough to reduce edge effects at multi-class boundaries.

4.5.3 Limitations and Future Research

In above analysis, the rule of object-based approach is to generate descriptive statistics of the LULC objects (houses, roads, etc.). However, there are some limitations. First, the size of the segmented objects is subject to scale (an abstract term used by Definiens); an actual ground object can possibly be segmented into several parts. Second, the accuracy of object segmentation and classification can potentially affect the analysis of window size effects. Due to these limitations, future study could investigate the association between object size and window size effects with artificially generated data. In addition, texture indices such as fractal dimension, lacunarity, Moran's *I* have great potential to be integrated into object-based classification.

4.6 Conclusions

Window size plays an important role in texture-aided classification because of the use of moving window technique. This research investigated the optimal windows of three textural indices: fractal dimension, lacunarity, and Moran's *I*. A case study was carried out with an IKONOS image of an urban area in the greater New Orleans, Louisiana. Twelve experiments were carried out with different spectral-textural layer settings: three multispectral bands (green, red, near-infrared) and their corresponding textural layers (fractal dimension, lacunarity, Moran's *I*); three spectral bands and textural layers extracted from the principal component band; and only textural layers extracted from the three original multispectral bands. A total of 18 windows ranged from 7x7 to 41x41 were tested.

Although having the lowest overall classification accuracy, fractal dimension exhibited more stable classification results that were less sensitive to window size, while both lacunarity and Moran's *I* and the composite texture vector exhibited an increasing phase toward a stable stage and followed by a slightly decreasing phase thereafter. The texture-based approaches

without combination with spectral bands were discouraged based on the experimental results. Based on the overlapped results from two different groups of spectral-textural band combinations, the follow windows are recommended for spectral-textural classifications: 17x17 to 27x27 for fractal dimension, 29x29 to 41x41 for lacunarity, 33x33 to 41x41 for Moran's *I*, and 27x27 to 37x37 for the texture vector-aided approach. The range of recommended window size generally agrees with some previous research for lacunarity (Myint and Lam, 2005a; Myint and Lam, 2005b; Myint et al., 2006); but this research further revealed an increasing trend toward a stable stage. In addition, this research also brought new knowledge of window size effects on fractal and Moran's *I* with high-resolution satellite imagery.

Optimal window size should meet the following criteria: (1) large enough to satisfy algorithm requirements for accurate and robust measurement; (2) large enough to cover underlying objects; (3) large enough to have good generalization such that variation of percentage of objects in each moving window is relatively small; (4) small enough to reduce edge effects at multi-class boundaries.

Chapter 5
A Genetic Bayesian Approach for Texture-Aided Urban Land-Use/Land-Cover Classification

5.1 Introduction

Detailed urban land-use/land-cover (LULC) classification from high-resolution satellite imagery is increasingly needed to support a variety of applications such as population estimation, mass evacuation planning, and flood and damage estimation (Al-Khudhairy et al., 2005). However, accurate and fast classification of urban LULC remains a very difficult task due to the heterogeneous nature of urban environment. Traditional spectral-based classifiers are known to yield low classification accuracy for urban environment. Hence, new classification methods aiming at improving classification accuracy continue to appear (Myint and Lam, 2005a; Pal and Mather, 2005).

One approach to improving classification accuracy is to utilize textural information computed from the image to aid classification. There is substantial progress of applying textural indices in urban mapping, with a number of new indices recently introduced, such as fractal dimension (Emerson et al., 1999; Lam, 2003; Lam and De Cola, 1993; Sun et al., 2006), lacunarity (Dong, 2000; Greenhill et al., 2003; Myint et al., 2006), and spatial autocorrelation (Cliff and Ord, 1973; Emerson et al., 2005; Lam et al., 2002). Studies that used both textural and spectral information in some LULC classification scenarios have also been made (Emerson et al., 2005; Myint and Lam, 2005a). However, these indices have seldom been integrated as a vector to aid image classification. The motivation of using a texture vector instead of individual textural index is similar to the motivation of using multiple spectral bands instead of single band in traditional satellite image classification. Because different textural indices are likely to capture different aspects of texture for the same image, it is expected that a texture vector will have the

capability to describe multiple aspects of the texture pattern of heterogeneous urban area; hence better classification results can be anticipated.

Another strategy to improving image classification accuracy is to improve the classifier itself by utilizing artificial intelligence. Recent research has demonstrated some successful classifiers, such as decision tree (Gislason et al., 2006; McIver and Friedl, 2002), support vector machines (Huang et al., 2002; Pal and Mather, 2005), and artificial neural network (Erbek et al., 2004; Huang et al., 2002). In practice, the selection of classifier is often a tradeoff between accuracy and efficiency. Although the traditional maximum likelihood classifier (MLC) is not the most accurate classifier in many cases, it is still widely used because it is simple and robust, and it can be carried out with minimal human-computer interaction. Hence, improving the operation of MLC could be promising, especially if the goal is to make the image classification process as easily automatable as possible for rapid monitoring applications.

The MLC has been widely used by the remote sensing community and was made available through most image processing platforms. The classifier calculates posterior probabilities of a pixel belonging to different LULC classes, and assigns it to the class with the highest posterior probabilities. In most satellite image classifications, prior probabilities are often assumed to be the same for all classes. They are rarely optimized with other methods except in some contextural classification using a Markov random field (MRF, Jackson and Landgrebe, 2002; Solberg et al., 1996). Some research used ancillary data to estimate prior probabilities, which means that an additional dataset and considerable efforts are required (Maselli et al., 1995; Pedroni, 2003). Because prior probabilities range between 0~1, an optimization approach could be applied to find the optimal prior probabilities to achieve higher classification accuracy. Genetic algorithms (GAs) have been found to be efficient and fast in many applications

(Armstrong et al., 2003; Li and Yeh, 2005). Hence, it is possible to use GAs to optimize the prior probabilities in the Bayesian classifier. Such an implementation of the GA will improve identification of class boundaries, thus a boosted performance can be achieved.

This research proposes a new method that combines the above two strategies. The method utilizes both a texture vector (fractal dimension, lacunarity, and Moran's *I*) and a genetic Bayesian classifier (GBC) to increase urban LULC classification accuracy. In the following, we will describe the essence of the two components of the method. An example is then demonstrated using a high-resolution IKONOS imagery acquired from Jefferson Parish (greater New Orleans), Louisiana. The image was taken in 2005.

5.2 A Texture Vector

Fractal dimension, lacunarity, and a spatial autocorrelation measure (Moran's *I*) were selected to be in the texture vector for this analysis because they have been shown to be effective in characterizing spatial patterns. Improvements to classification accuracy with these three indices have been reported in recent literature (Dong, 2000; Emerson et al., 2005; Myint and Lam, 2005a). Emerson et al. (2005) reported a 10% (67% to 77%) improvement in Landsat ETM+ imagery classification when a fractal layer was added to multispectral layers for classification. Dong and Leblon (2004) found that lacunarity measure was useful to improve rock unit discrimination by 8%. Myint and Lam (2005) reported that adding a spatial autocorrelation or lacunarity layer could improve land cover classification from 55% to 81% or 92%, respectively. Since the properties of fractal, lacunarity, and Moran's *I* seem to complement with each other, and they all measure spatial arrangements of pixels within the measurement window, combining these three indices into a vector for this analysis is expected to help improve classification. Moreover, unlike some other landscape indices, these textural indices can be

computed directly on either classified or unclassified images. This property is considered very important to future automation of image classification (Lam et al., 2008).

5.2.1 Fractal Triangular Prism Dimension

Fractal dimension (Mandelbrot, 1983) has been utilized to measure image complexity and landscape pattern of different LULC categories (Chust et al., 2004; Emerson et al., 1999; Lam and De Cola, 1993; Qiu et al., 1999). A higher fractal dimension means a rougher image surface. Different algorithms have been proposed to measure image fractal dimension, and it was found that a modified triangular prism method yielded the most accurate estimation (Clarke, 1986; Lam et al., 2002; Zhou and Lam, 2005). In this method, triangular prisms are constructed by connecting four corner pixels with the center pixel, with the z-position of the center point averaged from the intensity values of corner pixels. The step size S is the edge length (in pixel). The image surface area A is the total top surface area of the triangular prisms constructed on this image. The step size will increase and the total surface area will be measured at each step size. A regression is conducted between the logarithms of the total prism surface area and step size to derive the fractal dimension D:

$$LogA = a + (2 - D)LogS \tag{1}$$

where D will range from 2 to 3 (Lam et al., 2002).

The traditional methods of step selection to construct triangular prisms follow either geometric or arithmetic progression, which do not guarantee a full coverage of the entire image. Some edge pixels may be out of utilization at some step sizes. This exclusion is significant when small window size is used in local measurements. In this paper, a newly developed divisor-step method (Chapter 2) was used. In this method, step sizes are determined so that they are divisible by the window size, thus guaranteeing the inclusion of all pixels in local window calculation.

5.2.2 Gray-Scale Lacunarity

An image with the same fractal dimension can have different "gap" patterns (Mandelbrot, 1983). As a counterpart of fractal dimension, lacunarity was suggested to measure the "gap" distribution in an image. Higher lacunarity generally means a more porous pattern, and vice versa (Mandelbrot, 1983). Lacunarity has been utilized to characterize landscape patterns (Dale, 2000; Plotnick et al., 1993). It was applied recently to texture image analysis and was found to increase accuracy in urban LULC classification (Dong, 2000; Myint and Lam, 2005a; Myint et al., 2006). To calculate the lacunarity of a surface, a gliding cubic box (edge length: x) is usually used to cover through the image intensity space. Let $P(m, x)$ denote the probability of a box mass m (number of points) occurring in gliding box with length x, and let n denote the maximum mass. Then the lacunarity for a gray-scale image is shown as (Voss, 1986):

$$\Lambda(x) = [\sum_{m=1}^{n} m^2 P(m,x) - (\sum_{m=1}^{n} mP(m,x))^2] / [(\sum_{m=1}^{n} mP(m,x))^2] \quad (2)$$

5.2.3 Moran's *I*

Spatial autocorrelation refers to the similarity or dissimilarity of values between neighboring pixels (Cliff and Ord, 1973; Goodchild, 1986). Moran's I, a robust measure of spatial autocorrelation, has been applied locally to generate additional textural layer to improve classification (Emerson et al., 2005; Lam et al., 2002). These previous studies demonstrate the potential of using Moran's I as an aid in image classification. Moran's I is calculated as the following:

$$I(d) = (n\sum_{i}^{n}\sum_{j}^{n} w_{ij} z_i z_j) / (W\sum_{j}^{n} z_i^2) \quad (3)$$

where w_{ij} is the weight at distance d, w_{ij}=1 if point j is within a certain distance d of point i, otherwise w_{ij}=0; W is the summation of all weights for any $i \neq j$; z is the deviation from its mean

value. $I>0$ indicates a positive autocorrelation, $I<0$ indicates a negative autocorrelation; when there is a random pattern, I will be approaching 0.

5.2.4 Texture-Aided Classification and Texture Vector Method

Textural layers are often derived by using a recursive moving window and assigning the local measurement to the center pixel of the moving window. The generated textural layers can then be combined with spectral bands for classification. The effects of window size on texture measurements hence become critical to the resultant textural indices (Chen et al., 2004; Hodgson, 1998; Myint and Lam, 2005a). In addition to the above three textural indices, previous studies have utilized other textural techniques for image classification, such as the co-occurrence matrix (Carr and de Miranda, 1998), wavelet transform (Zhu and Yang, 1998), mathematical morphological operation (Plaza et al., 2004), and geostatistical metrics such as entropy, mean, variance, fragmentation index, diversity, and standard deviation (Carr and de Miranda, 1998; Zhu and Yang, 1998). However, with a few exceptions (Emerson et al., 2005; Myint and Lam, 2005a), the texture vector method has seldom been extended to combine fractal dimension, lacunarity, and Moran's I with spectral vectors for land cover classification. Given this research gap and their potential in complementing with each others, fractal dimension, lacunarity, and Moran's I were selected in this research to form a texture vector to describe more aspects of image "texture" and aid classification. Similar to the widely-used spectral green, red, and near-infrared bands, different textural layers can provide different textural perspectives, and in this case, the textural indices will measure the properties of complexity, gap distribution, and spatial autocorrelation.

5.3 Genetic Bayesian Classifier

5.3.1 Introduction to Genetic Algorithms

The development of GA was motivated from the evolutionary theory. GAs have been widely used in optimization problems (Goldberg, 1989). A simple GA can be described as follows.

GAs usually start with a randomly-generated population that contains some chromosomes, and then the offspring are generated by combining or changing the genes of the parent chromosomes, known as crossover and mutation, according to predefined rates. A solution is defined as a chromosome which is comprised by genes and usually encoded as bit strings or real numbers. The goodness of a chromosome is evaluated by a fitness function. The fitness value of a chromosome determines its chance of being selected to reproduce offspring. The chromosomes with top fitness values can be kept in the next generation as elite members. The evolution continues until it meets the stopping criteria such as no fitness improvement after a number of generations.

5.3.2 The Proposed Genetic Bayesian Classifier

According to the Bayes theorem, given an image training data D and classification space C (e.g., forest, pasture, urban, etc.), let $P(c)$ denote the prior probability of class c and $P(c|D)$ denote the probability of the pixel belonging to class c given training data D. Under the independent assumption of the training pixels, following Mitchell (1997), we have

$$P(c|D) = \prod_{i \in D} p(d_i|c) \bullet P(c) / P(D) \qquad (4)$$

Assume that the distribution of the training data D is a multivariate Gaussian distribution and let u and S denote the mean vector and the covariance matrix of class c in the training sample respectively. By taking the natural logarithm of the above equation, we have

$$\ln P(c|D) = -\frac{1}{2}(x-u)^T S^{-1}(x-u) - \frac{N}{2}\ln(2\pi) - \frac{1}{2}\ln(|S|) + \ln P(c) - \ln P(D) \qquad (5)$$

The classification *c* of a pixel satisfies:

$$\arg\max_{h\in H}[\ln P(c) - \frac{1}{2}(x-u)^T S^{-1}(x-u) - \frac{1}{2}\ln(|S|)] \qquad (6)$$

Equation (6) is the general form of MLC. In traditional remote sensing classification, the prior probabilities are often assumed to be the same for each class, which neglects the importance of this parameter. Previous literature demonstrated the use of MRF to model prior probabilities in contextual classification (Jackson and Landgrebe, 2002; Solberg et al., 1996), but a direct optimization of prior probabilities is seldom explored. Some research used ancillary data to estimate the prior probabilities (Maselli et al., 1995; Pedroni, 2003), but such an approach requires an additional dataset and significant extra processing cost. Since GAs have been proven to be an efficient optimizing method (Armstrong et al., 2003; Li and Yeh, 2005), it can be used here to optimize the prior probabilities by fitting the goal of maximizing classification accuracy. The equal probability solution of traditional MLC can be included as a seed in initial population. For convenience, we define this method as GBC.

If *m* denote the number of classes, the problem is to derive the optimal solution of {*P* |i=1,…,m} with the constraints:

$$\sum_{i=1}^{m} P(c_i) = 1, where P(c_i) > 0 \qquad (7)$$

The problem can be further simplified to search the solution of {*P'*|i=1…m}. Let *P'* belongs to (0, 1); then the solution of prior probabilities is

$$P(c_i) = P'(c_i) / \sum_{i=1}^{m} P'(c_i) \qquad (8)$$

The fitness function is defined as follows. Given a solution of prior probabilities for classifying the training set, let N denote the number of correctly classified pixels and L denote the total number of training pixel. Then the fitness function (using overall accuracy) is:

$$f = N / L \tag{9}$$

An important concern of training classifiers is to avoid overfitting. A common solution to this problem is cross-validation. The training data can be separated into several sets, with one set used for validation and the others for training. Then the fitness criterion is the weighted average of overall accuracies for all validation sets, and the fitness function (Equation 9) is still valid, with N denoting the number of correctly classified pixels from all validation sets and L denoting the total number of training pixels.

In the following case study, P' is encoded as real numbers within (0, 1) with four decimal places. The GA used in this paper was programmed in MATLAB according to the version described in Section 3.1, but with an additional procedure for checking uniqueness. This procedure was employed after the reproduction that removes duplicated chromosomes and generates replacements randomly. A worked example is shown in Appendix 1.

5.4 Research Design

A subset of an IKONOS image of greater New Orleans, Louisiana, was used in this study (Figure 5.1). The subset size was 481 x 621 pixels for multispectral bands. Based on the LULC categories available in the subset, a combined USGS level I and II classification scheme was used (Anderson et al., 1976), which included six classes: water, forest, residential, grassland, commercial, and industrial (Figure 5.2).

For the classification scheme, residential class refers to areas used primarily for residential purposes, including houses, amenity grasses/trees, small private roads, and others. Commercial

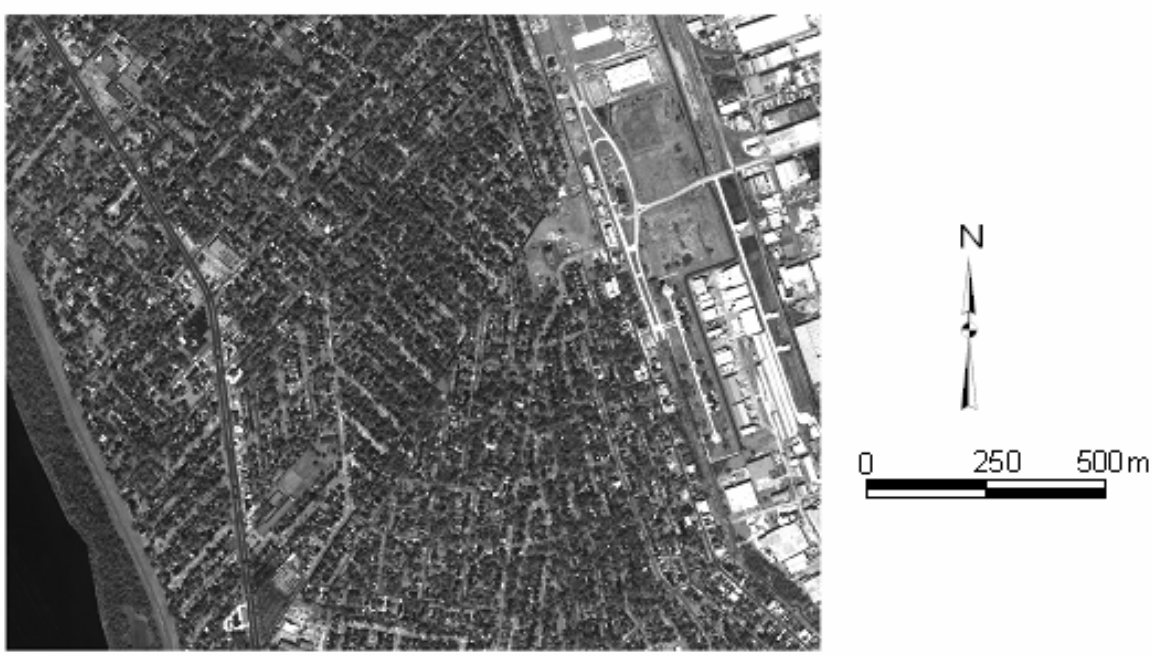

Figure 5.1 IKONOS panchromatic band of the study area (Jefferson Parish, Louisiana) acquired on Sep. 2, 2005. Image size: 1924 by 2484 pixels.

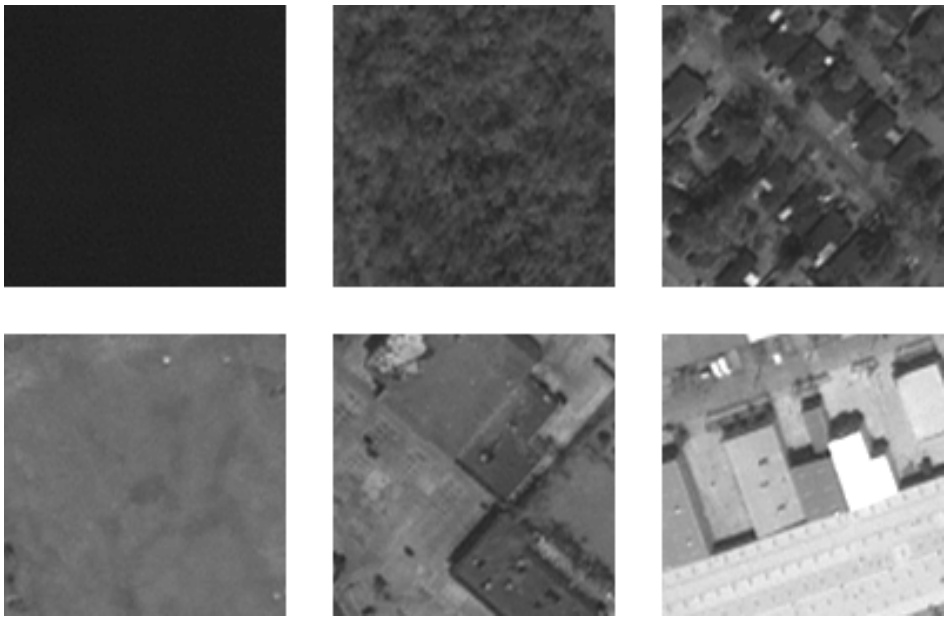

Figure 5.2 Selected training areas (120 by 120 pixels) shown in IKONOS panchromatic band; clockwise from upper left: water, forest, residential, industrial, commercial, and grassland.

class is used predominantly for the sale of products and services, including shopping centers, retail stores, office buildings and associated parking lots. Industrial class is associated with light/heavy manufacturing. Water, forest, and grassland refer to areas dominated by the corresponding land cover. Representative training areas for the six classes were carefully selected across the study area based on field survey and reference to half-foot (0.15meters) resolution aerial images taken in September 2005. Descriptive statistics of different LULC categories in terms of their spectral characteristics are listed in Table 5.1. It is clear from Table 5.1 that water, forest, and grassland classes had smaller spectral variations (i.e., smaller standard deviations and coefficients of variation), whereas the three land use classes that are characterized by intensive human activities (residential, commercial, and industrial) had higher spectral variations with higher standard deviations and coefficients of variation.

The 1-meter IKONOS panchromatic band (1924 by 2484 pixels) was used to extract textural layers of fractal dimension, lacunarity, and Moran's *I* (Figure 5.3). To be compatible with the 4-meter resolution multispectral bands, these textural layers were then downsampled and stacked with the three multispectral bands (red, green, and near-infrared) such that each pixel had a three-dimensional spectral vector and a three-dimensional textural vector. This method will avoid the high-dimensionality problem and also take advantage of the higher spatial-resolution panchromatic band for reducing the blurring effects.

For the GA, we used a common configuration with 30 population, 0.8 crossover rate, random point crossover/mutation, and 2 elite members. The stopping criterion was no improvement in 20 continuous generations. To minimize the random effects of the GA, the training stage was performed three times and the best results were used in subsequent analyses. A flow chart of the research design is shown in Figure 5.4.

Table 5.1 Descriptive statistics of the six LULC classes

Band	Land Use	Min	Max	Mean	SD	CV
Band4	Water	147	170	158.02	4.38	0.03
	Forest	300	594	431.46	55.66	0.13
	Residential	215	883	486.95	122.94	0.25
	Grassland	567	980	740.43	73.01	0.10
	Commercial	258	877	564.72	90.58	0.16
	Industrial	234	1927	696.96	183.78	0.26
Band3	Water	215	242	228.38	5.86	0.03
	Forest	211	325	241.97	16.89	0.07
	Residential	201	817	288.73	61.55	0.21
	Grassland	276	363	304.07	18.12	0.06
	Commercial	260	971	540.57	100.71	0.19
	Industrial	262	1963	708.04	227.80	0.32
Band2	Water	392	414	402.91	4.84	0.01
	Forest	352	442	380.23	13.17	0.03
	Residential	350	888	422.60	50.33	0.12
	Grassland	440	504	463.13	13.22	0.03
	Commercial	411	935	626.04	80.12	0.13
	Industrial	445	1982	821.70	204.70	0.25

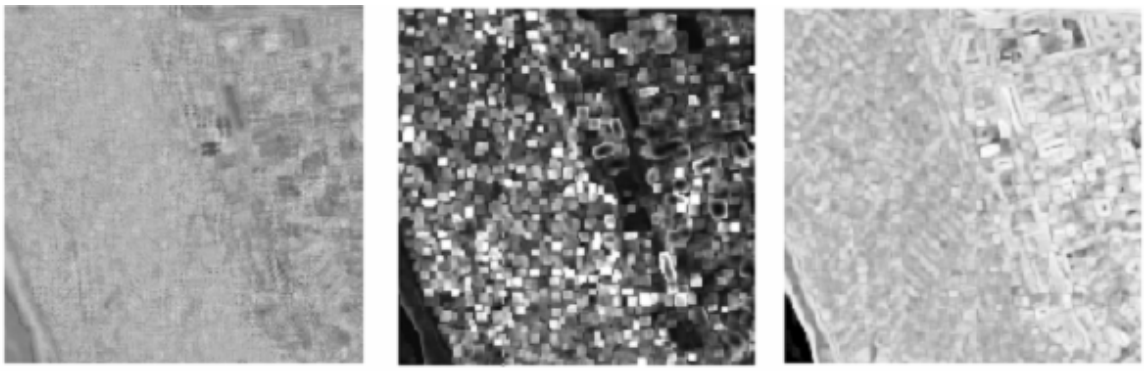

Figure 5.3 Textural layers extracted from an IKONOS image acquired on Sept. 2, 2005 of Jefferson Parish, Louisiana (greater New Orleans) (left to right: fractal dimension, lacunarity, Moran's *I*).

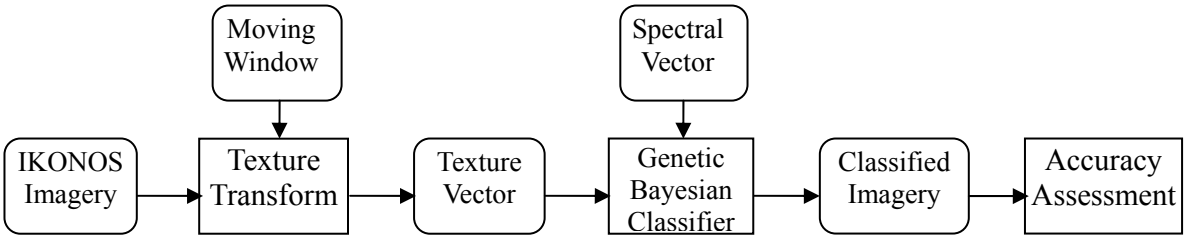

Figure 5.4 Flowchart of the Genetic Bayesian texture-aided classification process.

The original 11-bit IKONOS image was used for textural layer extraction (Myint and Lam, 2005). The textural layers were stretched linearly to 0-2048 such that each layer was within the same range. Four moving-window options, 33x33, 45x45, 55x55, and 65x65 pixels (meters), were used. For lacunarity layer extraction, the 3x3x3 gliding box was used; for Moran's *I* layer extraction, only neighbored pixels (Rook's case) were considered.

Two strategies were applied to reduce the edge and blurring effects caused by moving-window based texture measurements. First, because edge effects are more significant with local measurements, a variant of Zhou-Lam method (2008) was applied in this study to partially overcome the edge effects. Second, training areas were randomly sampled to minimize the blurring effects of moving window and high correlation among measurement in neighboring areas (Sun et al., 2006). The training data contained 5000 pixels. Classification accuracies were assessed with a common stratified sampling strategy based on the classified map. The evaluation

data consisted of 1716 points, and identification of their actual land cover types were made through reference to the half-foot (0.15meters) resolution aerial images (taken in September 2005) and field survey. Recent literature demonstrates some alternative accuracy assessment methods, such as fuzzy assessment (Binaghi et al., 1999), area-based confusion matrix (Lewis and Brown, 2001), and multiple-resolution method (Pontius and Cheuk, 2006). These methods can be integrated in the fitness function and evaluation procedure in future studies. For this case study, we used the traditional hard-classification-based cross tabulation accuracy assessment method. The GBC, MLC, image classification procedure, and accuracy calculation were programmed and automated in MATLAB.

In addition, to provide a better perspective of how GBC and MLC are compared with other classifiers, a multi-layer perceptron neural network classifier (NNC) was also tested. For NNC, typically a three-layer neural network is used in LULC classification, with input and output neurons configured as the number of spectral and textural bands and the number of classes, respectively. Since there are no theoretical guidelines of configuring hidden neurons, in this study the neurons of hidden layer were set to one, two, or three times of input neurons. For each configuration, the network was run three times with different random weights and bias settings. Bayesian optimization was used to avoid overfitting using MATLAB Neural Network Toolbox.

5.5 Results and Analysis

The overall classification accuracies from different classification scenarios are shown in Table 5.2. Generally, by introducing additional textural information or using GBC or NNC to replace the MLC, overall accuracies increased. The best performance occurred in the case of 65x65 window, with the overall accuracies boosted to 87% for MLC and about 90% for both GBC and NNC, using texture vector-aided approach. Classified maps are shown in Figure 5.5.

Table 5.2 Classification accuracy (%) among different classification approaches

Window	MS*			MS-Fractal			MS-Lacunarity			MS-Moran			MS-Vector		
(meter)	MLC	GBC	NNC	MLC	GBC	NNC	MLC	GBC	NNC	MLC	GBC	NNC	MLC	GBC	NNC
33x33	68.5	80.6	80.5	69.2	81.1	82.2	83.2	87.0	88.2	74.0	82.9	83.6	84.3	88.0	89.0
45x45	68.5	80.2	80.2	68.2	81.0	81.8	84.7	87.5	89.2	72.5	82.1	82.6	85.9	88.5	90.3
55x55	68.5	80.2	81.1	69.9	82.1	83.2	85.3	88.5	88.9	71.6	81.9	82.2	86.0	88.8	90.2
65x65	68.5	80.2	80.4	70.2	82.1	83.0	85.6	88.5	89.4	71.3	81.6	82.8	86.6	89.6	90.7

(*MS: multispectral)

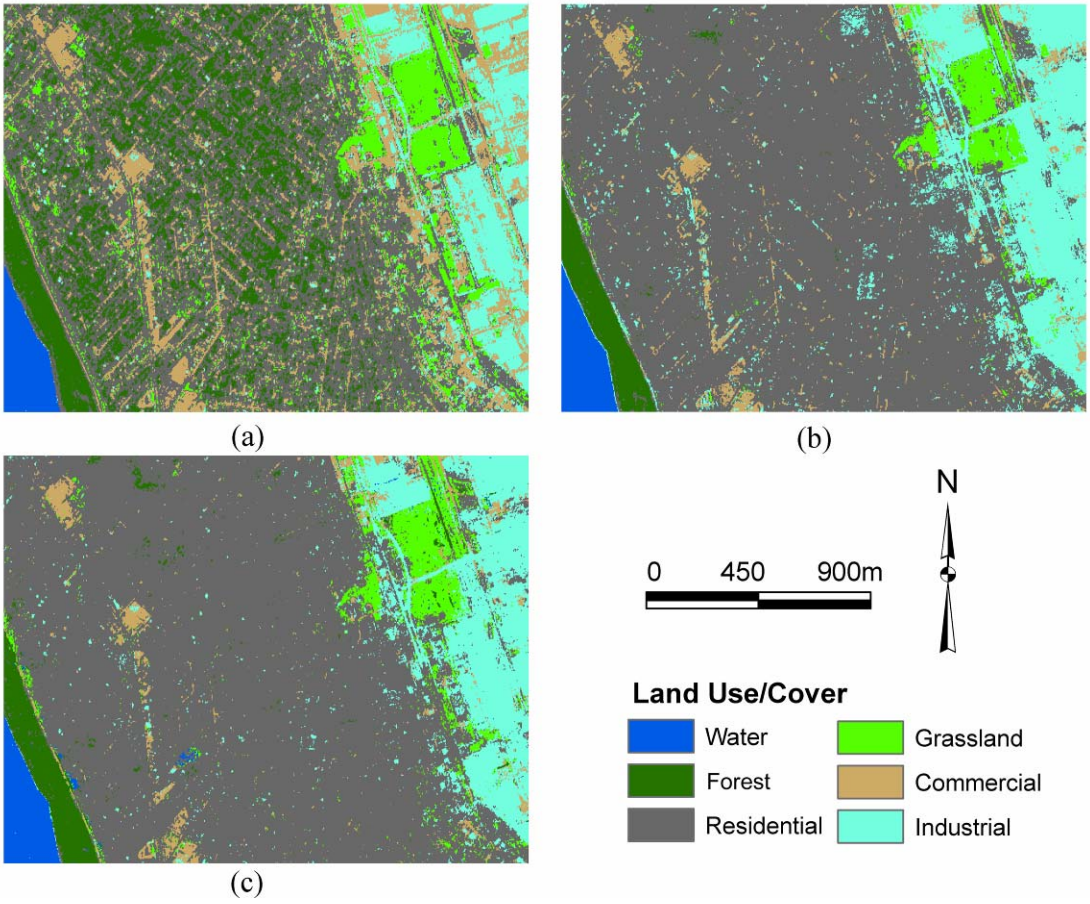

Figure 5.5 Classified LULC maps using IKONOS multispectral band 4,3,2 and textural layers. (a) MS with MLC; (b) MS-vector with GBC; (c) MS-vector with NNC.

5.5.1 Genetic Bayesian Classifier Versus Maximum Likelihood Classifier

The performance comparison includes two aspects: accuracy and computational efficiency. For accuracy, Figure 5.6 shows that the proposed GBC outperformed the traditional likelihood classifier in all scenarios; and such improvement was the greatest when no texture vector was used. In other words, using the GBC alone can increase accuracy more than 10% (Table 5.2). A one-to-one comparison with Kappa *Z* statistics was provided in Table 5.3. The *Z* values of GBC versus MLC were all greater than the 0.05 significance level ($Z>1.96$), implying that the classification accuracy of GBC was significantly higher than that of MLC.

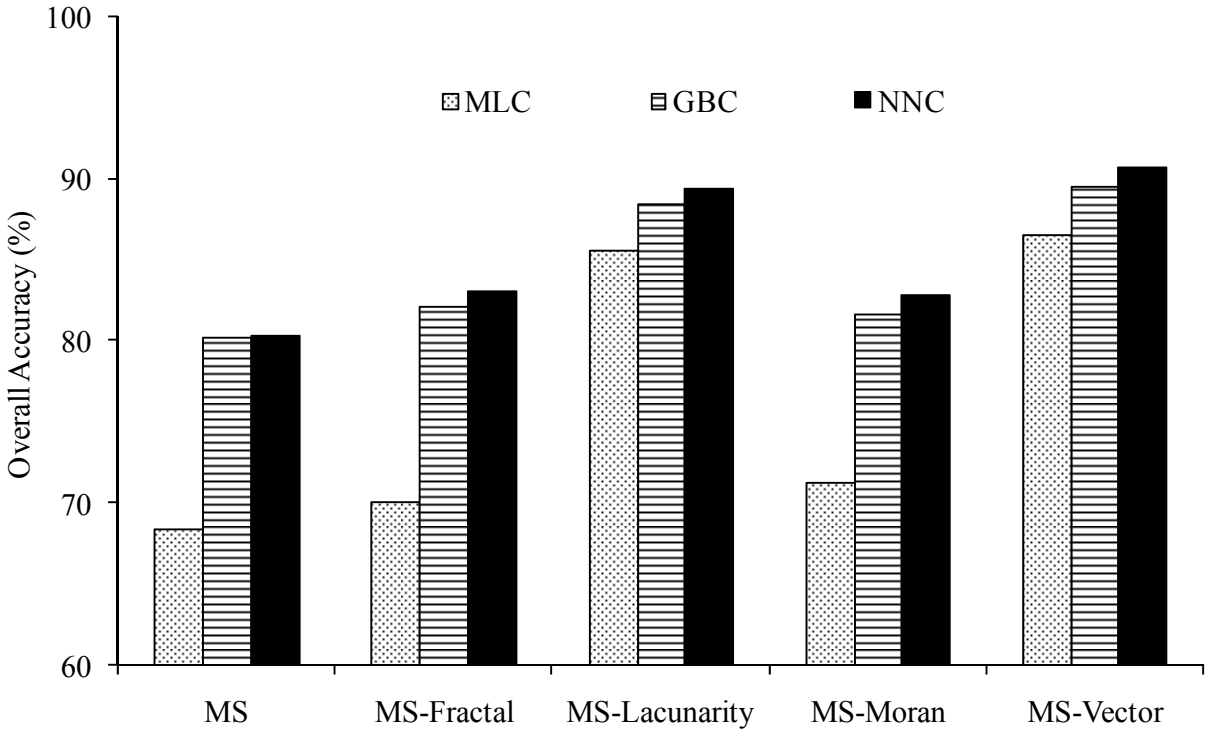

Figure 5.6 Overall accuracies (%) among different texture-aided classification with different classifiers at window size: 65x65.

Table 5.3 Kappa Z statistics among classifiers for window size 65x65

Classifier	MS	MS-Fractal	MS-Lacunarity	MS-Moran	MS-Vector
GBC vs MLC	5.260*	6.062*	2.052*	5.104*	2.747*
NNC vs MLC	4.527*	6.337*	2.864*	5.632*	3.286*
NNC vs GBC	-0.712	0.282	0.799	0.524	0.529

*: significant at 0.05 level (Z>1.96)

Another important aspect of performance is computational efficiency. On a Sun Microsystems workstation (dual dual-core AMD Opteron processor 2.41GHz, 4GB RAM), the training time for different scenarios varied from 5.9 to 8.3 seconds, and the number of generations needed varied from 37 to 87, with an average of 6.1 seconds and 61 generations. Hence, the GBC is still computationally efficient. When considering both accuracy and computational efficiency, we may conclude that the GBC outperformed the traditional MLC.

5.5.2 Genetic Bayesian Classifier Versus Neural Network Classifier

In terms of classification accuracy, the NNC yielded slightly better results than the GBC (Figure 5.6 and Table 5.2). However, the *Z* statistics of NNC versus GBC were not significantly different, indicating similar performance between the two classifiers.

In terms of computational efficiency, the NNC was much less efficient than the GBC. In this study, when the number of neurons in the hidden layer was set to twice as the number of input neurons, the computational time used was from 350 to 2568 seconds for this small training set (5000 pixels). It would be even more time consuming if multiple hidden layer configurations and multiple randomized weight/bias settings were used. More importantly, the NNC requires considerably more human-computer interaction to configure different structure settings. Some training algorithms may require users to interactively stop the training process. On the other hand,

the GBC has a fixed structure and requires no structure configurations and manual stop. The ease of use for GBC will be an advantage, especially after the procedure is programmed and made available to the end user.

5.5.3 Texture Vector Method Versus Individual Textural Index Aided Approach

Considering only the MLC, the improvement of texture-aided approach over the per-pixel spectral classification varied from individual index to index, while the composite texture vector approach yielded the greatest improvement (16-19%, see Table 5.2 and Figure 5.6). Among the three textural indices, lacunarity outperformed fractal dimension and Moran's *I* at all moving-window sizes. Fractal dimension and Moran's *I* had similar performance. The composite texture vector outperformed individual index aided approach. For the MLC, the baseline overall accuracy with only three multi-spectral layers was 68.5%, while the use of a texture vector improved it by 6-8% to 84-86%, depending on the size of the moving window. Similar performance trends can be observed for other classifiers. The addition of textural information for image classification has increased the classification accuracy.

5.5.4 Window Size Effects

In general, for the four window sizes tested in this study (from 33x33 to 65x65 meters), their effects on classification accuracy were very small and negligible. The maximum-minimum accuracy difference for either individual index or texture vector was within 3% (Table 5.2). Nevertheless, we can observe that for the MLC, larger windows generally yielded slightly higher accuracies for fractal- or lacunarity-aided approaches, whereas the classification accuracy of using Moran's *I* method decreased slightly with increasing window sizes. The combined effects resulted in a slight increasing trend for the texture vector-aided approach. Using the GBC or NNC, these trends were generally maintained but with some additional fluctuations due to the

stochastic nature of the techniques. Future research that uses wider range of window sizes is needed to derive the quantitative relationships between window size, object size, and index.

5.5.5 Stochastic Characteristics of GBC and NNC

Unlike the deterministic results derived from using the MLC, both the GBC and NNC exhibited some stochastic characters. With different initial parameter settings such as the randomized initial population of GA and randomized weights and biases of neural network, slightly different classification results could be yielded. This stochastic characteristic can be also observed in Table 5.2, when the same multi-spectral information was used for the four windows. Accuracy results were the same for the MLC but they were inconsistent for GBC and NNC. As discussed above, this stochastic characteristic could also slightly blur the window size effects. Following a common practice used by most research (Armstrong et al., 2003), both the GBC and NNC were run multiple times to get the best trained classifier for classification.

5.5.6 User's and Producer's Accuracies of the Genetic Bayesian Classifier

A further examination of the accuracies of individual LULC categories provided more valuable information of different classification approaches. Considering both producer's accuracy (1 - commission error%) and user's accuracy (1 - omission error%), the texture vector-aided approach with the GBC outperformed the spectral-based MLC for most LULC categories, as did the texture vector-aided approach with the NNC (Tables 4.4-4.6). Significant improvements occurred in the user's accuracies of forest, grassland, commercial and industrial classes, and in the producer's accuracy of residential and industrial classes. These improvements were reflected on the classified map (Figure 5.5), where some residential neighborhoods were misclassified into forest in the MLC, but were correctly classified with the texture-aided GBC/NNC approaches. However, unexpectedly, the commercial class had a poorer producer's

Table 5.4 Accuracy assessment of spectral-only classification with the MLC

C* / R*	Water	Forest	Residential	Grassland	Commercial	Industrial	Producer's (%)
Water	116	0	2	0	0	0	98.3
Forest	0	114	16	3	0	0	85.7
Residential	0	226	600	40	97	22	60.9
Grassland	0	0	25	113	9	11	71.5
Commercial	0	0	20	3	62	10	65.3
Industrial	0	0	2	2	53	170	74.9
User's(%)	100	33.5	90.2	70.2	28.1	79.8	68.5

(R*: Reference data, C*: Classified results)

Table 5.5 Accuracy assessment of texture vector- aided classification with the GBC

C* / R*	Water	Forest	Residential	Grassland	Commercial	Industrial	Producer's (%)
Water	116	0	0	0	0	2	98.3
Forest	0	123	10	0	0	0	92.5
Residential	0	2	934	0	21	28	94.8
Grassland	0	0	40	98	4	16	62.0
Commercial	0	0	29	3	50	13	52.6
Industrial	0	0	4	0	7	216	95.2
User's(%)	100	98.4	91.8	97.0	61.0	78.5	89.6

(R*: Reference data, C*: Classified results)

Table 5.6 Accuracy assessment of texture vector-aided classification with the NNC

C* / R*	Water	Forest	Residential	Grassland	Commercial	Industrial	Producer's (%)
Water	116	0	0	0	0	2	98.3
Forest	0	123	9	1	0	0	92.5
Residential	1	6	957	3	10	8	97.2
Grassland	0	6	24	109	7	12	69.0
Commercial	0	1	32	3	48	11	50.5
Industrial	0	0	15	1	8	203	89.4
User's(%)	99.1	90.4	92.3	93.2	65.8	86.0	90.7

(R*: Reference data, C*: Classified results)

accuracy for both the GBC and NNC than the MLC, as some commercial lands were omitted on the classified map (Figure 5.5b and 4.5c).

When comparing the GBC and NNC, the differences among individual LULC categories were subtle, and their small difference in overall accuracy as reflected by the insignificant Kappa statistic (Table 5.3). For both GBC and NNC, the user's and producer's accuracies of water, forest, and residential were more than 90%, indicating clear separation among these classes by these two classifiers. User's and producer's accuracies for the industrial class ranked second, followed by those of the commercial class. Scattered houses with commercial activities in large residential and industrial neighborhoods made it hard to classify, thus resulted in the worst accuracies for commercial lands. More studies are needed to develop strategies for achieving better classification accuracy for the commercial class.

5.6 Conclusions

Integrating artificial intelligence classifiers and texture information into the image classification process has proven to be fruitful in terms of improved accuracy. This paper presented a combined classification methodology using a texture vector method and the newly-developed GBC. The test of an IKONOS image of an urban area in New Orleans showed a 17-21% improvement by using the combined approach, or a more than 10% improvement by using the GBC alone, compared with the spectral-based MLC method.

As expected, the texture vector method was found to outperform the individual textural method, regardless of the classifier used. For individual textural index-aided approach, Lacunarity outperformed Moran's *I* and fractal dimension. The combined approach of texture vector with the GBC yielded a classification accuracy of 90% at window size of 65x65 meters, a 21% improvement over the 69% accuracy obtained from using the spectral-only MLC method. However, despite the significant overall accuracy improvement by the new approach, the commercial class had no improvement and remained to be very difficult to separate, with yielded user's and producer's accuracies of only 61% and 52.6%, respectively.

When compared with the extensively researched NNC, the GBC was found to yield statistically the same accuracies. However, the high computational efficiency, the ease of use, and the minimal requirement of human-computer interaction of the new GBC could make it an attractive alternative for future image classification. With further refinements and more experiments in the future, the GBC algorithm could be implemented into existing image processing software as an option provided to traditional MLC.

This study is limited by the fact that only one study area was experimented. Similar to the NNC which has been tested extensively in the literature, the performance of GBC is in need of

future tests using images from different study areas with different LULC compositions, different time periods, and different sensors. Future studies on different combinations of textural indices to find the optimal composite texture vector are also needed to help further improve image classification and segmentation.

Chapter 6
Integrating a Texture Vector with Artificial Intelligence in Urban Land-Use/Land-Cover Classification and Residential Neighborhood Discrimination

6.1 Introduction

The proposed launch of Geoeye-1 in 2008 will promote high-resolution remote sensing to a new era, with a 0.41-meter spatial resolution panchromatic band and 1.65m resolution multispectral bands. Along with QuickBird and IKONOS, commercial high-resolution satellite imagery from different vendors further enhances the role of remote sensing in inventorying land resource, monitoring environmental change, detecting and assessing hazards. Even in the public domain, some high-resolution imagery can be freely accessed through online mapping service providers such as Google, Microsoft, and MapQuest.

Land-use/land-cover (LULC) classification and change detection is a fundamental application of remote sensing and remains a major scientific topic in geographic information science. High-resolution satellite imagery greatly challenges the traditional per-pixel classification method, as different land use categories may carry similar ground components (Emerson et al., 2005). Recent research demonstrated that the use of neighborhood spatial analytical indices and artificial intelligence algorithms could provide improved classification (Huang et al., 2002; Myint and Lam, 2005a). Texture analysis techniques provide additional neighborhood information ignored by traditional per-pixel classification, such that classes are better characterized. Such techniques include lacunarity analysis (Dale, 2000; Greenhill et al., 2003; Myint et al., 2006), fractal modeling (Chust et al., 2004; Emerson et al., 2005; Read and Lam, 2002), spatial autocorrelation, and semivariogram (Carr and de Miranda, 1998; Emerson et al., 2005; Miranda et al., 1998). Artificial intelligence classifiers provide an alternative for

deriving better classification boundaries and relieve the strict restriction of parametric modeling, thus better accuracies can be achieved. Such methods include decision trees (DeFries et al., 1998; Gislason et al., 2006; McIver and Friedl, 2002; Pal and Mather, 2003), artificial neural networks (Erbek et al., 2004; Liu and Lathrop, 2002; Mills et al., 2006), and support vector machines (Bazi and Melgani, 2006; Foody and Mathur, 2004b; Huang et al., 2002; Pal, 2006).

One growing direction of remote sensing applications is in the social sciences (Liverman et al., 1998; Zhou, 2006) and disaster monitoring (Kerle et al., 2003; Tralli et al., 2005). The study area, metropolitan New Orleans, which was inundated on August 29, 2005 by Hurricane Katrina, impacted different residential neighborhoods with different economic/environmental statuses. These neighborhoods exhibited different spectral and textural appearance, which could possibly be discriminated utilizing a classification approach with textural information.

Using the maximum likelihood classifier (MLC) as a baseline, this chapter further investigates the performance of integrating the texture vector-aided approach (see Chapter 4 and 5) with three different classifiers: support vector machines (SVM), artificial neural network classifier (NNC), or genetic Bayesian classifier (GBC). Two classification scenarios were carried out. First, an image mosaic with different LULC types identified from metropolitan New Orleans on the IKONOS image taken after Hurricane Katrina was examined. The second study examined four urban residential neighborhoods with different incomes and inundation statuses.

6.2 Introduction to Neural Network Classifier and Support Vector Machines

In this research, both a spectral-only approach and a spectral-textural approach were tested with the four different classifiers. The texture measures include fractal dimension, lacunarity, and Moran's *I*, which are three distinct image textural indices with different emphases on complexity, heterogeneity, and auto-correlation. In previous experiments (Chapter 5), the integration of these

three indices successfully described more aspects of image texture, as each index measures a certain characteristic of spatial arrangements. The four classifiers include the traditional MLC, GBC, multi-layer perceptron NNC, and genetic algorithm - support vector machines classifier (GASVM). The algorithm of GBC can be found in a previous chapter (Chapter 5), while simple introductions to NNC and GASVM are to follow.

6.2.1 Multi-Layer Perceptron Neural Network

Artificial neural networks are a group of robust computational models inspired by the biological learning behavior of the human brain. A neural network model contains several layers of interconnected neurons (nodes). Each neuron takes a number of inputs and produces an output that could be the final result or the input for other neurons. Training of neural networks can be supervised, such as the multi-layer perceptron (MLP) network (Demuth et al., 2008; Erbek et al., 2004), or unsupervised such as Kohonen Self-organizing Map (Ju et al., 2006; Kohonen, 1995). Commonly, the MLP network (Figure 6.1) is used when classifying remote sensor data (Huang et al., 2002). The following description of the MLP network follows the work by Demuth et al. (2008).

In a MLP network, the output of each neuron in the hidden layers and output layer is a transformed value of the weighted summation of the inputs from previous layers plus a bias. The MLP network will learn its weights and biases by minimizing the difference between the produced output and the target output. Several different learning algorithms exist, such as gradient decent, conjugate gradient, Quasi-Newton, and Levenberg-Marquardt (Demuth et al., 2008).

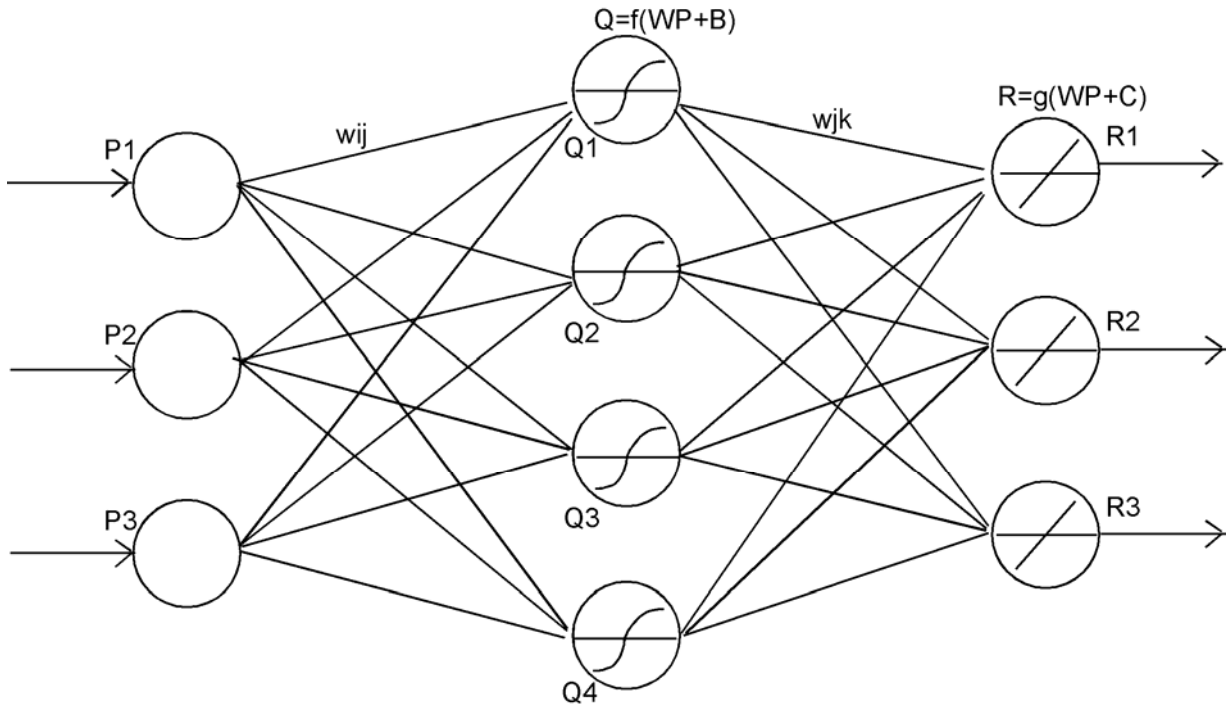

Figure 6.1 A common three layer (3-4-3) MLP network. P, Q, R corresponds to the value of input, hidden, and output neurons. The figure follows the demonstration in Demuth et al. (2008).

A typical learning process is outlined as the following:

(a) Initialize the network;

(b) Input training instances and compute outputs and performance; both the outputs of hidden neurons and output neurons will be calculated. The output is: $Q_j = f(\sum_{i=1}^{n}(w_{ij} p_i + b_{ij}))$

where p_{iij} is the value (output) from the i^{th} neuron in the previous layer, w_{iij} and b_{iij} corresponds to the weight and bias (a constant) of the i^{th} neuron. f is the transform function (e.g. sigmoid function, cosine function). Q_j is the output from the j^{th} neuron. A demonstration is made in Figure 6.1.

A simple performance function is the sum of square error:

$$SSE = \sum_{i=1}^{n}\sum_{j=1}^{m}(t_{ij} - o_{ij})^2 \qquad (1)$$

Where i is the i^{th} input instance, j is the j^{th} output neuron, t_{ij} and o_{ij} is the target and network predicted output values of i^{th} input instance on the j^{th} output neuron.

(c) Adjust the weights and biases

The gradient descent rule updates the weights and biases along the most rapid decreasing direction of the performance function:

$$\begin{bmatrix} w_{k+1} \\ b_{k+1} \end{bmatrix} = \begin{bmatrix} w_k \\ b_k \end{bmatrix} - \alpha_k g_k \tag{2}$$

where w_k and b_k are the k^{th} state of weights and biases; and a_k and g_k are the learning rate and gradient as of the k^{th} state.

(d) Repeat b-c until stop criteria met or interactively stopped.

As the learning process continues, the neural network could be trained to overfit the training data, which has poor generalization and will not respond well to unknown data. Several strategies can be used to prevent the occurrence of overfitting, such as early stopping and Bayesian regularization. Early stopping requires an additional validation data set to stop training earlier according to the performance on the validation data. Since the early stopping method could waste part of the training data, Bayesian regularization was suggested (Demuth et al., 2008). For Bayesian regularization, a cost function is added to the conventional performance function:

$$F = \alpha \times MSE + (1-\alpha) \times MSW \tag{3}$$

Where *MSE* is the mean square error between the prediction and the target outputs, and *MSW* is the means square weights. By supplying an additional cost function *MSW*, weights and biases are forced to be smaller, yielding a more stable output. MacKay (1992) provided an automated way of approaching optimal regularization parameters and it is implemented in the MATLAB neural network toolbox. A typical training process is illustrated in Figure 6.2.

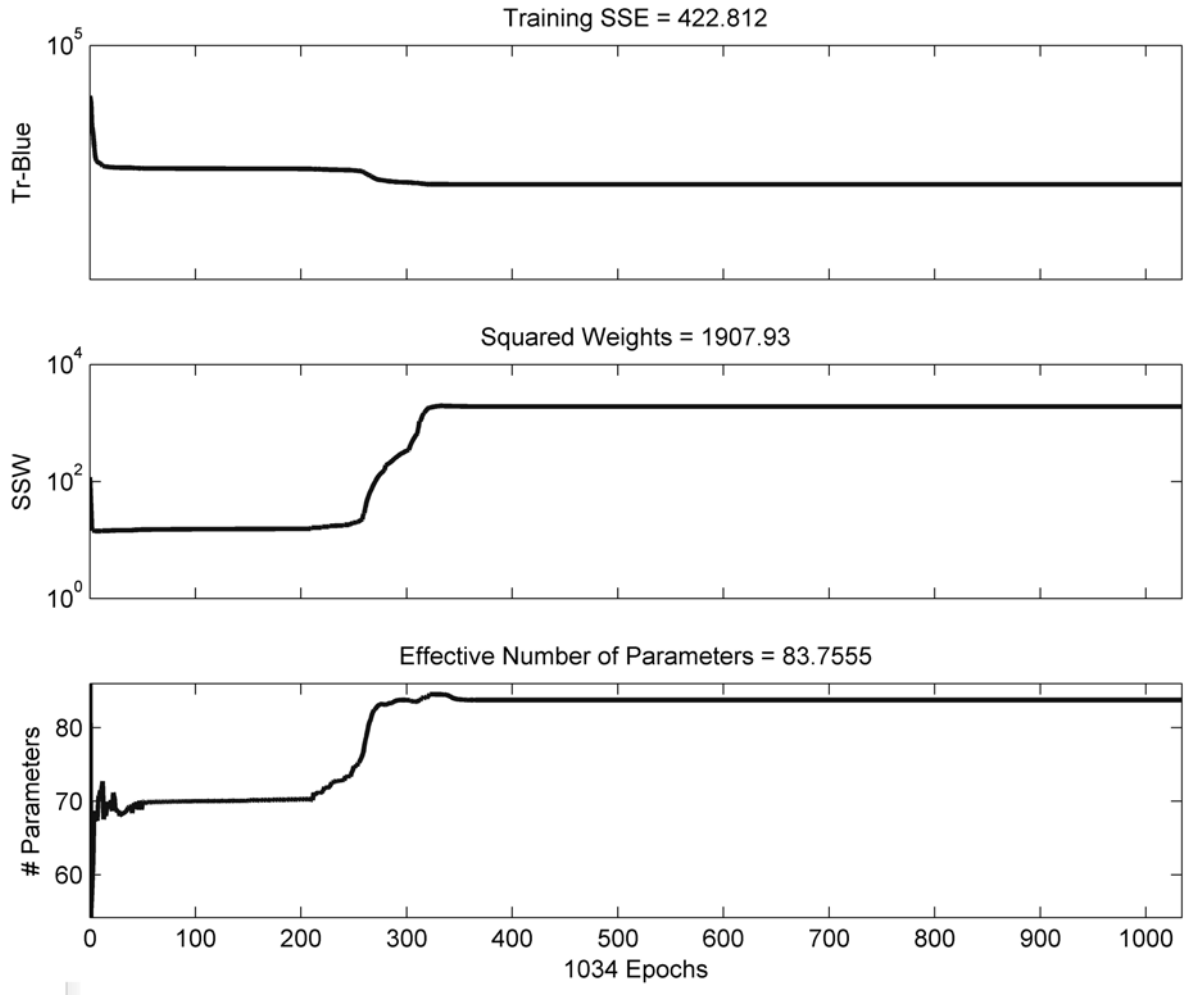

Figure 6.2 Learning curve of a three-layer back-propagation neural network with Bayesian regularization. *SSE* and *SSW* stand for sum of square errors and sum of square weights, respectively. The figure is an MATLAB output from one experiment in this chapter.

There are pros and cons of using neural network in classification. In contrast to MLC which assumes a Gaussian distribution, NNCs make no a prior assumption of data distribution. Hence, it could have a better fit to complex LULC classification, especially in an urban area. However, there are no universal guidelines for choosing network parameters. A trial-and-error approach is often required to determine the network structure. The training stage requires a significant amount of time.

6.2.2 Genetic Algorithm -- Support Vector Machines

The SVM is a machine learning technique that looks for the best decision boundaries with least structural risk (Tan et al., 2005; Vapnik, 2000). Considering a satellite image with two bands, each pixel is plotted in attribute space instead of the original coordinate space (Figure 6.3a). These pixels belong to two LULC categories represented with circles (residential) and squares (commercial). The SVM algorithm considers only the training pixel that lie on the class boundaries; as the other pixels are not necessary for class discrimination (Figure 6.3a). These pixels that lie on the class boundaries are so-called support vectors, as each pixel is a 2-dimensional (2 bands) vector in the attribute space. The algorithm looks for the decision boundary between the two land use classes with maximum margin achieving the best generalization power, as represented by the solid black line in Figure 6.3a. The mathematical process to search for this best separating class boundary is described next by following Tan et al. (2005) and Vapnik (1998; 2000).

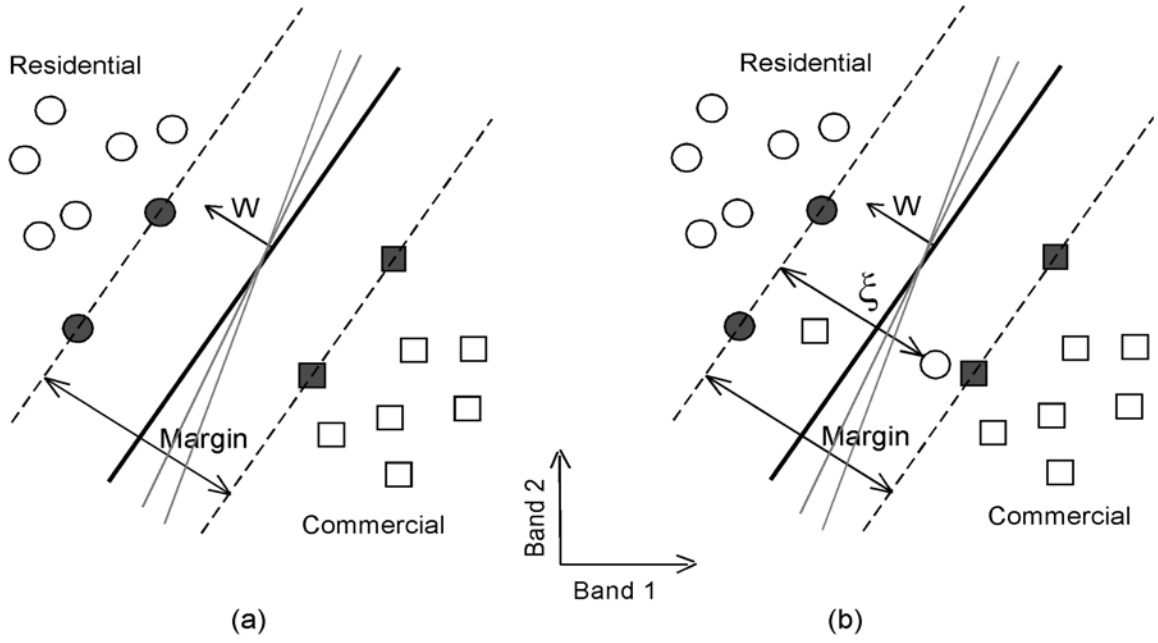

Figure 6.3 Linear decision boundaries for a separable case (a) and a non-separable case (b). Training pixels that lie on the parallel lines are support vectors.

Suppose the residential and commercial land use categories are linearly separable as indicated in Figure 6.2a. Let X_i denote the ith training sample in two dimensional attribute space (band 1 and band 2) and let y_i be the binary class label selected from {-1, 1} (-1 for residential and 1 for commercial). Let WX+b=0 denote the line of separating class boundary (there are many possible boundaries), where W is the normal vector of the class boundary, consisting two attributes and b is a bias. Then W and b must satisfy

$$WX_i + b \geq 1 \text{, for } y_i=1 \tag{4}$$

$$WX_i + b \leq -1 \text{, for } y_i=-1 \tag{5}$$

Combining equations (4) and (5) will result

$$y_i(WX_i + b) \geq 1 \tag{6}$$

Under this constraint, the solution of the optimal separating boundary (the solid black line in Figure 6.2a) must maximize the margin, i.e. minimize the norm of w:

$$F(W) = \frac{\|W\|^2}{2} \tag{7}$$

However, as there are some spectrum overlaps between the residential and commercial pixels, it is well-known that residential and commercial pixels are often linearly separable (Figure 6.3b). In this case, a slack variable ξ_i is introduced. The slack variable ξ_i indicates the distance of a training pixel i from the corresponding line WX+b=1 or WX+b=-1. Thus, the constraints of W and b in equation (6) will be changed to:

$$y_i(WX_i + b) \geq 1 - \xi_i \tag{8}$$

Under this modified constraint, the solution of the optimal separating class boundary will be minimizing a cost function that takes both margin maximization and error minimization into account:

$$F(w) = \frac{\|W\|^2}{2} + c\sum_{i=1}^{n} \xi_i \tag{9}$$

where *c* is a penalty term to penalize the training pixels that are located on the wrong sides of the class boundaries. By combining equation (9) and the inequality constraint function (8), the objective of the optimization problem is to find the saddle point of this Lagrangian:

$$L = \frac{\|W\|^2}{2} + C\sum_{i=1}^{n} \xi_i - \sum_{i=1}^{n} \lambda_i (y_i (WX_i + b) - 1 + \xi_i) - \sum_{i=1}^{n} \mu_i \xi_i \tag{10}$$

The saddle point meets the following conditions:

$$W = \sum_{i=1}^{n} \lambda_i y_i x_i \tag{11}$$

$$\sum_{i=1}^{n} \lambda_i y_i = 0 \tag{12}$$

$$\lambda_i + \mu_i = C \tag{13}$$

By substituting equations (11), (12), and (13) into the Lagrangian (10), the optimization problem will be converted to a dual Lagrangian:

$$L_D = \sum_{i=1}^{n} \lambda_i - \frac{1}{2}\sum_{i,j=1}^{n} \lambda_i \lambda_j y_i y_j X_i X_j \tag{14}$$

This optimization problem can be solved by quadratic programming (Vapnik, 1998; 2000). The decision rule for a new instance X_j is:

$$f(w) = sign(WX_j + b) = sign(\sum_{i=1}^{r} \alpha_i y_i (X_i X_j) + b) \tag{15}$$

where $x_i = 1, 2 \ldots r$ are support vectors, α_i is a Lagrange multiplier, *sign*() means +/- sign.

Non-linear decision boundaries can be solved through a kernel trick. The input attribute space *R* is non-linearly mapped to a higher-dimensional space *H* through a certain function Φ(X), allowing the linear decision boundary to be found in the newly-mapped space *H*. It is not

necessary to know the exact form of Φ(x), so one can define a kernel function:

$$K(X_i, X_j) = \Phi(X_i)\Phi(X_j) \tag{16}$$

The expensive computation in the higher-dimension space can be simplified by substituting the kernel function into the decision rule and computing in the attribute space:

$$f(w) = sign(\sum_{i=1}^{r} \alpha_i y_i K(X_i X_j) + b) \tag{17}$$

The kernel function must meet Mercer's condition (Vapnik, 2000). Commonly used kernels include polynomial kernels, radial basis functions (RBF), and sigmoid functions. The radial basis function is:

$$K(X_i, X_j) = e^{-\gamma \left\| X_i - X_j \right\|^2} \tag{18}$$

The above example is a simplified remote sensing classification. In most classification approaches, multiple bands and multiple classes are involved. As band-related attributes are represented with vectors in above equations, the above mathematical approach still applies to the multi-band scenarios. Many remote sensing classifications involve more than two LULC categories. Multi-class classification is more complex than the previous simple binary problems with only residential and commercial classes. Common solutions include techniques such as the one-against-the-rest (Vapnik, 2000) and the one-against-one approach (Knerr et al., 1990). The one-against-the-rest approach constructs n-1 support vector machines to separate one class from the rest, and the class output determined by the SVM corresponds to the maximum margin from the instance to the decision boundary. The one-against-one approach constructs n(n-1)/2 support vector machines to separate each pair of classes, and a maximum-win voting procedure from all support vector machines is applied to determine the predicted class. According to recent research (Hsu and Lin, 2002; Pal and Mather, 2005), one-against-one is more accurate and efficient.

Two parameters need to be determined *a priori* in order to use SVM (for radius basis kernel): *c* and γ. These two parameters are not demonstrated in Figure 6.3. Basically, c is a parameter that penalizes classification errors and γ is a parameter that controls the shape of the RBF kernel function. *c* controls the location of the classification boundary and γ controls the shape of the non-linear boundary. Some approaches use the grid-search algorithm to determine these parameters (Yang et al., 2006). The grid-search algorithm first searches a coarser grids such as (0, 10, 20, 30, 40, 50) for γ candidates, then focuses on the portion (suppose it is 10-20) that has the best classification accuracy and narrow down to a higher precision (11, 12, 13, 14, 15 …), until a certain level is reached or the accuracy is stable. However, the problem with this method is that the distribution of classification accuracy surface is not mathematically known, one cannot guarantee that the best γ exists in a certain portion based on a coarser resolution (in other words, although γ=30 is worse than γ =10 and γ=20, for a finer grid, γ =15 may not be better than γ =25). Usually it involves extensive trial-and-error attempts to determine the best *c* and γ. In this research, a GA is favored to search for optimized parameters. GAs have been applied in the optimization of SVM parameters in previous studies (Bazi and Melgani, 2006). In this study, a GA is configured in the following form: the search space of C and γ were limited to four integer places and four decimal places, i.e. c and γ were encoded in the range of [0000.0000, 9999.9999]. A decimal encoding was used such that crossover and mutation operations occur on one of the 16 decimal genes. To avoid the common overfitting problem in non-linear classifiers, a threefold cross-validation was used. Fitness of a chromosome was determined by its cross-validation accuracy. As suggested in some previous research (Huang et al., 2002), one-against-one approach was better; therefore it is used in this research. As the lacunarity layer may have different minimum-maximum ranges for different spectral layers, it was scaled so that it will affect the

accuracy of SVMs. Fractal dimension layers and spatial autocorrelation layers are also scaled to have the same range as the spectral layers. The MATLAB programming interfaces of LibSVM (Chang and Lin, 2001) were used in this research to combine GA modules in a seamless and automatic way. A learning curve is presented in Figure 6.4.

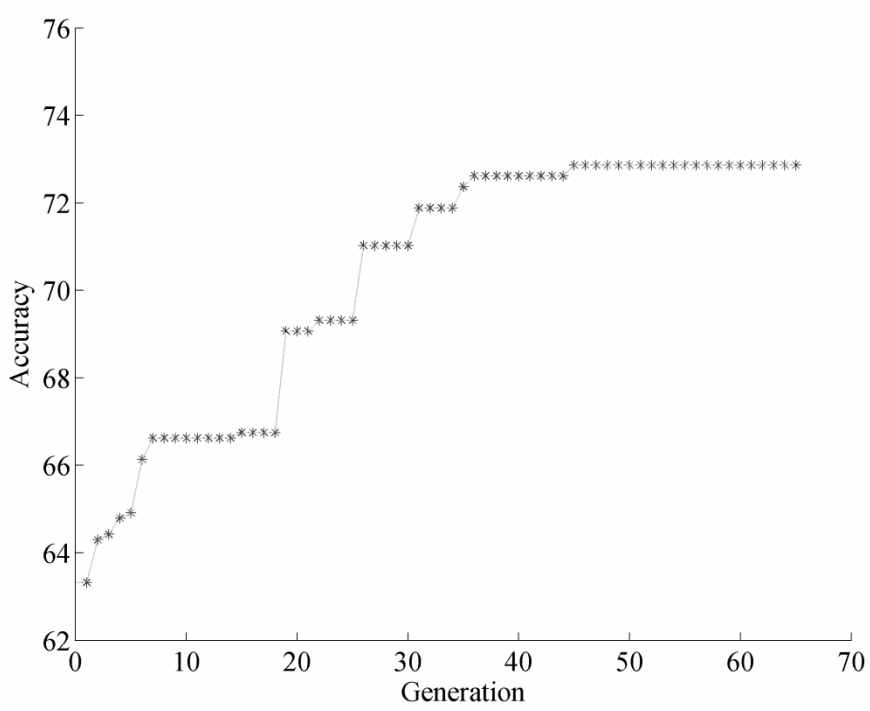

Figure 6.4 Training of GASVM with spectral and lacunarity bands on a small training set containing 800 pixles. The training time was 0.22 hour.

6.3 Experiment 1: Classifying Urban Land-Use/Land-Cover with IKONOS Image Mosaic

The first dataset used in this study is an image mosaic containing five land use categories (Figure 6.5) extracted from a post-Hurricane-Katrina IKONOS image of New Orleans: industrial/commercial complex (dominated by light manufacturing plants), low house density residential area, commercial area, flooded high house density residential area, and forest. The class ratio is perfect balanced and the overall size of the artificial mosaic is 175x1150 pixels.

Figure 6.5 IKONOS image mosaic. From left to right: Industrial/commercial complex, low house density residential area, commercial area, high house density residential area (flooded), and forest. Each subset contains 175x230 pixels. Displayed in band 4-3-2 false color composite. Image was taken on Sep.2, 2005, New Orleans, Louisiana.

The 4-meter resolution near-infrared, red, and green bands were used as spectral variables. Rather than compress the image into 8 bit, the original 11-bit image was used, because it has a sharper ground feature comparison and richer information. Lacunarity, fractal dimension, and Moran's *I* layers (Figure 6.6) were retrieved using a 33x33 (pixels) window from the principal component of the multi-spectral bands. Three textural bands were stacked with the three spectral bands such that each pixel can have a 6-dimensional spectral-textural vector.

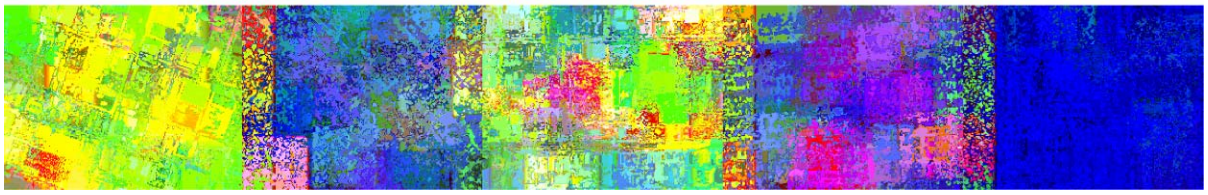

Figure 6.6 Composited textural bands (red: fractal dimension, green: Lacunarity, blue: Moran's *I*) derived from the principal component of IKONOS multispectral bands.

Training data was selected randomly and contained around 2000 pixels. In order to avoid a biased judgment based on one sample, 10 sets of training data were derived. All pixels in the entire image were used to calculate classification accuracy. Two sets of variables, spectral only and spectral-textural variables, were used as two sets of training data to compare the performance of supplying additional neighborhood spatial information. Different classification algorithms, GASVM, GBC, NNC, and MLC, were tested and compared. Considering the stochastic characteristics of GASVM, GBC, and NNC, each of them were run three times and the

best output was used in the comparison. For NNC, the number of input neurons was the number of bands used (3 or 6); the number of neurons in output layers was the number of classes (5); and the number of neurons in hidden layers ranged from one to three times as input bands (3-9 or 6-18). Threefold cross-validation was used for GBC and GASVM to prevent overfitting the training set. As suggested in previous literature (Demuth et al., 2008), Bayesian regularization was used for NNC to prevent overfitting.

6.3.1 Accuracy and Robustness

As shown in Table 6.1, clearly there is advantage of utilizing neighborhood spatial information in classification. Using a texture vector containing lacunarity, fractal dimension, and Moran's *I* information, in addition to the spectral reflectance information at the near-infrared, red, and green bands, resulted in improved overall and kappa accuracy regardless of the type of classifier. These improvements are significant using the Kappa statistic, reflected by the Kappa z values: 40.7 for TV-GBC to S-MLC, 83.0 for TV-NNC to S-MLC, and 78.6 for TV-GASVM to S-MLC), all exceeding the 0.05 significance level (z=1.96).

Table 6.1 Overall and Kappa accuracies of different classification approaches

Accuracy	S*-MLC	TV*-GBC	TV-NNC	TV-GASVM
Overall	80.5	85.04	89.52	90.08
Kappa	75.24	81.27	86.81	86.26

* S denotes spectral-based approach without textural bands; TV denotes texture vector-aided approach with both spectral and textural bands.

In comparison to the per-pixel MLC, using texture vector-aided classification with GBC, GASVM, or NNC can further increase the overall and kappa classification accuracy, as demonstrated in Figure 6.7.

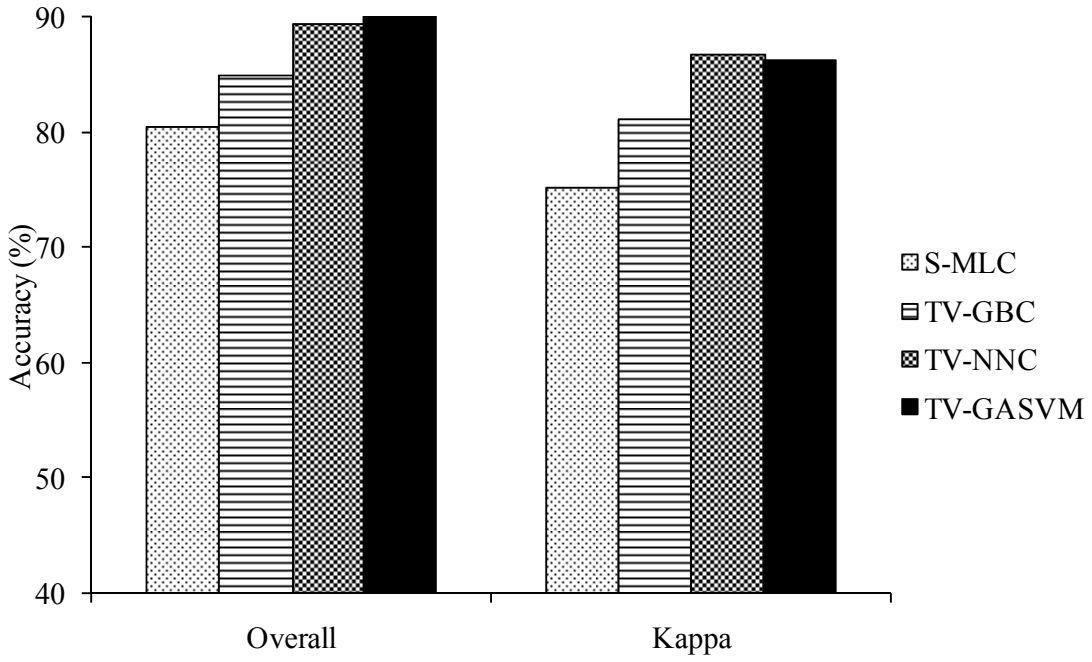

Figure 6.7 Mean overall and kappa accuracy of different classification approaches. S- stands for spectral-based approach, TV- stands for texture vector-aided approach. S-MLC serves as a baseline.

From the baseline accuracy of 80.5%, a 5% increase was determined with texture vector-aided GBC classification and a 10% increase was determined with the texture vector-aided GASVM and NNC classification approach. As GBC is basically a modified MLC with prior parameters optimized by GAs, the decision boundary locations are restricted by the normal curves. Therefore GBC is not able to locate more complex and accurate decision boundaries such as non-parametric GASVM and NNC. Accuracy improvements made by the combination of texture vector and advanced classifiers are illustrated using the classified images (Figure 6.8).

In the previous discussion, only the overall accuracy was mentioned; however, there are two other important accuracy measures: commission errors and omission errors. Although the use of probabilities with MLC may lead to better overall accuracy, it does not guarantee better accuracy for all classes (Zheng et al., 2005). A detailed comparison of the classifiers involved in this series of experiment is provided in Figure 6.9.

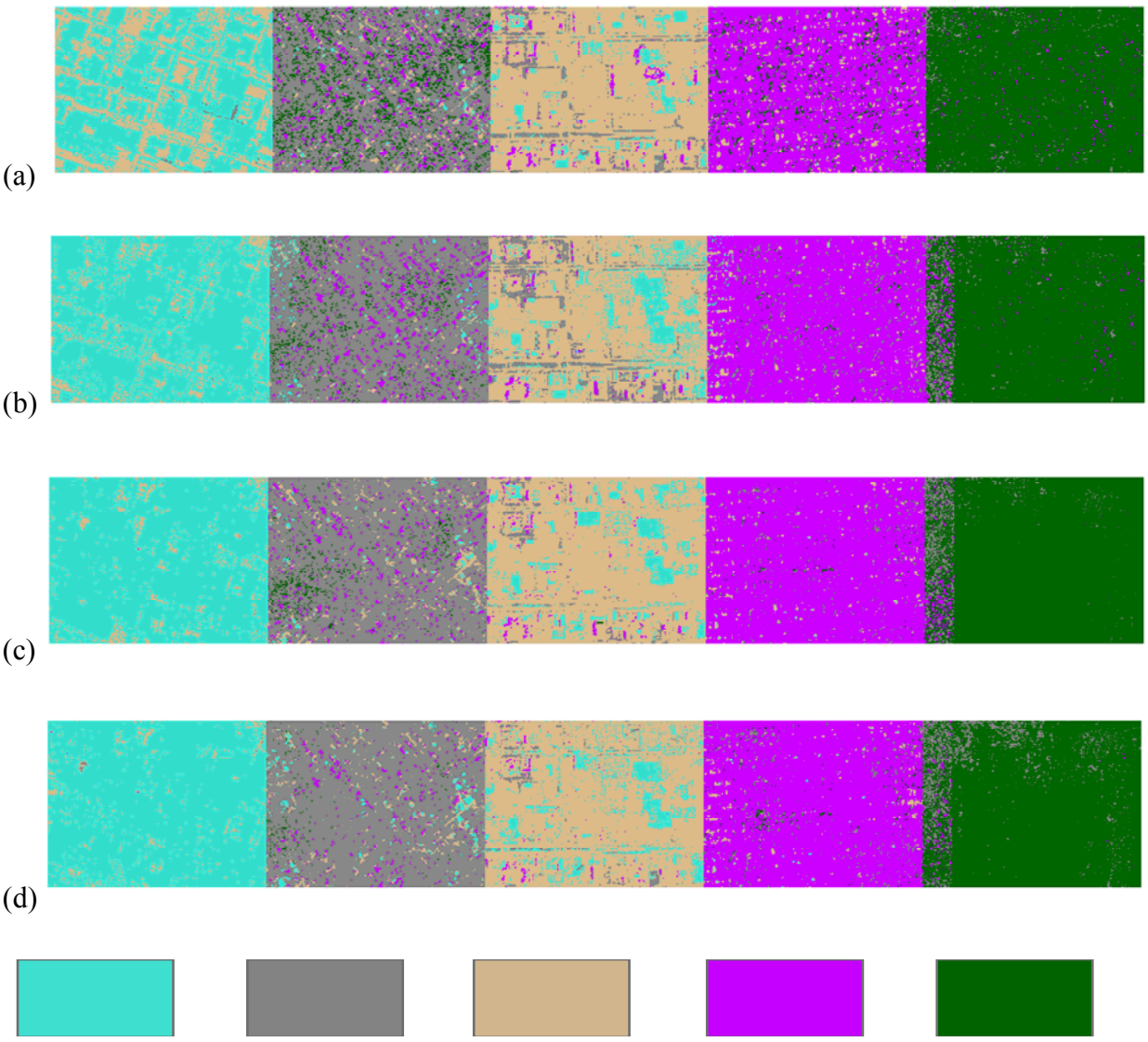

Figure 6.8 Classification results from different approaches. (a) traditional spectral-based classification with MLC; (b) texture vector-aided classification using GBC; (c) texture vector-aided classification using NNC; (d) texture vector-aided classification using GASVM.

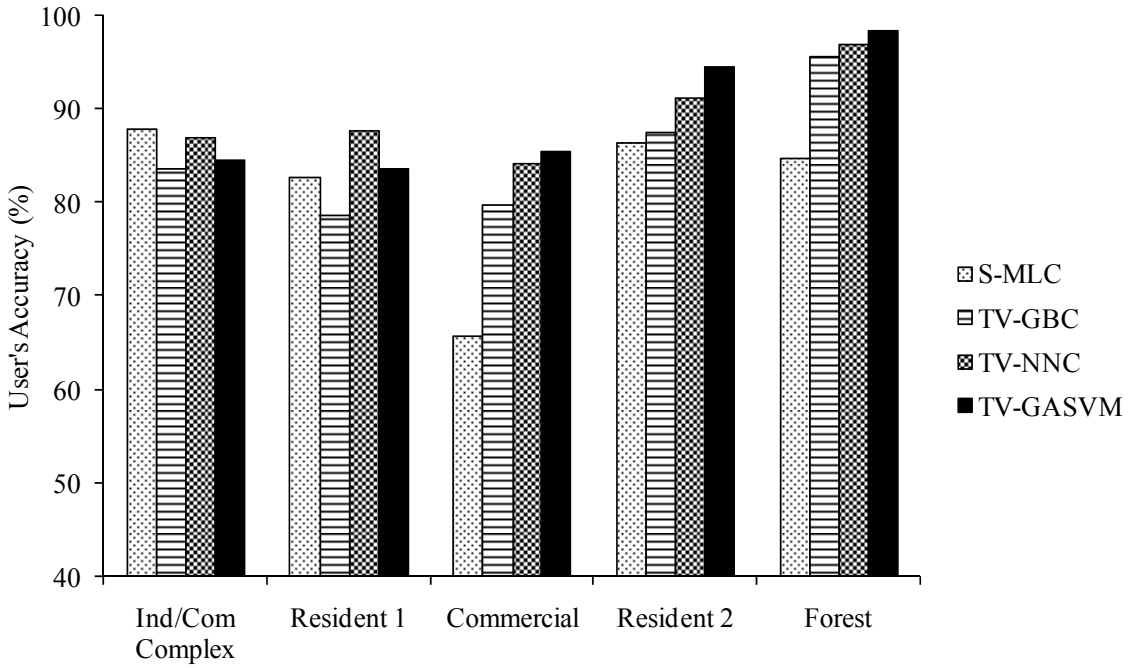

(a)

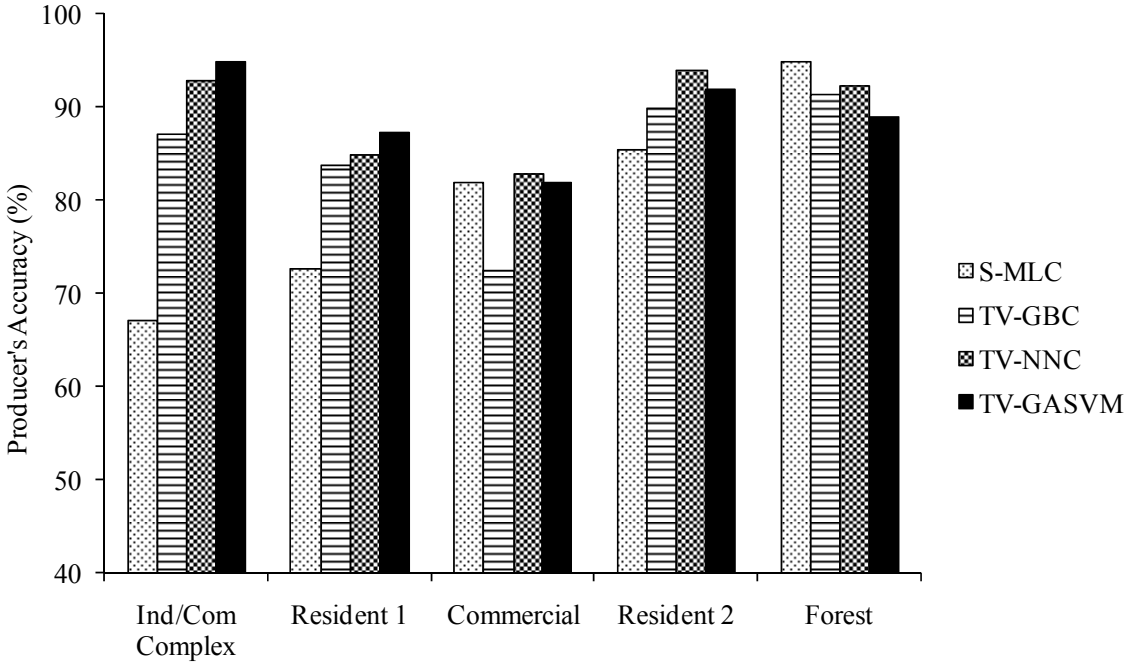

(b)

Figure 6.9 A detailed accuracy comparison of different land use categories from different classification approaches. (a) user's accuracy; (b) producer's accuracy. S- stands for spectral-based approach, TV- stands for texture vector-aided approach. S-MLC serves as a baseline.

Results shown in Figure 6.9 are from the same training data with spectral-textural information used for GBC, NNC, and GASVM. Results from the spectral-based MLC were also provided as a baseline. Using texture vector-aided approach with advanced classifiers can lead to an improvement for most classes as seen in Figure 6.9, compared to the baseline of spectral-based MLC approach. In regard to the three texture vector-aided approaches, NNC and GASVM were better than GBC for most classes. GASVM was slightly better than NNC for the user's accuracy of commercial, residential type 2, and forest, but were less accurate than NNC for the producer's accuracy of these three classes.

Based on classifications from ten different training sets, the standard deviation was measured for each classifier (Table 6.2). GASVM has the greatest variation. One possible reason could be that different c (penalization parameter) and γ (kernel parameter) parameters are generated by using the GA at different runs. GBC, GASVM, and NNC have better accuracies than MLC in each of the ten experiments with different training sets. GASVM and NNC are all better than GBC in the ten experiments. Meanwhile, GASVM and NNC are very similar in all ten scenarios without significant difference.

Table 6.2 Standard deviation of the overall accuracies derived from ten different training sets

S*-MLC	TV*-GBC	TV-NNC	TV-GASVM
0.60	0.56	0.35	0.66

* S denotes spectral-based approach without textural bands; TV denotes texture vector-aided approach with both spectral and textural bands.

6.3.2 Computational Efficiency

(1) Efficiency of calculating lacunarity, fractal dimension, and Moran's I layers

In this experiment, for the 4-meter resolution 175x1150 IKONOS image, at a 33x33 pixels window, the computational cost on a Sun Microstation (CPU: 2.41GHz, RAM: 4GB) was 35, 77, and 50 seconds for lacunarity, fractal dimension, and spatial autocorrelation Moran's *I*, respectively. For lacunarity and Moran's *I* calculation, the processing time will increase when a larger window is used. For fractal dimension, the processing time depends more on the number of available steps used to construct triangular prisms.

(2) Computational cost of different classifiers

MLC was the least accurate but most computationally efficient method. Training MLC was simply done by calculating the covariance matrices for discriminant functions and can be done in just a few seconds, even for a large training dataset. GBC uses GAs to search for the optimized solution of prior parameters, and was found quite efficient because the discriminant functions were fixed.

SVM (radial basis kernel) have two parameters. Derivation of support vectors varies dramatically when the magnitude of parameter *c* (penalization parameter) and γ (kernel parameter) are changed. As there is no common guideline for choosing appropriate values for *c* and γ; inappropriate parameters may lead to very low classification accuracy. Some search algorithms such as grid search (Chang and Lin, 2001; Yang et al., 2006) or GA search (Bazi and Melgani, 2006; Pal, 2006) are necessary. Because support vectors need to be recalculated for each possible solution of *c* and γ, even with an efficient GA, it often takes considerable time to train, as revealed in this research. The size of the training set also impact the training time. As the size increases, the training time may grow quickly.

Training of NNC is well-known to be a time-consuming process. Although different configurations or empirical rules were tried or compared in previous research (Huang et al., 2002; Kavzoglu and Mather, 2003; Mills et al., 2006), there is no undeniable universal solution. Increasing the sample size may increase the training time. Therefore, a more complex network structure could be rather time-consuming.

Figure 6.10 provides an illustration of computational cost for different classifiers. For GBC and GASVM, same GA parameter settings and termination criteria (no accuracy change in 20 generations) were used and the average evolved generations were both near 45. For NNC, the training stage involved a comparison among three different hidden layer settings: one, two, and three times of input variables. GBC (3.7 seconds) was much more efficient than GASVM and NNC. It should be noticed that the training set only contained a small amount of pixels (2000). In most classification scenarios, a number of selected sites are often used as the training data, which contain a much larger amount of pixels than this research. GASVM and NNC would be very time-consuming for a large training set.

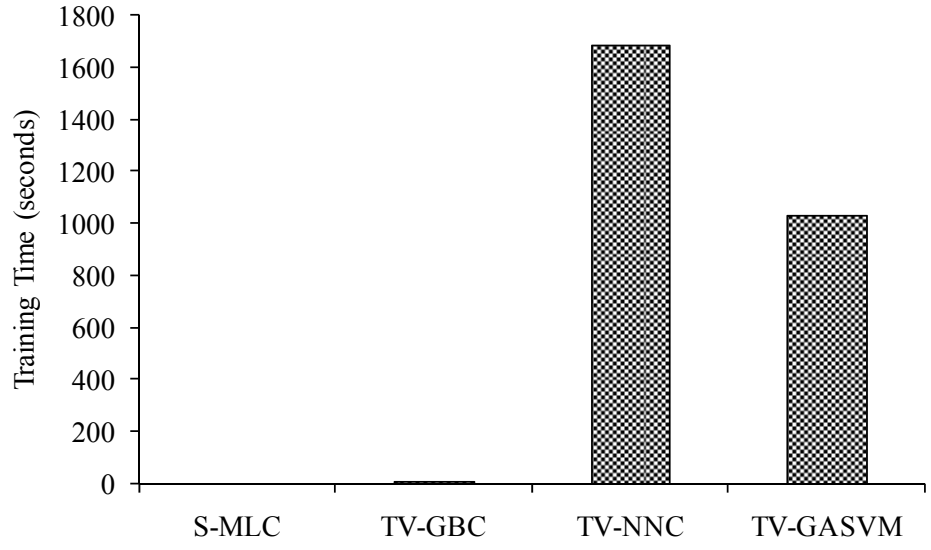

Figure 6.10 Average training time of different classifiers. S- stands for spectral-based approach, TV- stands for texture vector-aided approach. S-MLC serves as a baseline.

6.3.3 Stochastic Characteristics of GBC, GASVM, and NNC

The use of GBC, GASVM, and NNC require a number of initial parameters to be set randomly. The use of GAs to search optimal parameters of GBC and GASVM involves a randomized initial population, randomized crossover or mutation position, arbitrary population size, and crossover and mutation rates. The weight vectors and biases of NNC are often generated randomly, and the number of hidden layers and neurons are established by the user. These randomized parameters, along with some user-defined settings, could make different runs yield different classification accuracies. To partially correct the bias resulted from just one time training, three runs with different initial parameter settings may help to identify the best result, as proposed by Armstrong et al. (2003); this approach was taken in this research. Thus, the actual training time used is increased by a factor of three compared to those in Figure 6.10.

6.4 Experiment 2: Discriminating Urban Residential Neighborhoods with Different Economic and Hurricane Impact Statuses

Remote sensing data has been increasingly used in to perform socio-economic analysis. Yuan et al. (1997) performed multivariate regression analysis between census population and land cover types derived from Landsat TM data and used the result to remodel population in greater spatial details. Beck et al. (2000) reviewed the use of different sensors to analyze the spatial and temporal patterns of disease mapping. Zhou (2006) used aerial photographs to classify different urban residential neighborhoods with different levels of income.

An important application of remote sensing data was also extensively used for disaster monitoring and analysis (Kerle et al., 2003; Tralli et al., 2005). The study area, New Orleans was inundated on August 29, 2005 by Hurricane Katrina. Many residential neighborhoods were flooded. In this experiment, four neighborhoods (River Ridge, Metairie, Hollygrove, and Algiers) with distinct economic/environmental statuses were selected (Figure 6.11). An IKONOS image

that was taken on September 2, 2005 was used to discriminate these four residential neighborhoods. Textural indices (fractal dimension, lacunarity and Moran's *I*) were used to describe the textural images (Figure 6.12-6.15). Each neighborhood image covers one or more census blockgroups. The income and hurricane impact status of the four neighborhoods are listed in Table 6.3. Median income data was derived by tabulating 2000 census blockgroups.

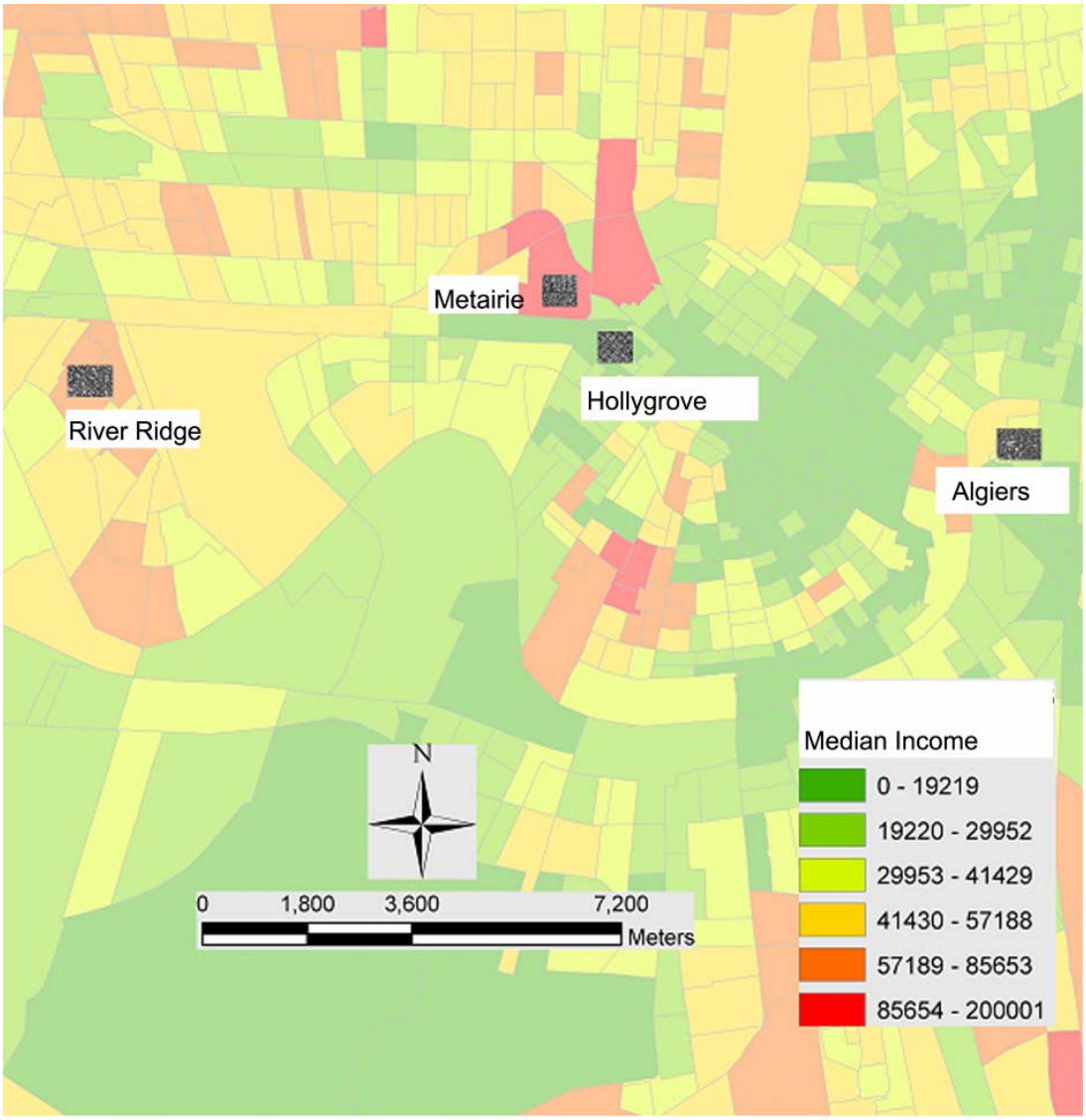

Figure 6.11 Distribution of selected urban residential neighborhoods (background polygons are census blockgroups).

Figure 6.12 The neighborhood of Algiers in Orleans Parish, Louisiana. Image is displayed using the IKONOS panchromatic band (Sep. 2, 2005). Size: 772x542 pixels.

Figure 6.13 The neighborhood of Hollygrove in Orleans Parish, Louisiana. Image is displayed using the IKONOS panchromatic band (Sep. 2, 2005). Size: 602x542 pixels.

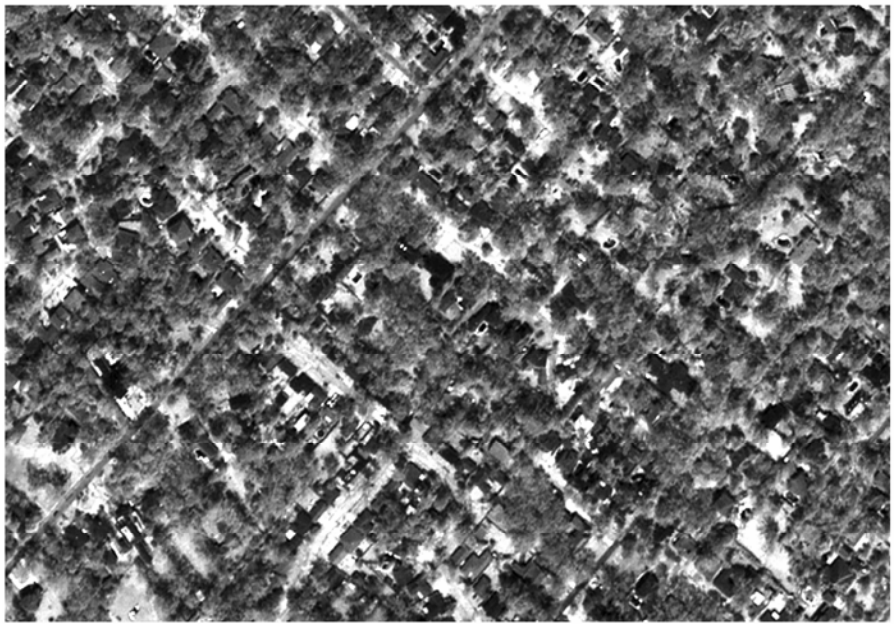

Figure 6.14 The neighborhood of River Ridge in Jefferson Parish, Louisiana. Image is displayed using the IKONOS panchromatic band (Sep. 2, 2005). Size: 772x542 pixels.

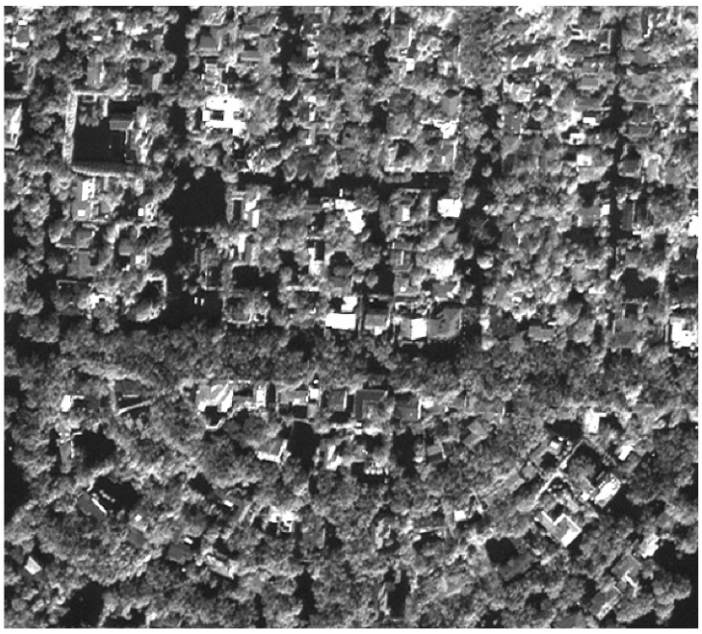

Figure 6.15 Metairie neighborhood in Jefferson Parish, Louisiana. Image is displayed using the IKONOS panchromatic band (Sep. 2, 2005). Size: 602x542 pixels.

Table 6.3 Income and hurricane impact status of four residential neighborhoods

Neighborhood	Median Income ($, year 2000)	Hurricane impacts	Subset size (m)
River Ridge	High: 79,347	Not flooded	772x542
Metairie	High: 88,604	Flooded	602x542
Hollygrove	Low: 17,026	Severely Flooded	602x542
Algiers	Low: 25,391	Not Flooded	772x542

Fractal dimension, lacunarity, and spatial autocorrelation texture layers were derived using the panchromatic band, under a 65x65 pixels (meters) window, the most appropriate window size determined in Chapter 5. Pixels located near the edge of each subset were processed using a mirror extension method (Myint et al., 2006). Spectral information from the green, red, and near-infrared components of the IKONOS multispectral bands were used, together with three downsampled textural bands, for neighborhood classification. Simple mean value is used in the downsampling process from 1 meter to 4 meter resolution. From the stacked spectral-textural images, a random sample of 4,500 pixels was used for training and another random sample of 4,612 pixels was used for accuracy assessment. Training data and assessment data did not overlap each other. For GBC, NNC, and GASVM, three runs were performed to select the best parameters for classification.

6.4.1 Descriptive Statistics of Different Urban Residential Neighborhoods

The descriptive statistics for the four selected residential neighborhoods are listed in Table 6.4. It can be seen that all neighborhoods have a wide range of spectral values and overlapped with each other, hence it is not easy to separate them by using only spectral information. Adding additional textural variables would improve the results. Flood impacts are obvious in band 4, as water absorbs more near-infrared energy and reduce mean DN values of flooded neighborhoods.

Table 6.4 Descriptive statistics regarding urban residential neighborhoods with different economic/environmental status

Band	Neighborhood	Min	Max	Mean	SD	CV
Band4	River Ridge (HI)	217	973	494	119	0.24
	Algiers (LI)	158	996	399	118	0.30
	Metairie (HI, F)	120	958	317	100	0.32
	Hollygrove (LI, F)	107	602	220	81	0.37
Band3	River Ridge (HI)	205	674	272	52	0.19
	Algiers (LI)	195	1040	322	80	0.25
	Metairie (HI, F)	180	1022	228	49	0.21
	Hollygrove (LI, F)	170	537	233	48	0.21
Band2	River Ridge (HI)	349	699	158	41	0.26
	Algiers (LI)	340	1124	431	70	0.16
	Metairie (HI, F)	322	1102	486	44	0.09
	Hollygrove (LI, F)	311	664	696	38	0.05

HI: high income; LI: low income, F: flooded

6.4.2 Classifying Residential Neighborhoods with Different Methods

Classification results are listed in Table 6.5. A large increase in accuracy was resulted using the integrated approach, from 62.7% of per-pixel MLC to 70.8%, 76.9%, 75.6% of texture vector-aided approach with GBC, NNC, and GASVM respectively (Figure 6.16). These improvements are significant based Kappa statistic z values: 8.1 for TV-GBC to S-MLC, 14.7 for TV-NNC to S-MLC, and 13.4 for TV-GASVM to S-MLC); all of them exceeded the 0.05 significance level (z=1.96).

Table 6.5 Overall and Kappa accuracies of different classification approaches

Accuracy	S*-MLC	TV*-GBC	TV-NNC	TV-GASVM
Overall	62.66	70.75	76.86	75.58
Kappa	50.31	60.81	68.9	67.24

* S denotes spectral-based approach without textural bands; TV denotes texture vector-aided approach with both spectral and textural bands.

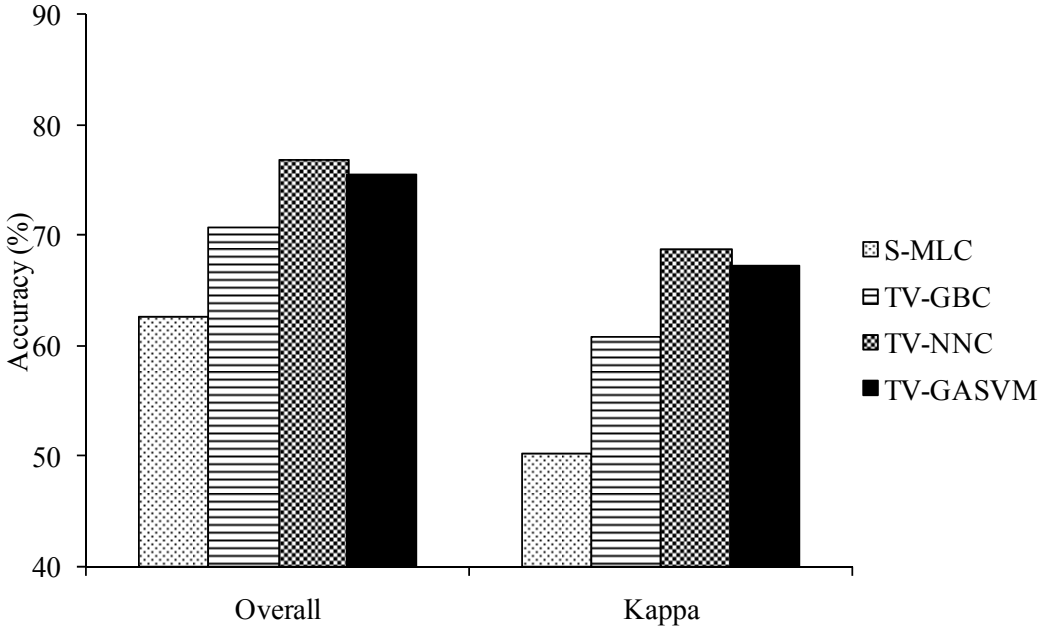

Figure 6.16 Overall accuracies and kappa accuracies of different classification approaches.

6.4.3 Detailed Analysis with Confusion Matrices

The confusion matrices are listed in Table 6.6-6.9. Compared to the traditional per-pixel MLC approach, with few exceptions, both user's and producer's accuracies were increased with texture vector-aided classification and all three artificial intelligence classifiers. An improvement with GASVM over GBC can also be found in most neighborhoods, but with some exceptions. In general, the errors for River Ridge neighborhood to be misclassified into the Hollygrove neighborhood and vice versa were lowest, because these two neighborhoods were dramatically different from each other in terms of their economic/environmental statuses.

Table 6.6 Confusion matrix of neighborhood classification by using spectral-based maximum likelihood classification

C* / R*	River Ridge (HI)	Algiers (LI)	Metairie (HI, F)	Hollygrove (LI, F)	Producer's (%)
River Ridge	897	148	218	47	68.47
Algiers	255	631	166	212	49.92
Metairie	99	70	562	309	54.04
Hollygrove	13	74	111	800	80.16
User's(%)	70.97	68.36	53.17	58.48	62.66

(R*: Reference data, C*: Classified results)

Table 6.7 Confusion matrix of neighborhood classification by using texture vector- aided classification with the Genetic Bayesian classifier

C* / R*	River Ridge (HI)	Algiers (LI)	Metairie (HI, F)	Hollygrove (LI, F)	Producer's (%)
River Ridge	927	201	171	11	70.76
Algiers	147	920	119	78	72.78
Metairie	101	134	724	81	69.62
Hollygrove	3	168	135	692	69.34
User's(%)	78.69	64.65	63.01	80.28	70.75

(R*: Reference data, C*: Classified results)

Table 6.8 Confusion matrix of neighborhood classification by using texture vector- aided classification with neural network classifier

C* / R*	River Ridge (HI)	Algiers (LI)	Metairie (HI, F)	Hollygrove (LI, F)	Producer's (%)
River Ridge	1056	191	55	8	80.61
Algiers	163	1009	22	70	79.83
Metairie	93	154	712	81	68.46
Hollygrove	4	134	92	768	76.95
User's(%)	80.24	67.81	80.82	82.85	76.86

(R*: Reference data, C*: Classified results)

Table 6.9 Confusion matrix of neighborhood classification by using texture vector- aided classification with support vector machines classifier

C* / R*	River Ridge (HI)	Algiers (LI)	Metairie (HI, F)	Hollygrove (LI, F)	Producer's (%)
River Ridge	1036	192	69	13	79.08
Algiers	178	942	54	90	74.53
Metairie	109	120	728	83	70.00
Hollygrove	3	111	104	780	78.16
User's(%)	78.13	69.01	76.23	80.75	75.59

(R*: Reference data, C*: Classified results)

Neighborhoods that have the same economic statuses can be merged so binary classification accuracy (high/low income) can be derived from the new confusion matrices. Similarly, a binary classification based on Hurricane Katrina impact statuses (flooded/non-flooded) can be also derived. The overall accuracies are listed in Table 6.10. For all classification methods, flooded/non-flooded classification scheme has a better accuracy than high/low income, implying that Hurricane Katrina impact status can be easier distinguished than economic status.

Table 6.10 Overall and Kappa accuracies of different classification approaches.

Binary scheme	S-MLC	TV-GBC	TV-NNC	TV-GASVM
High/low income	75.7	82.0	84.5	83.8
Flooded/non-flooded	80.1	83.2	88.4	87.7

6.4.4 Limitations of This Example

In fact, using census variables such as income can better differentiate these four different neighborhoods. However, the downside is that current census data is on a 10-year basis. Remote sensing data provide much quicker revisit to the same area, thus provide the capability of tracking detailed neighborhood changes. From this point of view, associating texture patterns with the socioeconomic statuses of residential neighborhoods could be promising.

As observed in the above example, flooding statuses complicated the social-economic status discrimination. In contrast to Hurricane Katrina impact, which is only special to this research area and flooding status can usually be easily detected, socioeconomic status is more generic to a wide range of area. As demonstrated in this example, texture analysis can be well-suited to identify the relative social-economic status; however, the achieved accuracy is still at a low level (<85%), in contrast to 93% accuracy in a research with 1-foot aerial photograph by Zhou (2006).

Future research could use even higher resolution remote sensor imagery to do more detailed analysis, such that image texture patterns of residential neighborhoods can be quantitatively socialized.

6.5 Comparison among GBC, NNC, and GASVM: Sampling Issues

The improvement of using GAs to optimize prior parameters of MLC is due to two adjustments. The first one is to adjusting prior probabilities to fit class proportions of the study area, as was done in Chapter 5 with an urban IKONOS subset that has unbalanced land use proportions. Another adjustment is to further adjust class boundary through changing prior probabilities even with balanced class proportions, as demonstrated in this chapter. Experiments showed that NNC and GASVM performed better than GBC for the dataset with balanced class proportions (this chapter) but there was no significant difference for the dataset with unbalanced proportions (Chapter 5). As class boundary candidates are bounded by the rigorous discriminant function, GBC is unable to search every possible class boundary like NNC and GASVM. By searching a wide range of boundaries, NNC and GASVM could lead to better accuracies as shown in this chapter, but require more computation cost and human-computer interaction.

Regarding sampling methods for remote sensing classifications, a common practice is to arbitrarily designate the training area with known LULC classes instead of randomly sampling some points and then judging classes. To achieve the best performance when using GBC, NNC, or GASVM, training samples should be representative in two aspects: the statistical distribution for each class and class proportions. For traditional MLC, only the covariance matrices are derived from the training data. Thus only the statistical distribution aspect is concerned. For GBC, NNC, and GASVM methods, not only is the statistical distribution for each class important, but also the class proportion, because the training performance measures such as

accuracy or sum of square errors are all tied to class proportions (as accuracy for each class is different). Another interpretation, MLC has a fixed class boundary and only takes statistical distribution into consideration; thus, it only requires that the training sample is statistically representative. GBC, NNC, and GASVM all employ training processes to better fit the training data and then deploy the best-fit model (training data) into the entire image, thus requiring the training data to be representative in terms of both statistics and class proportions. A recent research (Huang et al., 2002) reported that equal sample rate was a better sampling method than equal sample size for both NNC and SVM; which corresponds to the requirement of both class proportion and statistical distribution.

6.6 Conclusions

In this research, the performance of integrating a texture vector (fractal dimension, lacunarity, Moran's *I*) with advanced artificial intelligence classifiers (genetic Bayesian classifier (GBC), neural network classifier (NNC), and genetic algorithm – support vector machines (GA-SVM)) for classification was investigated using two experiments. The first experiment was the classification of an IKONOS image mosaic containing five LULC classes: commercial, industrial/commercial complex, residential, forest, and flooded residential area (due to Hurricane Katrina). The second experiment was to discriminate four different urban residential neighborhoods with different economic/environmental statuses: high/low income, flooded/non-flooded following the passage of Hurricane Katrina.

In the first experiment, textural measurements were extracted from the principal component band (following chapter 4) of the image mosaic. Three textural bands were stacked with three original multispectral bands. Training stages were then carried out with ten different random sample datasets. Results showed that the integration of both texture vector methods and artificial

intelligence classifiers significantly improved overall classification accuracy by 5-10%. With per pixel MLC as a reference, the texture vector-aided approach with GBC can increase accuracy to 85.0% with a very low computational cost, while the texture vector-aided approach with GASVM and NNC provide more accurate classification results (90.1% and 89.5% respectively) but sacrifice computational efficiency greatly. In the second experiment that tested the ability to distinguish four urban residential neighborhoods, textural bands were derived from the panchromatic band (following Chapter 5) and downsampled to be compatible with the resolution of multispectral bands (green, red, and near-infrared). Results show that with the integration of texture vector and advanced classifiers, residential neighborhoods with distinct economic/environmental status were better discriminated: 8-14% increase compared to the 62.6% with per-pixel MLC. The non-flooded high-income residential neighborhood and the flooded low-income residential neighborhoods were better classified than the rest.

NNC and GASVM yielded better accuracies than GBC in both experiments. As the location of the decision boundary is bounded by the normal curves, GBC is not able to search for other boundaries such as NNC and GASVM. By searching a wide range of boundaries, NNC and GASVM could lead to better accuracies, but with increased computation cost and human-computer interaction.

Chapter 7
Summary

High-resolution satellite imagery brings urban remote sensing to a new era by providing greatly improved ground feature interpretability. Urban land-use/land-cover (LULC) classification is facing a great challenge; on one hand to take advantage of the improved ground feature interpretability, and on the other hand to overcome the increased in-class heterogeneity and among-class overlap. This dissertation investigated two major approaches in recent literature, texture analysis and artificial intelligence classifiers, and demonstrated a promising avenue of integrating these two directions together to accomplish the goal of classifying urban LULC from high-resolution IKONOS imagery more efficiently and accurately.

Specifically, the research objectives include: (1) to develop more efficient algorithms of calculating local fractal dimension; (2) to evaluate and determinate the best lacunarity estimator; (3) to determine the effects of window size for local fractal dimension, lacunarity, and Moran's *I*, using IKONOS imagery; (4) to develop a genetic Bayesian classifier (GBC) to improve the classification performance of the traditional maximum likelihood classifier (MLC) by optimizing the prior probabilities; (5) to determine the effectiveness of integrating texture analysis and the proposed GBC in classifying heterogeneous urban area and identifying different residential neighborhoods with different economic/environmental statuses. The underlying hypothesis of this dissertation is: integrating the texture vector-aided approach with artificial intelligence classifiers can improve urban LULC accuracy.

7.1 Summary of Findings

(1) For Objective 1--to resolve the pixel coverage problem of local fractal triangular prism implementation--the divisor-step method was developed. The new method guarantees 100% effective coverage ratio on the local square window. It was compared with the arithmetic-step

and two variants of the geometric-step methods, using 4,000 computer simulated fractal surfaces and IKONOS images. The proposed divisor-step method was found to yield the lowest overall RMSE and was most accurate for highly complex surfaces (e.g. fractal dimensions of 2.7 and 2.9). Hence, the method is more suitable for complex urban satellite image characterization.

(2) On the research of lacunarity estimator, a new method based on the gliding-box algorithm and the fractal triangular prism method was developed. The new method was compared with two existing methods in IKONOS image classification, including the probabilistic box counting method and the differential box counting method. The new method yielded better classification accuracies and was more efficient computationally.

(3) On the issue of window size effects on texture-aided classification approach, the results suggested that fractal dimension aided approach was stable across different window sizes, whereas lacunarity, Moran's *I*, and the composite texture vector-aided approaches exhibited an accuracy increasing phase followed by a stable stage and a slightly decreasing phase thereafter. Based on the findings, the following windows for 4-m multispectral bands were recommended: 17x17 to 27x27 pixels for fractal dimension, 29x29 to 41x41 pixels for lacunarity, 33x33 to 41x41 pixels for Moran's *I*, and 27x27 to 37x37 pixels for the texture vector-aided approach. Window size effects on classification accuracy were found closely related to the land use object size. Other factors affecting accuracy can include algorithm effects and edge effects.

On the performance of texture-aided classification, the results showed that lacunarity was 3-16% better than Moran's *I* and fractal dimension. The texture vector-aided approach was 8-18% or 16-19% better than spectral-based approach, or 2-16% better than using individual textural index, with the same MLC.

(4) On the research of improving the traditional MLC method, an optimization approach with genetic algorithm was developed. The GBC significantly improved the overall accuracy, a 10% increase over the traditional MLC method, by using the spectral-based approach.

(5) On the performance of integrating texture analysis techniques with artificial intelligence classifiers, the proposed integrated approach greatly improved classification accuracy (17-21% for an urban IKONOS subset and 5-10% for an IKONOS image mosaic), compared with the baseline per-pixel MLC approach. The improvement was statistically significant and thus validated the hypothesis of the dissertation that this integrated approach can improve classification accuracy. In terms of classification accuracy, the GBC could achieve similar accuracy as neural network classifier (NNC) for a natural IKONOS subset with unequal land use proportion, but it was less accurate than the NNC and the genetic algorithm-support vector machines (GASVM) for an image mosaic with equal land use proportion. However, the GBC outperformed the other two artificial intelligence classifier dramatically in terms of computational cost.

The performance of using the integrated approach to discriminate urban residential neighborhoods with different economic statuses and impacts from Hurricane Katrina was evaluated using four neighborhoods extracted from post-Katrina IKONOS imagery in New Orleans, Compared with the 62.6% overall accuracy with the per-pixel MLC, the integration of a texture vector and artificial intelligence classifiers led to a 8-14% increase in accuracy.

7.2 Future Research

In general, the research is based on different subsets of one image. To generalize the findings, more study images will need to be experimented in future research.

Specifically, for local fractal dimension algorithms, this research found that the triangular prism method tends to have a slight overestimation for highly complex surfaces and a slight underestimation for medium or low surfaces. This is in agreement with previous research (Lam et al., 2002; Zhou and Lam, 2005). Further improvement is needed to overcome this problem.

For lacunarity algorithms, through both empirical IKONOS data and computer simulated fractals, this study found that for the same series of images, different algorithms (PBC, DBC, TP) disagree on the rank of "gappiness". Pendleton et al. (2005) reported a similar problem for the binary lacunarity estimators. Further investigation should be made to make a best recommendation for both binary and gray-scale estimators.

On the effects of window size on texture-aided approach, this dissertation only focused on IKONOS imagery at the 4-m multispectral, plus limited experiments on the 1-m panchromatic band. With only a few previous studies on the window size effects, further investigation on how window size effects can be related with a wide range of spatial resolutions (from high resolution at meter level all the way to low resolution at kilometers level) is necessary. In addition, the association between window size effects and land use object size can be further explored.

There is an increasing interest in the object-based approach in remote sensing community. The texture indices used in this research (fractal dimension, lacunarity, spatial autocorrelation) have a potential to be integrated into the object-based approach (as a parameter in both segmentation and classification stages), and artificial intelligence classifiers can also be applied to the classification stage of the object-based approach. More efforts need to be made toward the ultimate goal of LULC classification and change detection research, which is to improve accuracy, enable generalization, and reduce human supervision and computational cost.

References

Al-Khudhairy, D.H.A., Caravaggi, I. and Glada, S., 2005. Structural damage assessments from IKONOS data using change detection, object-oriented segmentation, and classification techniques. *Photogrammetric Engineering and Remote Sensing*, 71(7): 825-837.

Allain, C. and Cloitre, M., 1991. Characterizing the lacunarity of random and deterministic fractal sets. *Physical Review A*, 44(6): 3552-3558.

Anderson, J.R., Hardy, E.E., Roach, J.T. and Witmer, R.E., 1976. *A Land Use and Land Cover Classification System for Use with Remote Sensor Data*. U.S. Geological Survey, U.S. Government Printing Office, Washington, 28 pp.

Armstrong, M.P., Xiao, N.C. and Bennett, D.A., 2003. Using genetic algorithms to create multicriteria class intervals for choropleth maps. *Annals of the Association of American Geographers*, 93(3): 595-623.

Bagan, H., Wang, Q.X., Watanabe, M., Yang, Y.H. and Ma, J.W., 2005. Land cover classification from MODIS EVI times-series data using SOM neural network. *International Journal of Remote Sensing*, 26(22): 4999-5012.

Bazi, Y. and Melgani, F., 2006. Toward an optimal SVM classification system for hyperspectral remote sensing images. *IEEE Transactions on Geoscience and Remote Sensing*, 44(11): 3374-3385.

Beck, L.R., Lobitz, B.M. and Wood, B.L., 2000. Remote sensing and human health: New sensors and new opportunities, *Emerging Infectious Diseases*, 6(3): 217-226.

Binaghi, E., Brivio, P.A., Ghezzi, P. and Rampini, A., 1999. A fuzzy set-based accuracy assessment of soft classification. *Pattern Recognition Letters*, 20(9): 935-948.

Brodatz, P., 1966. *Texture: A Photographic Album for Artists and Designers,* Dover, New York, 128 pp.

Carr, J.R. and de Miranda, F.P., 1998. The semivariogram in comparison to the co-occurrence matrix for classification of image texture. *IEEE Transactions on Geoscience and Remote Sensing*, 36(6): 1945-1952.

Chang, C.C. and Lin, C.J., 2001. LIBSVM: A library for support vector machines. Available online at: http://www.csie.ntu.edu.tw/~cjlin/libsvm (accessed on Nov.20 2007).

Chen, D., Stow, D.A. and Gong, P., 2004. Examining the effect of spatial resolution and texture window size on classification accuracy: an urban environment case. *International Journal of Remote Sensing*, 25(11): 2177-2192.

Chubey, M.S., Franklin, S.E. and Wulder, M.A., 2006. Object-based analysis of IKONOS-2 imagery for extraction of forest inventory parameters. *Photogrammetric Engineering and Remote Sensing*, 72(4): 383-394.

Chust, G., Ducrot, D. and Pretus, J.L., 2004. Land cover mapping with patch-derived landscape indices. *Landscape and Urban Planning*, 69(4): 437-449.

Clarke, K.C., 1986. Computation of the fractal dimension of topographic surfaces using the triangular prism surface-area method. *Computers and Geosciences*, 12(5): 713-722.

Cliff, A.D. and Ord, J.K., 1973. *Spatial Autocorrelation*. Pion, London, 178 pp.

Cufi, X., Munoz, X., Freixenet, J. and Marti, J., 2002. A review of image segmentation techniques integrating region and boundary information. *Advances in Imaging and Electron Physics,* 120: 1-39.

Dale, M.R.T., 2000. Lacunarity analysis of spatial pattern: A comparison. *Landscape Ecology*, 15(5): 467-478.

De Cola, L., 1989. Fractal analysis of a classified Landsat scene. *Photogrammetric Engineering and Remote Sensing*, 55(5): 601-610.

Definiens, 2008. Difiniens User Guide. Definiens Imaging GmbH, Munich, Germany.

DeFries, R. S., Hansen, M., Townshend, J. R. G. and Sohlberg, R., 1998. Global land cover classifications at 8 km spatial resolution: The use of training data derived from Landsat imagery in decision tree classifiers. *International Journal of Remote Sensing*, 19(16): 3141-3168.

Dejong, S.M. and Burrough, P.A., 1995. A fractal approach to the classification of Mediterranean vegetation types in remotely-sensed images. *Photogrammetric Engineering and Remote Sensing*, 61(8): 1041-1053.

Demuth, H., Beale, M. and Hagan, M., 2008. *Neural Network Toolbox 6 User's Guide*. 907 pp. Available online at http://www.mathworks.com/access/helpdesk/help/pdf_doc/nnet/nnet.pdf (accessed on Apr.20, 2008)

Dong, P., 2000. Test of a new lacunarity estimation method for image texture analysis. *International Journal of Remote Sensing*, 21(17): 3369-3373.

Dong, P. and Leblon, B., 2004. Rock unit discrimination on Landsat TM, SIR-C and Radarsat images using spectral and textural information. *International Journal of Remote Sensing*, 25(18): 3745-3768.

Du, G. and Yeo, T.S., 2002. A novel lacunarity estimation method applied to SAR image segmentation. *IEEE Transactions on Geoscience and Remote Sensing*, 40(12): 2687-2691.

Emerson, C.W., Lam, N.S.N. and Quattrochi, D.A., 1999. Multi-scale fractal analysis of image texture and pattern. *Photogrammetric Engineering and Remote Sensing*, 65(1): 51-61.

Emerson, C.W., Lam, N.S.N. and Quattrochi, D.A., 2005. A comparison of local variance, fractal dimension, and Moran's I as aids to multispectral image classification. *International Journal of Remote Sensing*, 26(8): 1575-1588.

Erbek, F.S., Ozkan, C. and Taberner, M., 2004. Comparison of maximum likelihood classification method with supervised artificial neural network algorithms for land use activities. *International Journal of Remote Sensing*, 25(9): 1733-1748.

Foody, G.M. and Mathur, A., 2004a. A relative evaluation of multiclass image classification by support vector machines. *IEEE Transactions on Geoscience and Remote Sensing*, 42(6): 1335-1343.

Foody, G.M. and Mathur, A., 2004b. Toward intelligent training of supervised image classifications: directing training data acquisition for SVM classification. *Remote Sensing of Environment*, 93(1-2): 107-117.

Galante, M., 1996. Genetic algorithms as an approach to optimize real-world trusses. *International Journal for Numerical Methods in Engineering*, 39(3): 361-382.

Gefen, Y., Aharony, A. and Mandelbrot, B.B., 1984. Phase-transitions on fractals: III. Infinitely ramified lattices. *Journal of Physics a-Mathematical and General*, 17(6): 1277-1289.

Gislason, P.O., Benediktsson, J.A. and Sveinsson, J.R., 2006. Random forests for land cover classification. *Pattern Recognition Letters*, 27(4): 294-300.

Goldberg, D.E., 1989. *Genetic Algorithms in Search, Optimization, and Machine Learning*. Addison Wesley, Reading, Massachusetts, 412 pp.

Goodchild, M.F., 1980. Fractals and the accuracy of geographical measures. *Journal of the International Association for Mathematical Geology*, 12(2): 85-98.

Goodchild, M.F., 1986. *Spatial Autocorrelation*. Geo Books, Norwich, 56 pp.

Greenhill, D.R., Ripke, L.T., Hitchman, A.P., Jones, G.A. and Wilkinson, G.G., 2003. Characterization of suburban areas for land use planning using landscape ecological indicators derived from IKONOS-2 multispectral imagery. *IEEE Transactions on Geoscience and Remote Sensing*, 41(9): 2015-2021.

Haralick, R.M., Shanmugam, K. and Dinstein, I.H., 1973. Texture features for image classification. *IEEE Transactions on Systems, Man, and Cybernetics*, 3(6): 610-621.

Haralick, R.M. and Shapiro, L.G., 1985. Image segmentation techniques. *Computer Vision Graphics and Image Processing*, 29(1): 100-132.

Henebry, G.M. and Kux, H.J.H., 1995. Lacunarity as a texture measure for SAR imagery. *International Journal of Remote Sensing*, 16(3): 565-571.

Hodgson, M.E., 1998. What size window for image classification? A cognitive perspective. *Photogrammetric Engineering and Remote Sensing*, 64(8): 797-807.

Hsu, C.W. and Lin, C.J., 2002. A comparison of methods for multiclass support vector machines. *IEEE Transactions on Neural Networks*, 13(2): 415-425.

Hu, X.Y., Tao, C.V. and Prenzel, B., 2005. Automatic segmentation of high-resolution satellite imagery by integrating texture, intensity, and color features. *Photogrammetric Engineering and Remote Sensing*, 71(12): 1399-1406.

Huang, B., Cheu, R.L. and Liew, Y.S., 2004. GIS and genetic algorithms for HAZMAT route planning with security considerations. *International Journal of Geographical Information Science*, 18(8): 769-787.

Huang, C., Davis, L.S. and Townshend, J.R.G., 2002. An assessment of support vector machines for land cover classification. *International Journal of Remote Sensing*, 23(4): 725-749.

Jackson, Q. and Landgrebe, D.A., 2002. Adaptive Bayesian contextual classification based on Markov random fields. *IEEE Transactions on Geoscience and Remote Sensing*, 40(11): 2454-2463.

Jaggi, S., Quattrochi, D.A. and Lam, N.S.N., 1993. Implementation and operation of 3 fractal measurement algorithms for analysis of remote-sensing data. *Computers and Geosciences*, 19(6): 745-767.

Jin, X.C. and Ong, S.H., 1995. A practical method for estimating fractal dimension. *Pattern Recognition Letters*, 16 (5): 457-464.

Jobanputra, R. and Clausi, D.A., 2006. Preserving boundaries for image texture segmentation using grey level co-occurring probabilities. *Pattern Recognition*, 39(2): 234-245.

Ju, W., Lam, N.S.-N. and Chen, J., 2006. Application of Kohonen self-organizing map for urban structure analysis, *2006 IEEE International Conference on Granular Computing*, May 10-12, 2006, Atlanta, GA., pp. 118-123.

Kasetkasem, T. and Varshney, P.K., 2002. An image change detection algorithm based on Markov random field models. *IEEE Transactions on Geoscience and Remote Sensing*, 40(8): 1815-1823.

Kavzoglu, T. and Mather, P.M., 2003. The use of backpropagating artificial neural networks in land cover classification. *International Journal of Remote Sensing*, 24(23): 4907-4938.

Kerle, N., Froger, J.L., Oppenheimer, C. and De Varies, B.V., 2003. Remote sensing of the 1998 mudflow at Casita volcano, Nicaragua. *International Journal of Remote Sensing*, 24(23): 4791-4816.

Ketting, R.L. and Landgrebe, D.A., 1976. Classification of multispectral image data by extraction and classification of homogeneous objects. *IEEE Transactions on Geoscience and Remote Sensing*, 14(1): 19-26.

Knerr, S., Personnaz, L. and Dreyfus, G., 1990. Single-layer learning revisited: A stepwise procdure for building and training neural network. In: F. Fogelman-Soulié and J. Hérault (Editors), *Neuro-computing : Algorithms, Architectures, and Applications*. NATO ASI series. Springer-Verlag, Berlin, pp. 41-50.

Kohonen, T., 1995. *Self-Organizing Maps*. Springer-Verlag, Berlin.

Lam, N., 2003. Geographic information systems and science. *Annals of the Association of American Geographers*, 93(1): 259-261.

Lam, N., 2004. Fractals and scale in environmental assessment and monitoring. In: E.S. Sheppard and R.B. McMaster (Editors), *Scale and geographic inquiry : nature, society, and method*. Blackwell Publishing, Oxford, UK, pp. 23-40.

Lam, N.S.-N., Qiu, H.L., Quattrochi, D.A. and Emerson, C.W., 2002. An evaluation of fractal methods for characterizing image complexity. *Cartography and Geographic Information Science*, 29(1): 25-35.

Lam, N.S.-N., Quattrochi, D.A., Qiu, H.L. and Zhao, W., 1998. Environmental assessment and monitoring with image characterization and modeling system using multiscale remote sensing data. *Applied Geographical Studies*, 2(2): 77-93.

Lam, N.S.-N., Zhou, G. and Ju, W., 2008. Relating visual changes in images with spatial metrics. In: M. Yuan and K. Hornsby (Editors), *Understanding of Dynamics in Geographic Domains*. CRC Press, Bacon Raton. 240 pp.

Lam, N.S.N. and De Cola, L., 1993. *Fractals in Geography*. PTR Prentice Hall, Englewood Cliffs, N.J., 308 pp.

Lewis, H.G. and Brown, M., 2001. A generalized confusion matrix for assessing area estimates from remotely sensed data. *International Journal of Remote Sensing*, 22(16): 3223-3235.

Li, X. and Yeh, A.G.O., 2005. Integration of genetic algorithms and GIS for optimal location search. *International Journal of Geographical Information Science*, 19(5): 581-601.

Li, Z., Li, X., Wang, Y., Ma, A. and Wang, J., 2004. Land-use change analysis in Yulin prefecture, northwestern China using remote sensing and GIS. *International Journal of Remote Sensing*, 25(24): 5691-5703.

Lin, B. and Yang, Z.R., 1986. A suggested lacunarity expression for Sierpinski carpets. *Journal of Physics a-Mathematical and General*, 19(2): L49-L52.

Liu, A.J. and Cameron, G.N., 2001. Analysis of landscape patterns in coastal wetlands of Galveston Bay, Texas (USA). *Landscape Ecology*, 16(7): 581-595.

Liu, X. and Lathrop, R.G., 2002. Urban change detection based on an artificial neural network. *International Journal of Remote Sensing*, 23(12): 2513-2518.

Liverman, D., Moran, E.F., Rindfuss, R.R. and Stern, P.C., 1998. *People and Pixels: Linking Remote Sensing and Social Science.* National Academy Press., Washington, D.C.

Lo, C.P., Quatrochi, D.A. and Luvall, J.C., 1997. Application of high-resolution thermal infrared remote sensing and GIS to assess the urban heat island effect. *International Journal of Remote Sensing*, 18(2): 287-304.

MacKay, D.J.C., 1992. Bayesian interpolation. *Neural Computation*, 4(3): 415–447.

Mandelbrot, B.B., 1975. Geometry of homogeneous turbulence, with stress on fractal dimension of ISO-surfaces of scalars. *Journal of Fluid Mechanics*, 72(Dec9): 401-416.

Mandelbrot, B.B., 1983. *The Fractal Geometry of Nature*. W.H. Freeman, New York, 468 pp.

Maniezzo, V., 1994. Genetic evolution of the topology and weight distribution of neural networks. *IEEE Transactions on Neural Networks*, 5(1): 39-53.

Maselli, F., Conese, C., Defilippis, T. and Romani, M., 1995. Integration of ancillary data into a maximum-likelihood classifier with nonparametric priors. *ISPRS Journal of Photogrammetry and Remote Sensing*, 50(2): 2-11.

McIver, D.K. and Friedl, M.A., 2002. Using prior probabilities in decision-tree classification of remotely sensed data. *Remote Sensing of Environment*, 81(2-3): 253-261.

Mills, H., Cutler, M.E.J. and Fairbairn, D., 2006. Artificial neural networks for mapping regional-scale upland vegetation from high spatial resolution imagery. *International Journal of Remote Sensing*, 27(11): 2177-2195.

Miranda, F.P., Fonseca, L.E.N. and Carr, J.R., 1998. Semivariogram textural classification of JERS-1 (Fuyo-1) SAR data obtained over a flooded area of the Amazon rainforest. *International Journal of Remote Sensing*, 19(3): 549-556.

Mitchell, T.M., 1997. *Machine Learning*. McGraw-Hill, New York, 414 pp.

Mitri, G.H. and Gitas, I.Z., 2004. A performance evaluation of a burned area object-based classification model when applied to topographically and non-topographically corrected TM imagery. *International Journal of Remote Sensing*, 25(14): 2863-2870.

Myint, S.W. and Lam, N., 2005a. Examining lacunarity approaches in comparison with fractal and spatial autocorrelation techniques for urban mapping. *Photogrammetric Engineering and Remote Sensing*, 71(8): 927-937.

Myint, S.W. and Lam, N.S.-N., 2005b. A study of lacunarity-based texture analysis approaches to improve urban image classification. *Computers, Environment and Urban Systems*, 29(5): 501-523.

Myint, S.W., Lam, N.S.N. and Tyler, J.M., 2004. Wavelets for urban spatial feature discrimination: Comparisons with fractal, spatial autocorrelation, and spatial co-occurrence approaches. *Photogrammetric Engineering and Remote Sensing*, 70(7): 803-812.

Myint, S.W., Mesev, V. and Lam, N., 2006. Urban textural analysis from remote sensor data: Lacunarity measurements based on the differential box counting method. *Geographical Analysis*, 38(4): 371-390.

Pal, M., 2006. Support vector machine-based feature selection for land cover classification: a case study with DAIS hyperspectral data. *International Journal of Remote Sensing*, 27(14): 2877-2894.

Pal, M. and Mather, P.M., 2003. An assessment of the effectiveness of decision tree methods for land cover classification. *Remote Sensing of Environment*, 86(4): 554-565.

Pal, M. and Mather, P.M., 2005. Support vector machines for classification in remote sensing. *International Journal of Remote Sensing*, 26(5): 1007-1011.

Pal, N.R. and Pal, S.K., 1993. A review on image segmentation techniques. *Pattern Recognition*, 26(9): 1277-1294.

Pedroni, L., 2003. Improved classification of Landsat Thematic Mapper data using modified prior probabilities in large and complex landscapes. *International Journal of Remote Sensing*, 24(1): 91-113.

Pendleton, D.E., Dathe, A. and Baveye, P., 2005. Influence of image resolution and evaluation algorithm on estimates of the lacunarity of porous media. *Physical Review E*, 72(4): 041316. DOI: 10.1103/PhysRevE.72.041306.

Plaza, A., Martinez, P., Perez, R. and Plaza, J., 2004. A new approach to mixed pixel classification of hyperspectral imagery based on extended morphological profiles. *Pattern Recognition*, 37(6): 1097-1116.

Plotnick, R.E., Gardner, R.H. and Oneill, R.V., 1993. Lacunarity indexes as measures of landscape texture. *Landscape Ecology*, 8(3): 201-211.

Plotnick, R.E., Gardner, R.H., Hargrove, W.W., Prestegaard, K. and Perlmutter, M., 1996. Lacunarity analysis: a general technique for the analysis of spatial patterns. *Physical Review E*, 53(5): 5461-5468.

Pontius, R.G. and Cheuk, M.L., 2006. A generalized cross-tabulation matrix to compare soft-classified maps at multiple resolutions. *International Journal of Geographical Information Science*, 20(1): 1-30.

Qiu, H.L., Lam, N.S.N., Quattrochi, D.A. and Gamon, J.A., 1999. Fractal characterization of hyperspectral imagery. *Photogrammetric Engineering and Remote Sensing*, 65(1): 63-71.

Quattrochi, D.A., Emerson, C.W., Lam, N.S.-N. and Qiu, H.L., 2001. Fractal characterization of multitemporal remote sensing data. In: N.J. Tate and P.M. Atkinson (Editors), *Modelling scale in geographical information science*. Wiley, Chichester ; New York, pp. 13–34.

Quattrochi, D.A. and Goodchild, M.F., 1997. *Scale in Remote Sensing and GIS*. CRC Lewis, Boca Raton, Fla., 406 pp.

Quattrochi, D.A., Lam, N.S.-N., Qiu, H.L. and Zhao, W., 1997. Image Characterization and Modeling System (ICAMS): A geographic information system for the characterization and modeling of multiscale remote sensing data. In: D.A. Quattrochi and M.F. Goodchild (Editors), *Scale in Remote Sensing and GIS*. CRC/Lewis Publishers, Boca Raton, Fla.

Read, J.M. and Lam, N.S.N., 2002. Spatial methods for characterising land cover and detecting land-cover changes for the tropics. *International Journal of Remote Sensing*, 23(12): 2457-2474.

Sarkar, N. and Chaudhuri, B.B., 1992. An efficient approach to estimate fractal dimension of textural images. *Pattern Recognition*, 25(9): 1035-1041.

Solberg, A.H.S., Taxt, T. and Jain, A.K., 1996. A Markov random field model for classification of multisource satellite imagery. *IEEE Transactions on Geoscience and Remote Sensing*, 34(1): 100-113.

Sun, W., Xu, G., Gong, P. and Liang, S., 2006. Fractal analysis of remotely sensed images: A review of methods and applications. *International Journal of Remote Sensing*, 27(22): 4963-4990.

Sun, W.X., 2006. Three new implementations of the triangular prism method for computing the fractal dimension of remote sensing images. *Photogrammetric Engineering and Remote Sensing*, 72(4): 373-382.

Tan, P.-N., Steinbach, M. and Kumar, V., 2005. *Introduction to Data Mining*. Addison Wesley. Boston, 769 pp.

Tate, N.J., 1998. Estimating the fractal dimension of synthetic topographic surfaces. *Computers and Geosciences*, 24(4): 325-334.

Tralli, D.M., Blom, R.G., Zlotnicki, V., Donnellan, A. and Evans, D.L., 2005. Satellite remote sensing of earthquake, volcano, flood, landslide and coastal inundation hazards. *ISPRS Jounral of Photogrammetry and Remote Sensing*, 59(4): 185-198.

Turner, M.G. and Ruscher, C.L., 1988. Changes in landscape patterns in Georgia, USA. *Landscape Ecology*, 1(4): 241-251.

Vapnik, V.N., 1998. *Statistical Learning Theory*. Wiley, New York, 736 pp.

Vapnik, V.N., 2000. *The Nature of Statistical Learning Theory*. Springer-Verlag, New York, 314 pp.

Verbeke, L.P.C., Vancoillie, F.M.B. and De Wulf, R.R., 2004. Reusing back-propagation artificial neural networks for land cover classification in tropical savannahs. *International Journal of Remote Sensing*, 25(14): 2747-2771.

Voss, R.F., 1986. Characterization and measurement of random fractals. *Physica Scripta*, T13: 27-32.

Voss, R.F., 1988. Fractals in nature: from characterization to simulation. In: H.-O. Peitgen, D. Saupe and M.F. Barnsley (Editors), *The Science of Fractal Images*. Springer-Verlag, New York, pp. 21–70.

Woodcock, C. and Harward, V.J., 1992. Nested-hierarchical scene models and image segmentation. *International Journal of Remote Sensing*, 13(16): 3167-3187.

Wulder, M. and Boots, B., 1998. Local spatial autocorrelation characteristics of remotely sensed imagery assessed with the Getis statistic. *International Journal of Remote Sensing*, 19(11): 2223-2231.

Yang, F.H., White, M.A., Michaelis, A.R., Ichii, K., Hashimoto, H., Votava, P., Zhu, A-X. and Nemani, R.R, et al., 2006. Prediction of continental-scale evapotranspiration by combining MODIS and AmeriFlux data through support vector machine. *IEEE Transactions on Geoscience and Remote Sensing*, 44(11): 3452-3461.

Yu, Q., Gong, P., Clinton, N., Biging, G., Kelly, M. and Schirokauer, D., 2006. Object-based detailed vegetation classification with airborne high spatial resolution remote sensing imagery. *Photogrammetric Engineering & Remote Sensing*, 72(7): 799-811.

Yuan, Y., Smith, R.M. and Limp, W.F., 1997. Remodeling census population with spatial information from Landsat TM imagery, *Computers, Environment and Urban Systems*, 21(3-4): 245-258.

Zhao, W., 2001. *Multiscale Analysis for Characterization of Remotely Sensed Images*. Ph.D. Thesis, Louisiana State University., Baton Rouge, LA, 238 pp.

Zheng, M., Cai, Q. and Wang, Z., 2005. Effect of prior probabilities on maximum likelihood classifier, *IEEE International on Geoscience and Remote Sensing Symposium*, *2005*. IEEE Press, Seoul, Korea, pp. 3753-3756.

Zhou, G., 2006. *Detecting the Socioeconomic Conditions of Urban Neighborhoods through Wavelet Analysis of Remotely Sensed Imagery*. Ph.D. Thesis, Louisiana State University, Baton Rouge, LA, 160 pp.

Zhou, G.Y. and Lam, N.S.N., 2005. A comparison of fractal dimension estimators based on multiple surface generation algorithms. *Computers and Geosciences*, 31(10): 1260-1269.

Zhu, C.Q. and Yang, X.M., 1998. Study of remote sensing image texture analysis and classification using wavelet. *International Journal of Remote Sensing*, 19(16): 3197-3203.

Appendix:
A Worked Remote Sensing Example of the Genetic Bayesian Classifier

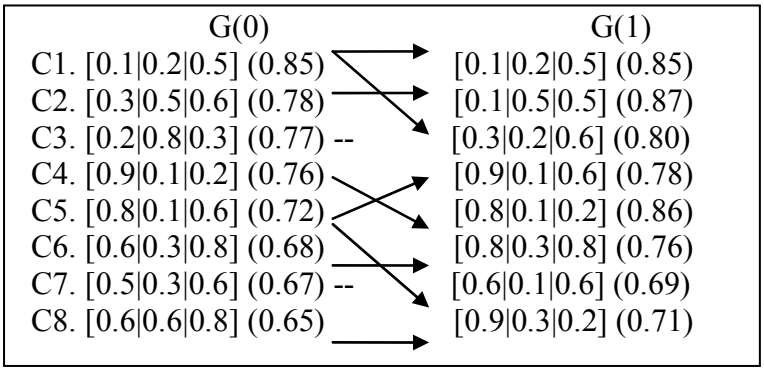

Figure A1. Demonstration of genetic evolution

As shown in the above figure, suppose there are three land use classes: urban, forest, and water. We can arbitrarily set the initial population G(0) to have 8 chromosomes; each one is coded with arbitrary pseudo prior probability *P'(c)* for each class, followed by its fitness value (overall classification accuracy of the training sets) in parentheses. The corresponding solution of prior probabilities is the normalized version of the chromosome by its genes' summation, according to equation (8). We can set the elite member count to 1 and crossover rate to 0.8. The chromosomes are sorted according to their fitness values.

Chromosome C1 is passed to next generation G(1) due to elitism (highest accuracy, 0.85). According to the crossover rate, given a total of 8 populations, there should be three pairs performing crossover and 1 chromosome performing mutation. The three pairs of parent chromosomes and the mutating chromosome are randomly selected from G(0). The chance of a chromosome being selected is proportional to its fitness value. Suppose C1&C2, C4&C5, C5&C6 are selected to perform crossover, and C8 is selected to perform mutation. C3 and C7 are not selected to perform reproduction. Thus the next generation G(1) is generated.

The genetic operation continues until it reaches an optimal solution, say [0.5 0.7 0.8] (0.91). This one will be normalized to [0.25 0.35 0.4], which is the optimized prior probabilities. These probabilities are then entered into the classification function (equation 6) to classify the entire image.

Vita

Wenxue Ju was born in Zhucheng City, Shandong Province, China. He entered Peking University in 1996 and received his Bachelor of Science degree in urban and regional planning (minor in computer science) in 2000. He received his Master of Science degree in environmental science in 2003 from Peking University. He joined the Louisiana State University in the fall of 2004 to work toward a degree of Doctor of Philosophy in geography, with a concentration in mapping sciences.